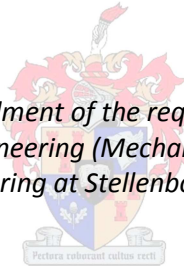


**EXPERIMENTAL AND NUMERICAL MODELLING INVESTIGATIONS OF THE
RESPONSE OF A TWO-PHASE NATURAL CIRCULATION MULTI-PARALLEL
CHANNEL SYSTEM**

Lucy Sithombesethu Sangweni

*Thesis presented in partial fulfilment of the requirements for the degree of
Master of Engineering (Mechanical) in the
Faculty of Engineering at Stellenbosch University*



Supervisor: Mr Robert Thomas Dobson

March 2015

DECLARATION

By submitting this thesis electronically, I declare that the entirety of the work contained therein is my own, original work, that I am the sole author thereof (save to the extent explicitly otherwise stated), that reproduction and publication thereof by Stellenbosch University will not infringe any third party rights and that I have not previously in its entirety or in part submitted it for obtaining any qualification.

.....
Signature of candidate

Date: 23rd February 2015

Copyright © 2015 Stellenbosch University

All rights reserved

ABSTRACT

In the present study, two-phase natural circulation flow in a multi-parallel channel system was investigated using experimental and numerical modelling. The investigation was carried out under different power excitations and various system operations (open system, closed system and heat pipe mode). The multichannel system was equipped at the upper end with a condenser enclosed within a steam drum, while the lower portion of each channel was heated to heat the system. For the numerical modelling, transient one-dimensional conservation equations were derived from first principle for both single- and two-phase fluids and used to computer program the system's discretised simulation model. Temperatures and mass flow rates of the fluid responses as a result of different power excitations and operations were obtained for both the experimental and numerical modelling.

It was observed from the results that the fluid experiences a start-up transient before accomplishing steady-state conditions. It was further noted that the transient duration varies with power excitations and system operation modes and hence with the stability of the system. A rise in power proved not to necessarily increase the fluid mass flow rate, but invited oscillations with higher amplitudes, depending on the system's mode of operation. Type I instability and low-quality steam oscillations were witnessed at low power and open system operation mode (system open to the atmosphere). Type II instabilities and flashing instability were observed to be associated with medium and high-power excitations for the open system mode of operation.

The fluid flow became more stable and less oscillatory at all power excitations for the closed system operation mode (system not open to the atmosphere). However, a sub-cooling effect was evident at higher power, where the two-phase fluid temperatures oscillated in a sinusoidal manner. However, the mass flow rates oscillated with high amplitudes in the forward direction in some channels and assumed a unidirectional flow in other channels. In general, steady-state conditions were obtained earlier when the system was operated as a closed system. For the heat pipe mode of operation, the system transient response in all channels exhibited a geysering instability followed by flashing-induced boiling. In-phase (flow in channels exhibiting the same behaviour) and out-of-phase (flow in channels exhibiting contradictory conduct) behaviour between adjacent channels were observed at all power excitations and system operation modes. Flow reversal in heated channels of a natural circulation system were proven to exist even under equal power excitations.

OPSOMMING

In hierdie studie is tweefasige natuurlike sirkulasievloei in 'n parallelle multikanaalstelsel ondersoek deur middel van eksperimentele en numeriese modellering. Die ondersoek is onder verskillende kragopwekkings en verskeie stelselwerkings (oop stelsel, toe stelsel en hittepyppmodus). Die multikanaalstelsel is aan die bopunt met 'n kondensator binne 'n stoomdrom toegegerus, terwyl die laer gedeelte van elke kanaal verhit is om die stelsel te verhit. Vir die numeriese modellering, is oorgangseendimensionele behoudsvergelykings vanaf die eerste beginsel vir beide een- en tweefasige vloeistowwe afgelei en dit is gebruik om die stelsel se gediskretiseerde simulasiemodel vir 'n rekenaar te programmeer. Temperature en massavloeiempo's van die vloeistofrespons as gevolg van verskillende kragopwekkings en -werkings is vir beide die eksperimentele en die numeriese modellering verkry.

Dit is in die resultate waargeneem dat die vloeistof 'n aansitoorgang ervaar voor dit vloeiewewigstoestand bereik. Daar is verder waargeneem dat die duur van die oorgang wissel volgens kragopwekkings en stelselwerkingsmodusse en dus op grond van die stabiliteit van die stelsel. 'n Toename in krag het nie noodwendig die vloeitempo van die vloeistofmassa verhoog nie, maar het aanleiding gegee tot ossillasies met groter amplitudes, afhangende van die stelsel se metode van werking. Tipe I-onstabiliteit en stoom-ossillasies van 'n lae intensiteit is teen lae krag en oop stelselwerkingsmodus waargeneem (stelsel oop aan die atmosfeer). Tipe II-onstabiliteit en flitsingsonstabiliteit (*flashing instability*) is met medium- en hoë kragopwekkings vir die oop stelselmodus van werking waargeneem.

Die vloeistofvloei het meer stabiel en minder ossillerend geraak by alle kragopwekkings in die geslote stelsel van werking (stelsel nie oop na die atmosfeer nie). 'n Subverkoelingseffek was egter teen hoër krag duidelik, waar die tweefasige vloeistof se temperature sinusvormig geossilleer het. Die massavloeiempo's het egter met hoë amplitudes in die vorentoe rigting in sommige kanale gevloei en eenrigtingvloei in ander kanale vertoon. Oor die algemeen is vloeiewewigstoestand vroeër verkry toe die stelsel as 'n geslote stelsel bedryf is. Vir die hittepyppmodus van werking het die stelsel se oorgangseweergawe in alle kanale 'n *geysering* onstabiliteit getoon, gevolg deur flitsinggeïnduseerde (*flashing induced*) kook. Gelykfasige gedrag (vloei in kanale vertoon dieselfde gedrag) en ongelykfasige gedrag (vloei in kanale vertoon teenstrydige gedrag) tussen langsliggende kanale is met al die kragopwekkings en stelselwerkingsmodusse waargeneem. Vloei-omkering in die verhitte kanale van 'n natuurlike sirkulasiestelsel is bewys om selfs onder gelyke kragopwekkings te bestaan.

ACKNOWLEDGEMENTS

The author would like to thank the following people for their immeasurable contributions in making this investigation a success:

Robert Dobson –Supervisor

Thank you for believing in me, your words of encouragement, guidance, support and constructive criticism all geared me to navigate the study at full force.

Cobus Zietsman – Laboratory Manager

Thank you for your many helpful suggestions and making available every instrument needed to exploit the practical exercise at full command.

Special thanks to the laboratory technical team (Anthon, Nathi, Ferdie and the rest of the team) for going extra miles in making every end meet in setting up the experimental facility. You guys rock!

My family and friends

Your unconditional love lifts me up when I am sailing through waves of sophisticated amplitudes.

Jesus Christ

Thank you for drawing me closer from the furthest corners of the earth and deeming me appropriate.

CONTENTS

DECLARATION	I
ABSTRACT	II
OPSOMMING	III
ACKNOWLEDGEMENTS	IV
CONTENTS	V
LIST OF FIGURES	VII
LIST OF TABLES	IX
NOMENCLATURE	X
1 INTRODUCTION	1
1.1 CONCEPT OF NATURAL CIRCULATION	2
1.2 MOTIVATION	3
1.3 SCOPE OF WORK AND OBJECTIVES.....	3
2 LITERATURE SURVEY	5
2.1 FUTURE NUCLEAR POWER PLANTS REQUIREMENTS.....	5
2.1.1 Pumped/active systems.....	6
2.1.2 Advanced heavy water reactor (AHWR)	8
2.1.3 Reactor cavity cooling systems (RCCS) for pebble bed modular reactors (PBMR).....	9
2.1.4 Westinghouse AP1000	10
2.1.5 Reliability of passive systems.....	11
2.2 NATURAL CIRCULATION SYSTEMS INSTABILITIES	12
2.3 PRACTICAL EXAMINATIONS OF NATURAL CIRCULATION SYSTEM INSTABILITIES	14
2.4 THEORETICAL INVESTIGATIONS OF NATURAL CIRCULATION SYSTEMS INSTABILITIES	18
3 EXPERIMENTAL WORK	22
3.1 EXPERIMENTAL DESIGN.....	22
3.2 MATERIALS AND INSTRUMENTS SELECTION	25
3.3 CALIBRATION OF INSTRUMENTS.....	32
3.3.1 Calibration setup.....	32
3.3.2 Calibration procedures.....	34
3.3.3 Calibration results	36
3.4 EXPERIMENTAL PROCEDURE	41
4 MATHEMATICAL MODEL	44
4.1 DERIVATION OF EQUATIONS	44
4.2 SIMULATION COMPUTER PROGRAM	47

4.3 DEBUGGING PHASE.....	52
5 RESULTS AND DISCUSSION.....	53
5.1 EXPERIMENTAL OBSERVATIONS.....	53
5.2 EXPERIMENTAL RESULTS	54
5.2.1 Open expansion valve operating mode	55
5.2.2 Closed expansion valve system mode	62
5.2.3 Heat pipe mode.....	70
5.3 THEORETICAL SIMULATION PROGRAM RESULTS	73
6 CONCLUSIONS AND RECOMMENDATIONS.....	81
7 REFERENCE.....	84
APPENDIX A: CONDENSER DESIGN CALCULATIONS	87
APPENDIX B: DETAILED DERIVATION OF THE EQUATIONS OF CHANGE FOR THE MATHEMATICAL MODEL.....	89
B.1 CONSERVATION OF MASS FLOW RATE /CONTINUITY EQUATION.....	89
B.2 CONSERVATION OF MOMENTUM	90
B.3 CONSERVATION OF ENERGY.....	97
B.4 CLOSURE EQUATIONS.....	100
APPENDIX C: DERIVATION OF MOMENTUM EQUATION ASSUMING STEADY FLOW	104
APPENDIX D: PHOTOGRAPHS OF EXPERIMENTAL SETUP	107
APPENDIX E: SAMPLE RESULT OUTPUTS OF THE DEVELOPED PROGRAM	110
APPENDIX F: RESULTS FROM SIMILAR WORK DONE BY OTHER RESEACHERS	111

LIST OF FIGURES

Figure 1.1: Natural circulation loops.....	2
Figure 2.1: RBMK-1000 nuclear reactor (by world nuclear association 2014 report)	7
Figure 2.2: Heat removal paths of the AHWR (by Sihna and Kakodkar, 2006:693).....	9
Figure 3.1: Experimental setup view.....	24
Figure 3.2: Experimental setup drawing	26
Figure 3.3: Electric heater details	27
Figure 3.4: Condenser with 7 staggered \varnothing 15 mm tubes in two rows	28
Figure 3.5: Orifice flow meter drawing and representation	29
Figure 3.6: Differential pressure sensors calibration setup	33
Figure 3.7: Orifices calibration setup	34
Figure 3.8: Differential pressure sensor 1 calibration results.....	36
Figure 3.9: Differential pressure sensor 2 calibration results.....	37
Figure 3.10: Differential pressure sensor 3 calibration results.....	37
Figure 3.11: Orifice A calibration results.....	38
Figure 3.12: Orifice B calibration results.....	38
Figure 3.13: Orifice C calibration results.....	39
Figure 3.14: Thermocouple measurements vs. PRT reference temperatures.....	41
Figure 4.1: Discretized experimental model	45
Figure 4.2: One-dimensional mass, momentum and energy control volumes	46
Figure 5.1: Experimental temperatures and pressure drops measuring locations	54
Figure 5.2: Temperature as a function of time of a 3kW (1kW per riser) test open system	56
Figure 5.3: Mass flow rate as a function of time in channels 1, 2, 3 & 4 of a 3kW test open system	56
Figure 5.4: Temperature as a function of time of 6kW (2kW per riser) open system	58
Figure 5.5: Mass flow rate as a function of time in channels 1, 2, 3 & 4 of a 6kW open system	58
Figure 5.6: Temperature as a function of time of a 9kW (3kW per riser) test open system	60
Figure 5.7: Mass flow rate as a function of time in channels 1, 2, 3 & 4 of a 9kW open system	60
Figure 5.8: Two-phase natural circulation constant volume loop	62
Figure 5.9: Temperature as a function of time of 3kW test closed system.....	64
Figure 5.10: Mass flow rate as a function of time in channels 1, 2, 3 & 4 of a 3kW closed system	64
Figure 5.11: Temperature as a function of time of a 6kW test closed system	66
Figure 5.12: Mass flow rate as a function of time in channels 1, 2, 3 & 4 of a 6kW closed system	66
Figure 5.13: Temperature as a function of time of a 9kW test closed system	68
Figure 5.14: Mass flow rate as a function of time in channels 1, 2, 3 & 4 of a 9kW closed system	68

Figure 5.15: Temperature as a function of time of a 3x3kW test heat pipe operation mode	71
Figure 5.16: Mass flow rate as a function of time in channels 1, 2, 3 & 4 of a 3X3kW heat pipe mode ...	71
Figure 5.17: Simulation mass flow rates and temperature measuring locations	73
Figure 5.18: Temperature as a function of time of a 3kW test.....	75
Figure 5.19: Mass flow rate as a function of time in channels 1, 2, 3 & 4 of a 3kW test	75
Figure 5.20: Temperature as a function of time of a 6kW test.....	77
Figure 5.21: Mass flow rate as a function of time in channels 1, 2, 3 & 4 of a 6kW test	77
Figure 5.22: Temperature as a function of time of a 9kW test.....	79
Figure 5.23: Mass flow rate as function of time in channels 1, 2, 3 & 4 of a 9kW test	79
Figure B.1: Fixed control volume for continuity	89
Figure B.2: Fixed control volume for 1-D flow linear momentum (Figure 4.2 repeated).....	90
Figure B.3: Discretised experimental model	93
Figure B.4: Energy control volume.....	97
Figure C.1: Discretised experimental model (Figure B.3 repeated).....	105
Figure D.1: Photograph of experimental facility.....	107
Figure D.2: Heating elements and pressure gauge mounted on the steam drum	108
Figure D.3: Pressure relief valve mounted on the steam drum.....	109
Figure D.4: Valve connecting the expansion tank to the system and drainage system	109
Figure F.1: Individual channel behaviour for experiment at 1 bar pressure (Jain et al., 2010:784).....	111
Figure F.2: Inlet velocity oscillation curves (Yun et al., 2008:673).....	112

LIST OF TABLES

Table 3.1: Geometric dimensions of the experimental facility.....	24
Table 3.2: Properties of glass and polycarbonate materials.....	25
Table 3.3: Performance comparison of differential and absolute pressure sensors.....	30
Table 3.4: Betz 5000 micro-manometer	30
Table 3.5: Agilent® data acquisition unit specifications	31
Table 3.6: Eagle® data acquisition unit features specifications.....	31
Table 3.7: Thermocouples and platinum resistance thermometer measurements.....	40
Table A.1: Condenser sizing calculations	88

NOMENCLATURE

A	Area, m^2
a	acceleration, m/s^2
C_f	Fanning friction factor
c_p	specific heat at constant pressure, $J/kg.K$
c_v	specific heat at constant volume, $J/kg.K$
D	diameter, m
e	energy per unit mass, J/kg
E	energy, J
\dot{E}	energy transfer rate, W
F	force, N
f	Darcy friction factor
g	gravitation constant, m/s^2
G	mass flux, $kg/m^2.s$
Gr	Grashoff number, $Gr = \frac{g\beta(T_s - T_\infty)L_c^3}{\nu^2}$
h	heat transfer coefficient, $W/m^2^\circ C$
h	specific enthalpy, J/kg
h	height, m
i	enthalpy, J/kg
i_{fg}	latent heat of vaporization, J/kg
k	thermal conductivity, $W/m^\circ C$
K	minor loss coefficient
L	length, m
\dot{m}	mass transfer rate, kg/s
m	mass, kg
n	counter for loop branches
N	number
Nu	Nusselt number, $Nu = \frac{hD}{k}$
P	pressure, Pa
Pr	Prandtl number, $Pr = \frac{k}{\rho c}$
Q	heat, J
\dot{Q}	heat transfer rate, W
r	radius, m

R	thermal resistance, °C
R	resistance, Ω
Ra	Rayleigh number
Re	Reynolds number, $Re = \frac{\rho V d}{\mu} = \frac{4\dot{m}}{\pi \mu d}$
SF	slip factor
T	temperature, °C
t	time, s
u	internal energy, J
v	velocity, m/s
V	volume, m ³
V	Voltage, V
\dot{V}	volumetric flow rate, m ³ /s
w	width, m
W	work, J
\dot{W}	rate of work, W
x	mass fraction
z	distance, m

Greek Letters

α	void fraction
β	coefficient of volume expansion, K ⁻¹
θ	angle, °
ϕ^2	two phase multiplier
ρ	density, kg/m ³
σ	Stefan-Boltzmann constant, $\sigma = 5.67 \times 10^{-8} \text{ W/m}^2 \cdot \text{K}^4$
τ	shear stress, N/m ²
ε	emissivity
μ	viscosity, kg/m.s

Subscripts

∞	property of the far field
a	air
b	bottom
atm	atmosphere

<i>c</i>	convection, condensation
<i>com</i>	combined
<i>cw</i>	cooling water
<i>evap</i>	evaporisation
<i>conv</i>	convection
<i>f</i>	property of fluid
<i>fg</i>	difference in saturated liquid and saturated gas values of property
<i>gen</i>	internal heat generation
<i>i</i>	inside, in
<i>i</i>	control volume counter
<i>in</i>	in
<i>ℓ</i>	liquid
<i>lo</i>	liquid only
<i>o</i>	outside, out
<i>out</i>	out
<i>r</i>	riser
<i>rad</i>	radiation
<i>sat</i>	saturation
<i>s</i>	surface
<i>t</i>	top
<i>v</i>	vapour
<i>x</i>	in axial direction transverse to control volume
<i>z</i>	in direction transverse to control volume

Superscripts

<i>t</i>	time step
·	quantity per unit time
→	vector quantity

Abbreviations

AHWR – Advance heavy water reactor
FMWs – Field Metrology Wells
NCL – Natural circulation loop
PRT – Platinum resistance thermometer

1 INTRODUCTION

Natural circulation loops are capable of transporting heat passively from a heat source to a heat sink, utilizing natural forces such as convection and gravity. For this reason, natural circulation loops enhance safe operation and reliability as opposed to mechanically pumped systems. Therefore, such systems are used in many industrial systems, e.g. solar heaters, nuclear power plants, energy convertors and thermal control of electronic components (Swapnalee & Vijayan, 2011:54).

However, natural circulation loops are susceptible to various instabilities during operation. Instabilities in a natural circulation system are undesirable, as they can hinder the safe operation of plants. Flow instabilities in water-cooled industrial systems are of particular importance, since they can cause system control and mechanical vibration problems and hence must be avoided (Zhang et al., 2009). The challenges associated with natural circulation systems may be overcome with proper design and operation procedures to assure the integrity of the system (Jain et al., 2010:34). The problems of instabilities in natural circulation in both single and two-phase flow have attracted the attention of many thermal hydraulic scientists (Yun et al., 2008:35). Extensive studies have been carried out worldwide on the instabilities of natural circulation single-phase flow systems, but very few investigations have been done of the two-phase flow instabilities of multi-channel natural circulation systems (Reyes & Cleveland, 2005:37).

Most commercial energy-generation systems utilizing natural circulation boiling consist of many parallel channels connected between common plena. The presence of multiple channels poses many challenges, as it triggers various modes of flow instability that need to be overcome by proper design and operating procedures (Jain et al., 2010:34).

This study carries on from work done by Ruppertsberg (2008) and White (2011). In their studies, they worked on a single loop single-phase flow and double loop two-phase flow natural circulation system respectively, investigating and modelling the instabilities of such systems. In this context, a parallel channel loop has been designed and built to investigate the instabilities of a multi-channel thermosyphon loop. The loop comprises three identical parallel channels connected between a steam drum and header. A single down-comer connected between two common plenums, i.e. steam drum and header, provides the recirculation path. The multi-channel natural circulation system was also simulated theoretically. Detailed flow and stability experiments were undertaken at various operating conditions. The experimental response characteristics recorded in this manner were compared with the analytical model's results, and thereby the accuracy with which the analytical model simulates the experimental results was established.

1.1 Concept of Natural Circulation

Natural circulation is a process whereby fluid flows in a closed loop without the use of external forces (mechanical pumps). This process is utilized mostly to remove decay heat from the reactor core during an emergency in a boiling water reactor and pressurized water reactor (PWR), and in some instances to drive coolant in the primary loop instead of using active power pumps (Lu et al., 2010:3851). The basic operating principle of a natural circulation system can be illustrated as follows: a fluid-filled loop is heated at one location and cooled at another location. Usually, the cooling section (sink) is located at a higher elevation than the heated section (source) to enhance circulation rates. The operation of this system depends on the density difference between the heated and cooled section. The fluid absorbs heat from the source, expands and becomes less dense and rises up by buoyance force to the sink, where it gets cooled, becomes heavier in density and falls by force of gravity (Vijayan & Austregesilo, 1994:152), thus the process repeats itself as shown in Figure 1.1.

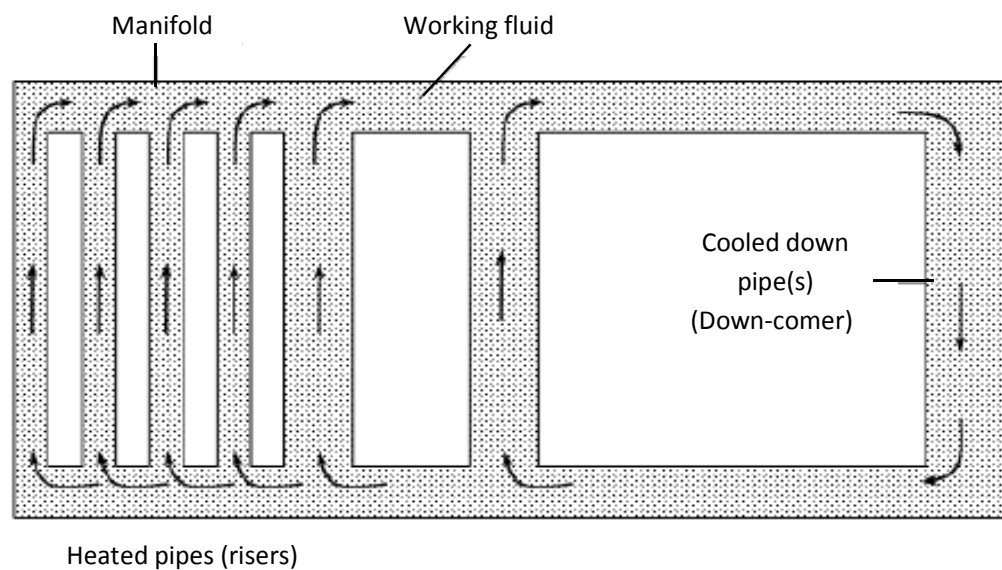


Figure 1.1: Natural circulation loops

Jain et al. (2010:776) state that the natural circulation mode of cooling offers many advantages, including simplicity of design and operation economy. This system is known for its passive safety features (elimination of external signal inputs of intelligence) and is utilized where high safety standards are required. Hence, natural circulation systems are considered to be more reliable than active systems, resulting in less demand on plant operators and maintenance staff requirements while providing a consistent cooling system even in the case of an emergency (Nayak & Sinha, 2007:486-487).

1.2 Motivation

Unsteady transient, dynamic flow behaviour and predictions are important in all transient and dynamic multi-channel natural circulation loops with risers, down-comers and manifolds, such as forced boiling in water reactors, steam generators, refrigeration plants and re-boilers. An analysis of the instabilities of such systems is crucial for the safety of the systems.

Extensive studies have been carried out worldwide on the instabilities of a natural circulation single-phase flow system, but very few studies have looked at the two-phase flow instabilities of a multi-channel natural circulation system (Reyes & Cleveland, 2005:37). Nuclear reactor cooling systems require multiple heated risers, cooled down pipes and various inlet/outlet manifolds and headers. This project hence contributes to future nuclear power stations, which are expected to have similar advanced passive safety features.

South Africa is looking at nuclear power stations for future base load generation that does not emit greenhouse gases and assures sustainable development. There is considerable debate around this proposal (nuclear power stations as safe means of power expansion), particularly among the public. Most people are concerned about the greenhouse effect, waste reduction, environmental protection, recycling and energy saving. The public opinion also raises concerns about the reliability and safety of nuclear power stations. It is thus crucial to liaise with the public and make people understand the safety, design philosophy and reliability of the nuclear power plant. One way of doing this is by providing rigid proof of excellently performing nuclear power plants worldwide. Also, investment in research on and development of advanced technologies to improve the safety aspects and reliability of nuclear power stations is needed.

Safety concerns relating to nuclear reactors have absorbed many researchers in two-phase flow and its flow instabilities in a multichannel system, including this present investigation. The current study contributes to the investigation of the flow instabilities of two-phase flow in multi-channel systems.

1.3 Scope of Work and Objectives

In the present study, a triple parallel channels transparent experimental system was designed, constructed and tested. Also, an analytical model resembling the experimental facility was developed and detailed flow behavioural analyses undertaken for different heat inputs to the risers and various system operation modes. The risers were subjected to variable electrical resistance heating element power inputs. Dynamic temperature and flow rate measurements (using thermocouples and differential pressure measurements across orifices respectively) were taken. These measurements then were conditioned, digitised and recorded.

The experimental response characteristics recorded in this manner were then compared with the analytical model's results and thereby the accuracy with which the analytical model simulates the experimental results could be established. The objectives of this project hence were to:

- Conduct an extensive literature study on natural circulation loop (NCL) operation, but focusing on the dynamic and transient flow behaviour.
- Design and construct a multi-channel natural circulation loop.
- Perform single- and two-phase flow experiments and identify any unstable behaviour.
- Write a simulation program to predict the experimental behaviour of a multiple NCL.
- Identify instabilities associated with single- and two-phase flow operating conditions.
- Identify heat pipe mode operation instabilities.
- Simulate outcomes to correlate with the experimental and literature outcomes.
- Confirm, where appropriate, some of the researched outcomes of similar systems already published.
- Document all the work done.

2 LITERATURE SURVEY

In order to obtain a broader understanding of the behaviour of a multichannel natural circulation system, a literature review was undertaken. In this section, a brief summary of studies done by other researchers in the past regarding multi-channel natural circulation systems is provided. The divisions in this section involve future nuclear power plants' requirements, natural circulation experiments, natural circulation modelling and natural circulation flow instabilities. At the end of each subsection, a summary of the findings and the paper's relevance are provided.

2.1 Future Nuclear Power Plants Requirements

According to Vecchiatto (2014), the South African cabinet has approved an integrated resource plan for power generation that calls for nuclear technology to become the single biggest new generator of electricity, peaking at 9 600 MW of power generation by 2029. Coal power stations currently meet about 95% of present electricity demand and are expected to expand more after the two giant coal power stations that are under construction, namely Kusile and Medupi, with 4 800 MW each of generating capacity, have come on board. While this is definitely good news for South African power, which is currently under severe strain, this is not good news for environmental activists and the future of the globe due to greenhouse gas emissions that arise from the operation of a coal-fired power stations.

A call to reduce greenhouse gas emissions during power generation has been taken serious through renewable energy harvesting technologies. However, the natural resources that the South African country holds for use in renewable power generation technologies are insufficient to supply the country's rising energy demands. Therefore nuclear power remains a cleaner technology than coal power and will secure the country's forecasted electricity needs. Nevertheless, there are lots of debates and concerns regarding the safety of nuclear power stations, particularly after the devastating earthquake and tsunami in Japan, and the crisis they caused at the Fukushima power station.

The purpose of the research being done at Stellenbosch University is to contribute to investigations also being done elsewhere in the world that are currently under way to achieve higher safety standards in terms of risk reduction in nuclear technology. One of the promising safety technologies is to incorporate passive systems into the design of new nuclear reactors by eliminating the requirements of operators or active inputs in their operation. Nayak and Sinha (2007:487) define a passive system as "either a system that consists of entirely passive components and structures or a system that partially utilizes active mechanisms to initiate ensuing passive operation".

The research points out that there are different classifications of passive safety systems that can be integrated into the design of nuclear reactors. Passive safety features that require minimum or zero external signal ability, including power sources, and have no moving mechanical parts to drive the working fluid were emphasised in this study. Hence, the subsequent sections look at certain nuclear power plant technologies and their related safety measures. This includes future safety plans for new nuclear plants and the incorporation of advanced safety measures into existing plants.

2.1.1 Pumped/active systems

Active systems are governed by an external source of power or human actions for their effective performance. Their reliance on power and human activation make them unfavourable for nuclear power stations, particularly in the case of an emergency. A pumped cooling system will cease to operate in an incident involving loss of power, which could lead to failure of the core cooling system, reactor meltdown and fission product release. For instance, on account of possible unforeseen devastation outside the protected reactor building, it is likely that all external sources of cooling water, electricity, air instrumentation and ventilation becomes disengaged from operation. In such cases it is also plausible that the operators may not be in a position to act in a resourceful manner. This was the case in the devastating accident in Japan, when the Fukushima plant ran out of water to cool the reactor core as a result of the power failure due to the tsunami.

So far, besides the Fukushima plant accident (2011), only two major accidents that have caused damage to the reactor core have taken place in the entire history of commercial nuclear power (Nayak & Sinha, 2007:486), viz. at Three Mile Island (1979) and Chernobyl (1986). In the case of the Three Mile Island accident, Nayak and Sinha (2007:486) declare that proper adherence to good engineering principles in the design of the plant prevented unacceptable radiation exposure of plant operators and members of the public, despite a series of human errors. According to Nayak and Sinha (2007:486), the Chernobyl nuclear power station accident materialised from several design errors, accompanied by a series of human errors. Nayak and Sinha (2007:486) further state that the Chernobyl accident was more severe in magnitude and resulted in the only fatalities. The lessons learnt from these incidents drew researchers' attention to the improvement in manpower-machine interfaces to minimise operator errors.

The Chernobyl nuclear plant consisted of an RBMK-1000 pressurized water reactor (PWR) that used water as a coolant and graphite as moderator. The RBMK reactor layout is shown in Figure 2.1 below.

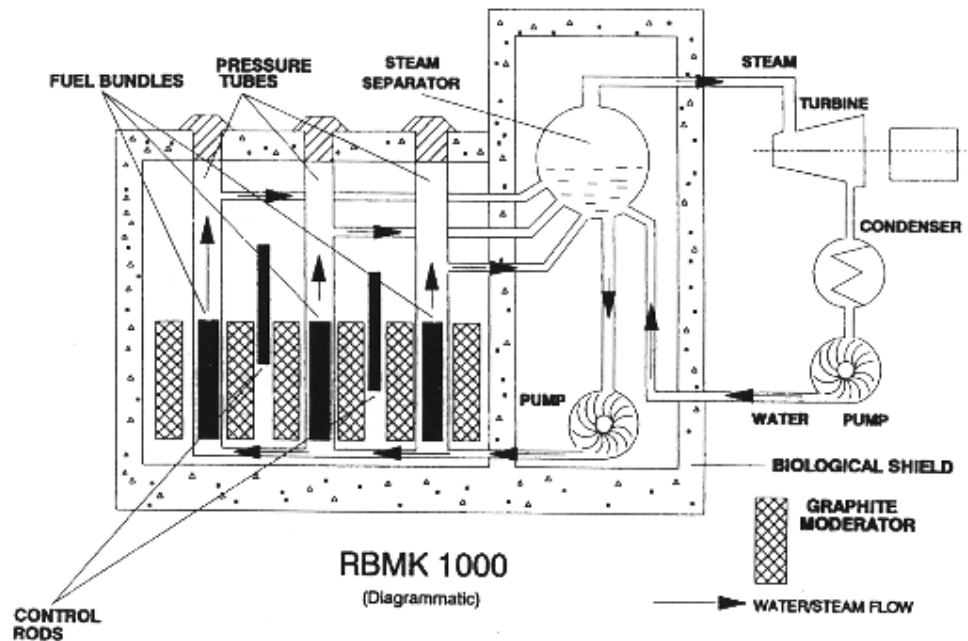


Figure 2.1: RBMK-1000 nuclear reactor (by world nuclear association 2014 report)

The RBMK reactor used at the Chernobyl nuclear power plant was unique and differed from other reactor designs in the sense that it was also utilized to produce weapons plutonium grade. However, the World Nuclear Association (2014a) report states that there were two problems with the physical features of the design that contributed to the severity of the incident:

- i) It possessed a positive void coefficient, i.e. excess steam voids led to increased power generation, cooling reduction and reduced neutron absorption, while retaining moderation, hence enhancing power production. This phenomenon can lead to rapid power increases as power and steam are directly proportional.
- ii) The reactor contained 211 control rods, of which 179 were inserted into the core from the top of the reactor. These rods were equipped with graphite riders at the bottom end. When the rods are at the upper position, the graphite rider lies in the fuelled region, replacing water. Graphite, unlike water, does not absorb neutrons, as much as water which promotes the chain reaction during the first part of their movement when the rods are dropped into the core from their fully withdrawn position.

The report of the World Nuclear Association (2014a) states that these flaws and their possible significance were known long prior the accident. The new RBMK reactors will incorporate a negative void coefficient in their design.

It is now mandatory for new-generation reactor designs to consider an extremely low probability of beyond design basis accidents (accidents that occurs not as a result of design error e.g. Tsunami caused accidents) as part of the design, state Nayak and Sinha (2007:487). Considering the necessity of power deployment using nuclear technology worldwide in the future, nuclear power plant safety measures have to be advanced for the next generation. Most of the new designs are incorporating inherent and passive safety features that are independent of human intervention or external sources of power for their successful performance. Nayak and Sinha (2007:487) state that a better understanding of nuclear power plants' operations and advances in technology can eliminate accidents like Three Mile Island and Chernobyl. In order to achieve advanced safety standards in nuclear power plants, the research shows that building small-size reactors and incorporating passive systems are amongst the best solutions to the safety concerns facing nuclear power plants.

2.1.2 Advanced heavy water reactor (AHWR)

According to Sihna and Kakodkar (2006:683), India has drawn out a nuclear power programme taking advantage of its local uranium, plutonium and thorium reserves in order to deliver long-term energy security to the country. The future nuclear power programme is based on the thorium-U fuel cycle, considering the massive thorium reserves in India. However, there is a requirement for sensible growth of thorium-based technologies for the whole fuel cycle. Sihna and Kakodkar (2006:683) state that the advanced heavy water reactor (AHWR) is being designed to accomplish this necessity. The AHWR is a small-sized (300MW), vertical, pressure tube-type, heavy water-moderated, boiling light water-cooled natural circulation reactor.

This reactor (AHWR) is equipped with advanced safety features (passive containment coolers, shut down by poison injection, passive moderator and concrete cooling systems) due to the fact that it is designed to remove core heat by natural circulation under normal operating conditions, consequently eliminating active pump usage. According to Sihna and Kakodkar (2006:683), the design of the AHWR also incorporates various innovative passive systems for the removal of decay heat under plant shut-down conditions and the alleviation of forecasted accidents. The AHWR has extension pipes to drive coolant circulation by natural convection to the steam drum. In the steam drum the steam is separated and supplied to the turbine, run through the condenser and returned back to the reactor as sub-cooled liquid.

Figure 2.2 shows the passive and active heat-removal paths of the AWHR. According to Sihna and Kakodkar (2006:692), the reactor power during normal operation is removed passively by a thermo-siphoning process. Light water transports heat from the fuel rods to the steam drums in a natural circulation manner. Steam drums are positioned at a certain height above the core to achieve the necessary flow rate (Sihna & Kakodkar, 2006:692).

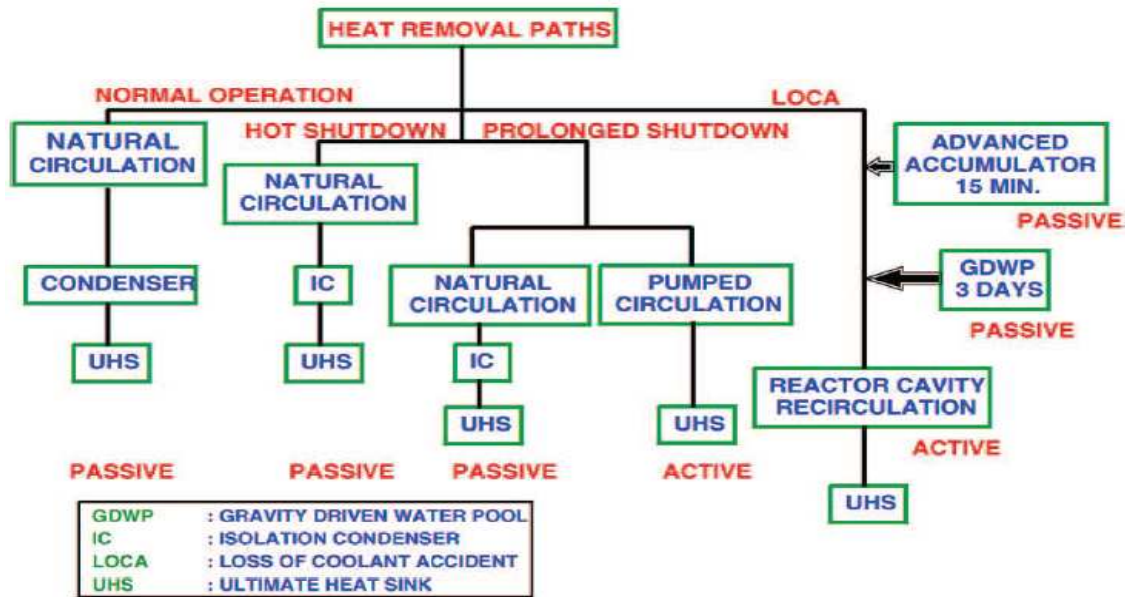


Figure 2.2: Heat removal paths of the AWHR (by Sihna and Kakodkar, 2006:693)

During shutdown, reactor core decay heat is removed by eight isolation condensers (ICs) immersed in the gravity-driven water pool (GDWP). After condensation the condensate returns to the core by gravity. In the case of a loss of coolant accident (LOCA), the reactor is equipped with four independent loops of emergency core-cooling system (ECCS) to provide cooling to the core for at least 72 hours.

2.1.3 Reactor cavity cooling systems (RCCS) for pebble bed modular reactors (PBMR)

A closed natural circulation loop is a heat transfer device capable of transporting heat from a heat source to a condenser over fairly long distances without the use of mechanically moving parts to drive the flow (Dobson & Ruppertsberg, 2008). Reactor cavity cooling systems consist of a number of axially symmetrical elements: the reactor core, reactor pressure vessel, reactor air cavity, concrete structure and cooling water heat sink, as shown in Figure 2.3.

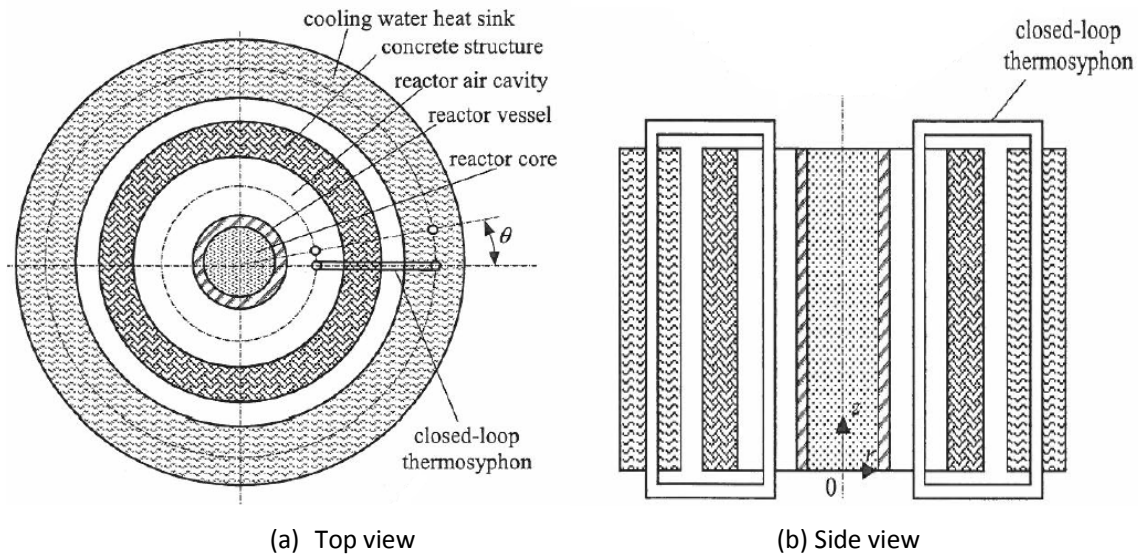


Figure 2.3: Axially symmetrical RCCS (by Dobson and Ruppertsberg, 2008)

According to Dobson and Ruppertsberg (2008), such a system within the reactor cavity would ensure the integrity of the fuel for the entire spectrum of hypothesised accidents during the operating lifetime of the reactor. The heat pipes are spread out around the margin of the reactor cavity at a pitch angle θ . Also, the heat pipes in the cavity are equipped with vertical fins to shield the concrete structure from radiation and convection and direct the heat to the pipes. This similar system could be incorporated in the safety innovation standards of new nuclear reactor designs.

2.1.4 Westinghouse AP1000

The AP1000 is a double loop 1 000 MWe pressurised water reactor (PWR). It is an upgraded form of the AP600. According to Schulz (2006:1547), the AP1000 incorporates passive safety systems to provide a significant enhancement in plant simplification, reliability, safety investment protection and costs. It uses proven competent technologies that have accumulated over 35 years of experience of operating PWR in the United State (US) (Schulz, 2006:1547). For instance, according to Schulz (2006:1548), Zircaloy grids, removable top nozzles and longer burn-up features are currently used in about 120 operating plants worldwide. Also, the AP1000 plant uses no pumps, fans, chillers, diesel generators or any rotating machinery for its safety systems, which eliminates the need for safety-related electric power sources. The safety performance has been verified by extensive testing, safety analysis and probabilistic assessment. Schulz (2006:1550-1551) states that the safety margins of the AP1000 are high and the potential of accident scenarios that could lead to the public's safety being jeopardised is extremely low. Figure 2.4 provides a schematic view of an AP1000 plant.

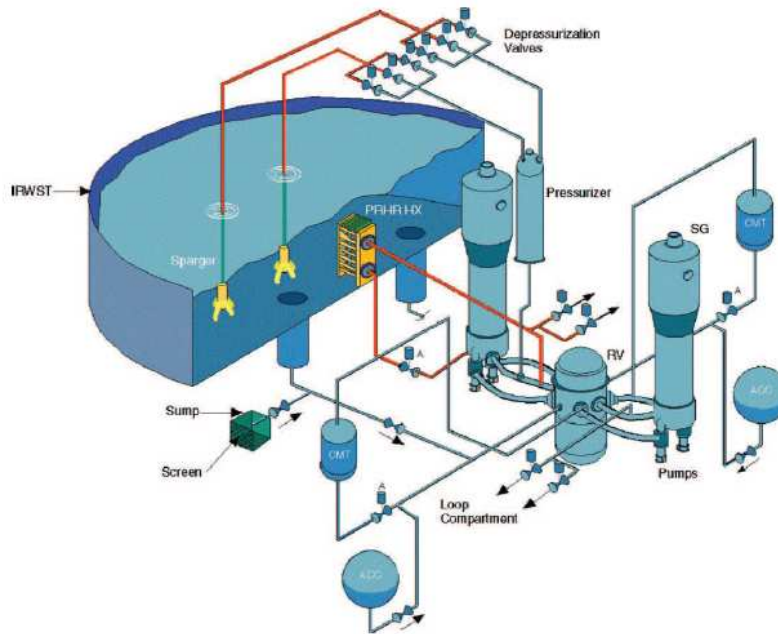


Figure 2.4: AP1000 plant schematic view (Schulz, 2006:1552)

The AP1000's reactor coolant system consists of two heat transfer circuits, with each containing one steam generator, two reactor coolant pumps and a single hot leg for circulating coolant between the reactor and the steam generator (Schulz, 2006:1550-1551). The system also integrates a pressuriser, interlocking piping, valves and instruments required for functioning control and the actuation of safety systems. Simplicity is a vital practical concept behind the design of the AP1000, which makes it easier to construct, operate and maintain. The simplicity of the AP 1000 also eliminates the need of manpower equipment therefore reducing monitoring and maintenance costs.

In case of an emergency, air cooling will be enhanced by water evaporation, and the water will drain by gravity from a tank located on top of the containment shield building. Schulz (2006:1553) states that air cooling only will be proficient for maintaining the containment below the pressure failure pressure should a water drain failure occur. Analysis performed on the AP1000's containment revealed that it will remain undamaged even during severe accidents.

2.1.5 Reliability of passive systems

While good engineering practice have been implemented successfully by incorporating passive systems in the designs of new nuclear reactors and many other systems, like any other design, passive systems have disadvantages too. Natural circulation (NC) systems are associated with various instabilities that are inherited from the weak driving forces of the passive system (buoyancy and gravitational forces), unlike the forced circulation system, where flow is imposed by a pump. Hence, there is a lot of debate regarding the reliability and safety of thermosyphon systems.

The instabilities of a natural circulation system require careful design and analysis methods to assure the safety of the system. This has become a serious problem that has absorbed many researchers across the globe, including this one.

The characteristics of the natural circulation cooling phenomenon requires the identification of conditions under which natural circulation will occur and then to determine its effectiveness. It also is necessary to identify factors that affect (e.g. geometrical plant conditions, loop components, etc.) the natural circulation process. Natural circulation will occur in a system whenever buoyancy forces resulting from density differences are adequate to overcome the flow resistances of geometrical loop components. Density differences cause fluid to circulate through the loops, providing a way of removing heat from the system. Natural circulation removes heat using at least two different modes of cooling, i.e. single-phase and two-phase modes. These modes of natural circulation are differentiated according to characteristics of mass flow rates and temperature difference behaviour.

In single-phase mode, the heat transfer driving mechanism is convection, whereas in two-phase mode density gradients are affected by temperature differences and voids in the primary loop. The study of the natural circulation cooling phenomenon focuses on several areas, including the effectiveness of natural circulation, the stability of various modes, transitions between modes, and flow interruptions due to instabilities. Instabilities in natural circulation are undesired, as they could lead to flow interruptions, which result in a reduction of heat removal. Hence, it is very important to understand factors that influence the onset of flow instabilities and the effect of instabilities on heat removal.

2.2 Natural Circulation Systems Instabilities

The following section explains instabilities encountered in the operation of a natural circulation system and their possible causes. These instabilities were gathered from various sources, such as Nayak et al. (2006), Jiang et al. (1995), Furuya et al. (2005) and IAEA-TECDOC-1474 (2005), to name just a few.

Type-I instability

According to Nayak et al. (2006:645), this type of instability occurs as a result of longer risers in a boiling two-phase natural circulation loop. Under low-quality conditions, a slight change in quality due to any disorder can cause large changes in void fraction and therefore in the driving head, thus making it possible for the flow to oscillate at low power. As the power increases, the flow quality increases and the slope of void fraction as a function of flow quality decreases. This suppresses fluctuations of the driving head for a minor change in quality, hence stabilising the flow at higher power (Nayak et al., 2006:645).

Type-II instability

Nayak et al. (2006:645) state that Type II instability occurs at higher power conditions. At high power the void fraction or quality becomes large, therefore increasing two-phase frictional pressure loss due to the two-phase mixture density being small. Large void fraction will give rise to a void propagation time delay in the two-phase region, causing a large fluctuation in the two-phase frictional pressure loss. A pressure drop in the single-phase flow region occurs due to the fluctuation of flow alone. The pressure drop pulse in the single-phase flow region moves much quicker due to the incompressibility of the fluid in this region. If pressure drop variations in the two-phase flow region are equal in magnitude, but out of phase with that of the single-phase region, the variation is sustained in the system since there are no diminishing mechanisms (Nayak et al., 2006:645).

Boiling crisis instability

IAEA-TECDOC-1474 (2005:23) states that this instability occurs when there is ineffective heat removal from the heated surface and that it is characterised by wall temperature excursion and flow oscillation.

Flow pattern transition instability

This instability is determined by bubbly flow with few voids, but a higher pressure drop than that of annular flow. Flow pattern transition instability is characterised by cyclic flow pattern alterations and flow rate variations (IAEA-TECDOC-1474, 2005:23).

Density wave oscillations

Furuya et al. (2005:1564) state that density wave oscillations occur as a result of regeneration feedbacks between the flow rate, vapour development rate and pressure drop. According to Furuya et al. (2005:1564), the period is 1.5 to two times the required time for the fluid to move through the pipe. This instability is associated with low frequencies (1 Hz) related to the transit time of a continuity wave.

Geysering

According to Jiang et al. (1995:112), geysering occurs at a definite inlet sub-cooling section. It is caused by vapour generation, growth, detachment and condensation. This causes flow rate oscillations with high amplitude and flow distribution that appear like pulses with no regular period (Jiang et al., 1995:117). This instability is characterised by a periodic process of super heat and violent evaporation with possible discharge and refilling.

Flashing-induced instability

Jiang et al. (1995:114) state that flashing-induced instability occurs in relatively low-pressure systems with long non-heated sections. It occurs at lower inlet subcooling, under which the system becomes unstable at diverse system pressures. The decrease in the inlet subcooling temperature triggers flashing instability that is accompanied by geysering. According to Jiang et al. (1995:118), geysering and flashing instability diminish with increasing pressure in the system. They (Jiang et al., 1995:118) revealed that the effects of these two instabilities vanished at a system pressure of approximately 0.3 MPa in their experimental investigation, where they had increased system pressure by adding nitrogen gas (N₂).

Parallel channel instability

Parallel channel instability is characterised by various modes of flow redistribution driven by an interaction between contiguous channels (IAEA-TECDOC-1474, 2005:23). According to IAEA-TECDOC-1474 (2005:146), multiple parallel channels consisting of different heat fluxes and connected to common plenums are bound to have different flow patterns, flow reversal in some channels, and some may even stagnate.

IAEA-TECDOC-1474 (2005:146) states that out-of-phase behaviour is one of the common oscillations of a parallel channel system and requires that individual channel flow measurements must be able to be detected.

Pressure drop oscillations

Pressure drop oscillations are categorised by a very low frequency (0.1 Hz) periodic process driven by dynamic interaction between channel and compressible volume (IAEA-TECDOC-1474, 2005:23).

The following sections discuss the outcomes of successful studies done in the past regarding instabilities associated with two-phase natural circulation systems and measures of mitigating such instabilities. The investigations were carried out through experimental tests and theoretical modelling.

2.3 Practical Examinations of Natural Circulation System Instabilities

Advanced conceptions of steam generator (nuclear power reactor) systems inherit passive safety features to remove decay heat. Queries arising with regard to this technology are: How reliable is the intelligence of the passive systems to respond in the designated way? Is the capability of the underlying physical mechanisms understood completely? Experimental investigations have been carried out worldwide to answer these questions. This technical research has contributed to a better understanding of the phenomenon and provided design improvements to mitigate negative impacts.

Jain et al. (2010) conducted an experiment on a parallel channel loop that resembles the pressure tube boiling water reactor to study the behaviour of a boiling natural circulation system (see Figure 2.5). Experiments were conducted at various (low and high) pressures to investigate pressure effects on the stability of a two-phase flow parallel natural circulation channel.

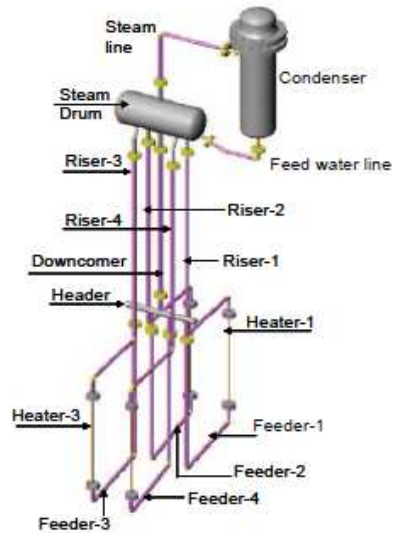


Figure 2.5: Schematic of parallel channel loop (by Jain et al. (2010:777))

They (Jain et al., 2010) observed the growth and decay of instability at both pressures at a low power, which was then classified as Type I instability. However, at intermediate power they observed a rather stable two-phase flow condition. At high power the onset of instability was observed again, and it was then classified as Type II instability. This flow behaviour was also observed in the present study, where a two-phase natural circulation multi-parallel channel system was exposed to various power excitations and system operating modes. It was further observed that the relationship between flow and power under two-phase flow conditions was governed by two regimes, viz. a buoyancy-dominated regime and a friction-dominated regime. For the buoyancy-dominated region, an increase in power resulted in a significant increase in flow rate, whereas in the friction-dominated regime, an increase in power resulted in a sudden decrease in but stable mass flow rate.

According to Jain et al. (2010:787), instabilities that initiate at high power are classified as Type II instability. Jain et al. (2010:787) conclude, based on their practical observations and the outcomes of the study, that the flow is more stable at high pressure, whereas instabilities of low pressure are accompanied by flow reversal. In the present study, the flow was observed to be more stable when the system was operated as a closed system, flow reversal was drastically reduced, and oscillations were rather sinusoidal and unidirectional at high power.

Krepper and Beyer (2010) numerically and experimentally studied passive systems for decay heat removal by natural circulation in large pools. They equipped modern concepts (emergency condenser pools) of nuclear power reactor systems to remove decay heat. The main purpose of their study was to investigate the heat removal capabilities of an emergency condenser with slightly inclined tubes (see Figure 2.6).

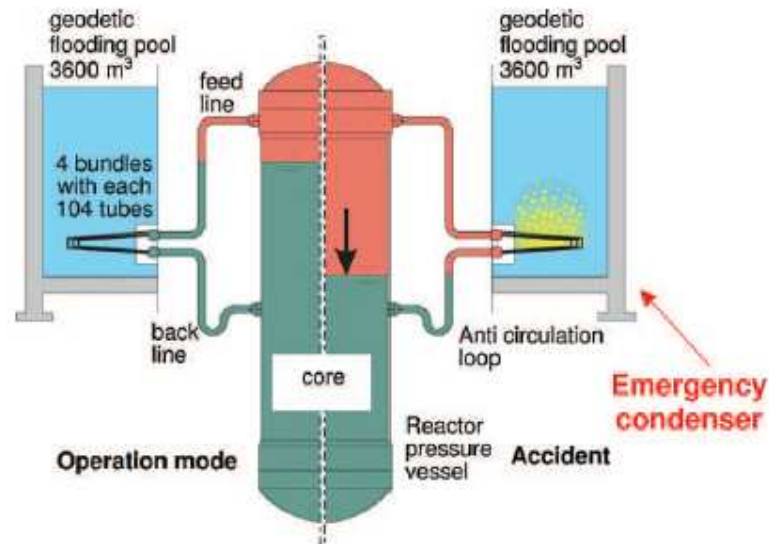


Figure 2.6: Operation schema of an emergency condenser (by Krepper and Beyer, 2010:3171)

The outcomes of Krepper and Beyer's (2010) investigation show that temperature stratification phenomena were observed, even in small-scale tests, with circulating fluid flows being the key role players. They observed single-phase hot fluid rising fast from the heated region and slowing down in the unheated section. Regarding steam they concluded that steam bubbles accelerated the liquid and caused disruption of the temperature stratification. In this present study it was observed and concluded that bubbly boiling at saturation conditions caused temperature oscillations, which seemed to be more severe when the system was opened to the atmosphere than when it was closed.

Jain et al. (2011) conducted an experimental investigation to study the impact of varying steam drum levels in a multiple loop natural circulation system of a pressure tube-type boiling water reactor. In their study, four loops were connected to the same header but different steam drums (see Figure 2.7). The outcome of their investigations was that mixing the flows from different quadrants empowered a reorganisation of flows to the loops. This triggered steam drum level deviations as a result of different pressure in the steam drums caused by feed water mal-distribution.

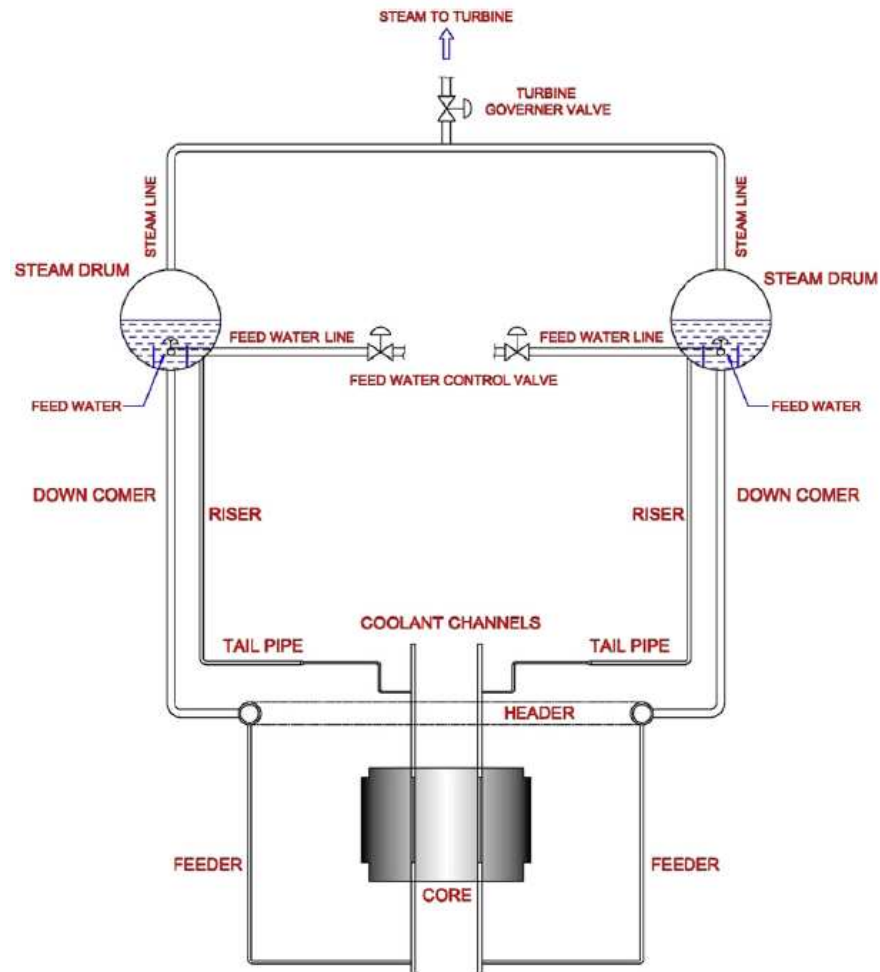


Figure 2.7: Main heat transport system (MHTS) facility (by Jain et al., 2011:2228)

Jain et al. (2011) concluded that connecting the steam drums to each other in both the liquid and steam regions was a necessity to ensure the same operating water level and pressure. In the present study, all three loops were connected to the same steam drum and header, which eliminated system instabilities due to steam drum pressure differences.

Vyas et al. (2010) experimentally studied the steady-state boiling natural circulation behaviour in a multi-parallel channel system. Their experimental setup consisted of 10 vertical electrically heated channels connected to a common steam drum, header and down-comer. In their investigation, they imposed various parameters on the system, i.e. channel power and down-comer resistance. The outcome of their study was that two-phase natural circulation did not always decrease with increasing down-comer resistance, but instead passed through maxima and minima (Vyas et al., 2010:3867).

They further observed that a zero-powered channel acts as a down-comer and transports fluid in the opposite direction to the heated channels (Vyas et al., 2010:3867). They concluded that unequally heated channels result in flow reversal. However, one of the conclusions of this study was that flow reversal eventually materialises between the channels, irrespective of subjecting the channels to equal power. They attributed this to be due to the considerable sluggishness of the coolant in the down-comer.

Furuya et al. (2005) conducted an experimental study of natural circulation behaviour in a boiling water reactor (BWR). They conducted the experiments to study two-phase flow instabilities associated with pressure during the start-up of a BWR. They observed and identified flashing-induced density wave oscillations at low pressure (Furuya et al., 2005:1557). They also concluded that the stability of the system during start-up improved with increasing pressure. This was also observed in the present study, when the system was operated as a heat pipe it experienced geysering followed by flashing-induced stability and became stable when operated as a closed system.

2.4 Theoretical Investigations of Natural Circulation Systems Instabilities

The instabilities of natural circulation were also investigated using simulation models of different systems. This was done so that the models could be used to predict natural circulation heat transfer under various conditions and to be able to make reasonable engineering judgements and improve designs, which is not possible when conducting an experiment. The question is: Are the models capable of describing the phenomena? The following paragraphs review theoretical natural circulation investigations conducted worldwide (this study inclusive) using different models. Conclusions drawn by the investigators are also discussed.

Lakshmanan and Pandey (2010) performed a numerical investigation of start-up instabilities of natural circulation in a parallel boiling system using the RELAP 5 model. They used simulation to investigate the effect of in-phase and out-of-phase flashing instabilities in parallel-channel systems under unequal and equal heating. They concluded that there are in-phase and out-of-phase interactions between channels.

Where unequal heating channel power exists, flow reversal was predicted in one channel, followed by a sudden surge due to flashing in another channel (Lakshmanan & Pandey, 2010:7). They further concluded that the model predicted a reduction in flow amplitude oscillations due to additional loss of heat transfer coefficient. In the present study, a one-dimensional model for two-phase natural circulation in double loop developed by Dobson (2006) and tested by White (2011) was extended to simulate two-phase natural circulation in a multi-parallel channel system.

There are a variety of programs/codes (RELAP 5, ATHLET, CATHARE, APROS, TRAC, etc.) that have been developed and currently are in use to predict the thermal hydraulic response of natural circulation flow. However, Dobson's (2006) code was decided upon as it was believed that it would serve as a simple, yet valuable, tool for the analysis of the single-phase and two-phase natural circulation flow of this study. Also, it was readily available and had been proven to predict experimental responses satisfactory in White's (2011) study. The outcomes of the present study predicted that, in the buoyancy regime, all channels behave in a similar manner. However, some channels assumed out-of-phase (opposite flow response) behaviour in the friction (boiling)-dominated region. The amplitude of the oscillations was indeed reduced due to the loss of coefficient at the header, down-comer and channels.

Nayak et al. (2006) numerically studied boiling natural circulation instability in an ethylene oxide chemical reactor system using the MONA code and compared the results to the performance of the plant's results. In their investigation they concluded that the model predicted the performance of the plant closest to the measured values. They predicted the system to be unstable at high power, which was associated with Type II instability, and increasing the riser's diameter triggered oscillation at low power. The model developed in the present study also predicted Type II instability at high power and buoyancy-dominated instability at low power.

Jiang et al. (1995) performed a simulation study on the start-up of the 5 MW nuclear heating reactor and observed geysering, flashing instability at pressures less than 0.3 MPa and low steam quality density wave instability. To overcome these instabilities at the start-up of the reactor, Jiang et al. (1995:122) suggested that the reactor pressure be increased at the initial stage by using nitrogen gas.

Yun et al. (2008) and Zhang et al. (2009) performed theoretical investigations on two-phase instability in a multi-parallel channel system. The outcomes of their studies were that such systems possess chaotic characteristics (damped, periodic and divergent oscillations) and further investigation to find out why it has to be carried out in the future using non-linear dynamics (Yun et al., 2008:676; Zhang et al., 2009:9). According to Yun et al. (2008:676), increasing the inlet resistance coefficient can stabilise the system. In the present study, the simulation outcomes did not possess any serious chaotic behaviour at start-up, except for some minor transient start-up response. The chaotic behaviour was observed at a mature stage of each test (see the simulation results section) and the results seemed to be in good agreement with the experimental results.

Goudarzi and Talebi (2013) performed linear stability analysis of a double-channel two-phase natural circulation loop to investigate the effects of different parameters on the steady-state and transient behaviour of the system. Figure 2.8 shows the double-channel loop they investigated.

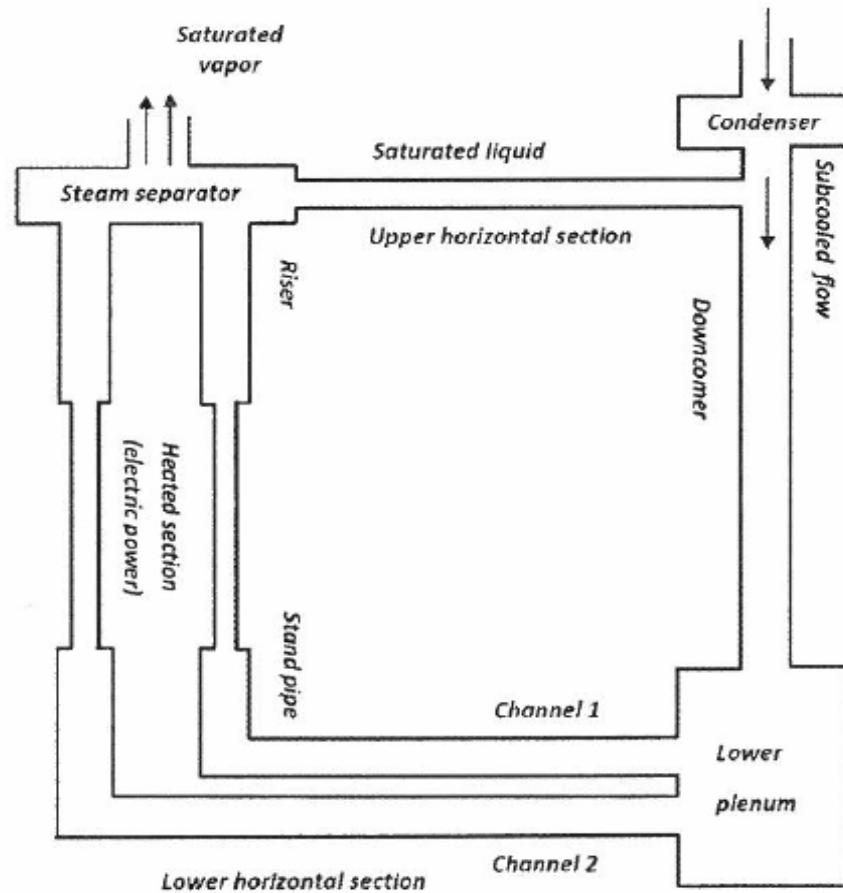


Figure 2.8: Double-channel two-phase natural circulation loop (by Goudarzi & Talebi, 2013:116)

Goudarzi and Talebi (2013:123) concluded that the use of a two-phase friction multiplier in the decay ratio criterion improved the stability of their results and gave good experimental result approximation compared to the results obtained by Lee and Pan (2005). Goudarzi and Talebi (2013:123) further predicted the existence of Type I instability in the low power regime and Type II instability in the high power region.

Rao et al. (2006) performed steady-state investigations of a two-phase natural circulation system in a single-loop and double-loop system respectively. They used uniform heat flux for heating and cooling, along with constant physical properties, uniform pressure inside the loop and water-steam as the working fluid (see Figure 2.9). Their findings show that an increase in power does not always result in an increase in mass flow rate (Rao et al., 2006:1051). They discovered that the flow rate rather increased with the height of the loop, although with the heat flux first increasing to reach the maximum and then falling. They concluded that the surface heat flux should match the loop geometry and other operating parameters to produce the maximum flow rate.

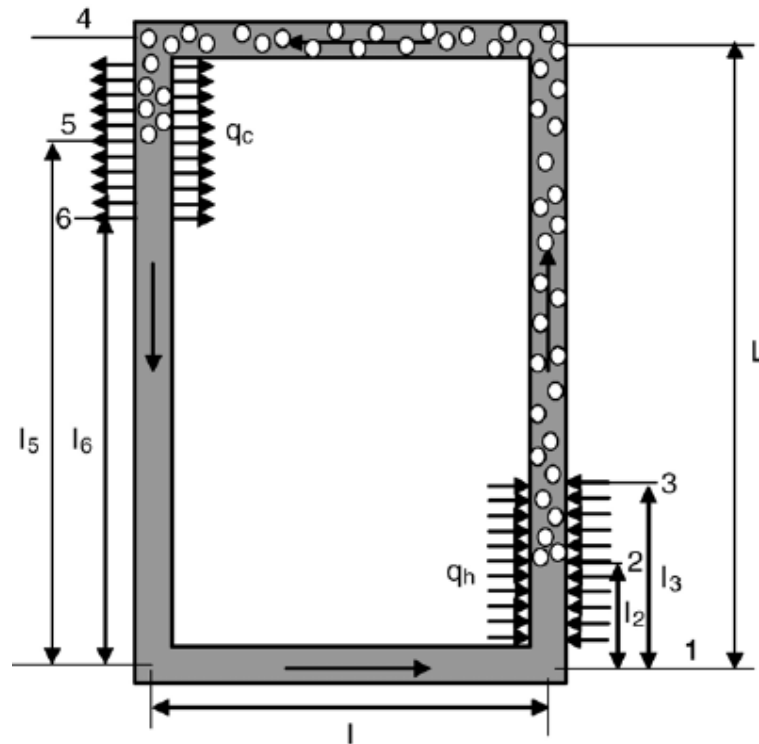


Figure 2.9: Schematic diagram of a two-phase natural circulation loop (by Rao et al., 2006:1043)

The outcomes of the studies by both Rao et al. (2006) and Goudarzi & Talebi (2013) are similar to the conclusions drawn from the theoretical model in this study (see Chapter 6). A Two-phase friction multiplier was also used in the numerical model of this study, as it is believed to have to make major contributions in approximating the experimental conclusions.

3 EXPERIMENTAL WORK

One of the objectives of this study was to perform practical investigations of the instabilities of single- and two-phase flows in a multi-channel thermosyphon loop. Multi-parallel channel natural circulation systems are utilized in many energy-generation systems for cooling purposes e.g. nuclear reactor cooling systems has multiple heated risers and cooled down pipes connected to various manifolds and headers. In this goal, a four parallel-channel natural circulation loop was designed, constructed and tested. This chapter outlines the experimental design and setup, the calibration of all the instruments used and the experimental procedures.

3.1 Experimental Design

In this context, a parallel channel loop was designed and built to investigate the instabilities of a multi-channel thermosyphon loop. Three heating sections were chosen based on the conclusion drawn by Lee and Pan (1999:32), which states that “a 3 channels plus system exhibits instability characteristics fairly similar to a 2-channel system”. White (2011) performed an investigation of two-phase flow instabilities in a dual-channel system. Comparing the outcomes of this study with White’s (2010) findings and verifying the conclusion drawn by Lee and Pan (1999:32) was one of the objectives of the present study. The geometric configuration of the experiment (see Figure 3.1) was chosen based on the water reactor cooling concept (multiples of heat removal pipes).

The loop comprises three identical parallel channels, connected between a steam drum and header, see Figure 3.1. A single down-comer, connected between two common plenums, i.e. the steam drum and header, provides the recirculation path. The steam drum forms the top plenum, while the header takes the bottom part of the setup to enforce natural circulation. The condenser was placed inside the steam drum to increase efficiency. Risers were electrically heated independently at the bottom by means of heating elements. Independent powering of the heating elements was achieved by using three separate rheostats. The purpose of using three rheostats was to be able to control the heating elements independently and subject the system to unequally heated risers if need be. Heating the system at the bottom was chosen to accelerate the water-vapour mixture upward by buoyancy force into the steam drum, where cooling and separation of liquid and vapour will take place through gravitational settling.

In the steam drum, the vapour condenses and comes down as water droplets, mixing with the saturated water in the steam drum. The condensed liquid and saturated water mixture accelerate downward by force of gravity, through the orifice flow meters, and becomes heated again in the risers, and the flow recirculates. The orifice flow meters are located at the header to measure the flow rates into the risers and the down-comer.

The flow meters are connected to an electrical data logger which is connected to a computer where the data is captured and stored at 10-second intervals. Thermocouples are inserted to measure the temperatures at the top and bottom of the risers and down-comer, on the steam drum and at the inlet and outlet of the condenser. The thermocouples are also connected to the data logger. The pressure drop is measured at the header using differential pressure sensors across the orifice flow meters. In addition, a pressure gauge was installed on the steam drum to measure the system's pressure.

The steam drum was the preferred positioning of the pressure gauge because it is the highest part of the system, hence it will be easier to take pressure readings. The pressure gauge was also used to monitor the safety of the system during operation. As more heat is transferred into the system, pressure builds up and, if not monitored and engineered correctly, might lead to the system exploding. To ensure the safety of the system during operation, a safety valve was installed on the steam drum. The safety valve was set to operate when the pressure gauge reads greater than 110 kPa.

To relieve excess pressure build up inside the experimental set up, the header was connected to an expansion tank open to the atmosphere. The expansion tank was connected to the header via a transparent pipe with a ball valve. It was decided to have a transparent expansion tank pipe so that the water level could be measured and expansion and contraction of the system could be observed. The purpose of the header ball valve was to be able to operate the system at different modes. Another ball valve was installed on the steam drum to evacuate air trapped inside the steam drum during system fill up. Two-phase flow is unstable in nature, hence a well-balanced holding frame was designed and built to hold the system (the four loops, expansion tank and steam drum) together, even under unstable events. Figure 3.1 shows a view of the experimental setup.

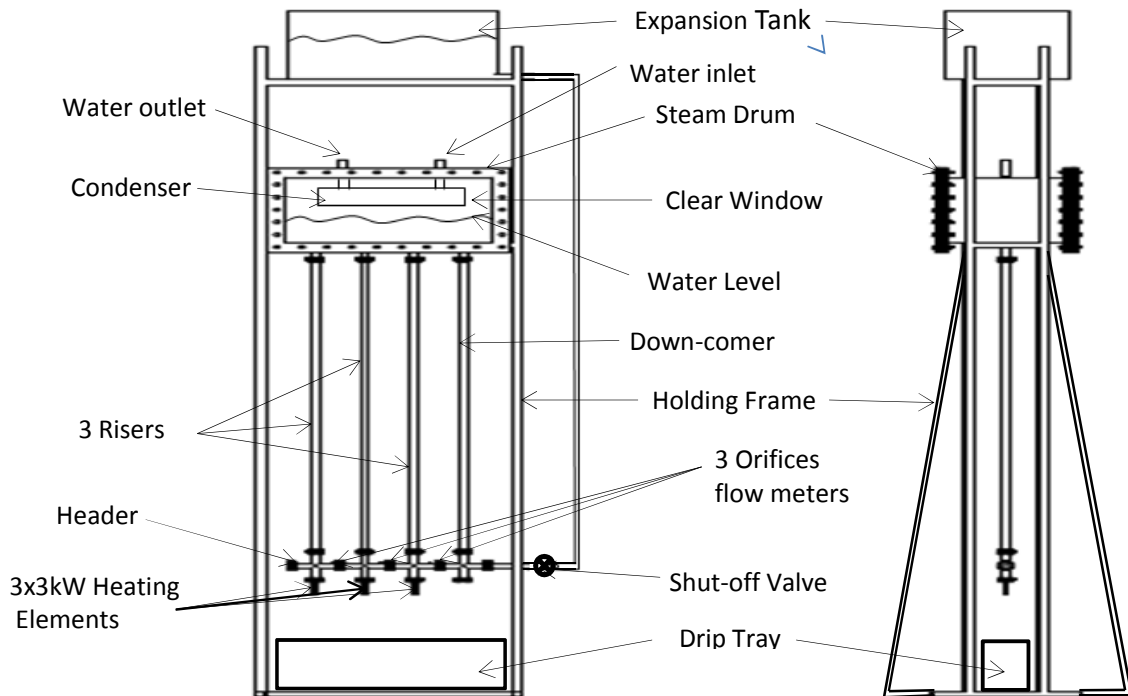


Figure 3.1: Experimental setup view

The geometric details of various components used in the experimental facility are provided in Table 3.1. The photographic view of the experimental setup is included in Appendix D.

Table 3.1: Geometric dimensions of the experimental facility

Component	Dimensions (mm) and Orientation	Quantity
Expansion Tank	400 w x 420 h x 700 L x 3 thick, Horizontal	1
Steam Drum	386 w x 400 h x 700 L x 3 thick, Horizontal	1
Condenser	200 w x 110 h x 400 L x 3 thick, including 7 x 28 OD x 3 thick x 290 L, Horizontal	1
Risers	28 OD x 1.5 thick x 1993 L, Vertical	3
Down-comer	28 OD x 3 thick x 1993 L, Vertical	1
Header	28 OD x 3 thick x 664 L, Horizontal	1
Orifice	30 OD x 12.5 ID x 2.5 thick	3
Heating elements	12.5 OD x 210 Cold L x 1000 Hot L, Vertical	3
Dripping Tray	794 w x 200 h x 1400 L x 1.6 thick, Horizontal	1
Holding frame	900 w x 4000 h x 1500 L, Vertical	1

To study the behaviour of the natural circulation flow, it was deemed necessary to visually observe the flow behaviour during operation. To achieve this, the header, risers, down-comer, front and back sides of the steam drum were made out of transparent material (polycarbonate). Polycarbonate is plastic which, when subjected to continuous high heat, is likely to deform slightly.

In this event, the electrical heaters inserted in the risers were likely to touch the plastic tube for a prolonged time and melt it, even though the system was engineered properly. This could put the system operator and the surroundings in danger, particularly as the system operates with both hot water and electricity. To prevent unforeseen unfortunate situations, a shielding frame (not shown in Figure 3.1) with transparent polycarbonate sheets was designed and constructed to house the entire system. The protection frame was equipped with transparent sheets to maintain a clear view of the system. The shielding frame also ensured that the electrical instruments were isolated from the water.

Thermal insulation was eliminated in the experimental setup because most of the system's components were purposely made transparent, and insulation would have blocked the view. The material and instruments used were selected based on certain engineering aspects, such as reducing thermal losses to the environment while meeting the desired purposes (clear view). The following section outlines factors considered in selecting material for the different components of the system and the instruments used in performing the experiments.

3.2 Materials and Instruments Selection

The main objective of the technical study was to visually observe the behaviour of the flow. To achieve this, a transparent material had to be used to build the loops of the experimental system. The material to be selected had to be clear and able to operate continuously at temperatures above 100°C, and to be able to handle pressures of more than atmospheric pressure. The system's working fluid (water) was required to reach boiling for two-phase flow with high quality to be generated and water attains boiling at 100°C at atmospheric conditions. There was not too much flexibility in terms of getting a material that will meet the specifications. The material would have to be either plastic or glass. The plastic material that is highly temperature resistant is polycarbonate. The properties of both glass and polycarbonate are presented on Table 3.2.

Table 3.2: Properties of glass and polycarbonate materials

Properties	Polycarbonate plastic	Pyrex Glass
Max. Operating temperature	110 °C	230 °C
Coefficient of thermal expansion	$6,5 \times 10^{-5}/^{\circ}\text{C}$	$32.5 \times 10^{-7}/^{\circ}\text{C}$
Thermal conductivity	0.2 W/mK	1.1 W/mK
Softening temperature	149 °C	821 °C
Density	1200 kg/m ³	2230 kg/m ³
Machinability	Yes	Difficult

Compared to polycarbonate, Pyrex glass operates at fairly high temperature without concerns of material softening. However, glass has the disadvantage of machinability difficulties.

Polycarbonate material was preferred over glass as it is not only light, but can also easily be machined, extruded and joined together. Thermal conductivity was also one of the deciding factors for the clear material to be used. Polycarbonate has exceptional low thermal conductivity of only 0.2 W/mK, compared to glass with 1.1 W/mK conductivity. Low thermal conductivity means less heat losses to the environment. The only challenge was to get polycarbonate tubes locally and even outside the country (South Africa). We could not find a company that supplies tubes made out of this material in South Africa, and international companies were either supplying it in bulk or had difficulties to outsource it as a result of laws and regulations. The polycarbonate tubes were eventually sourced from Gilbert Curry Industrial Plastics Co Ltd, United Kingdom.

Experimental geometry

The risers, down-comer and header were made of clear polycarbonate tubes, while the front and back of the steam drum were made of clear polycarbonate sheets. The steam drum was rectangular in shape so that it was easier to construct. The sides of the steam drum were made of stainless steel W304 to prevent rust forming and discolouring the working fluid.

The polycarbonate sheets were fastened onto the stainless steel flanged front and the steam drum. Figure 3.2 shows the steam drum, risers, down-comer, and the steam drum/header dimensions.

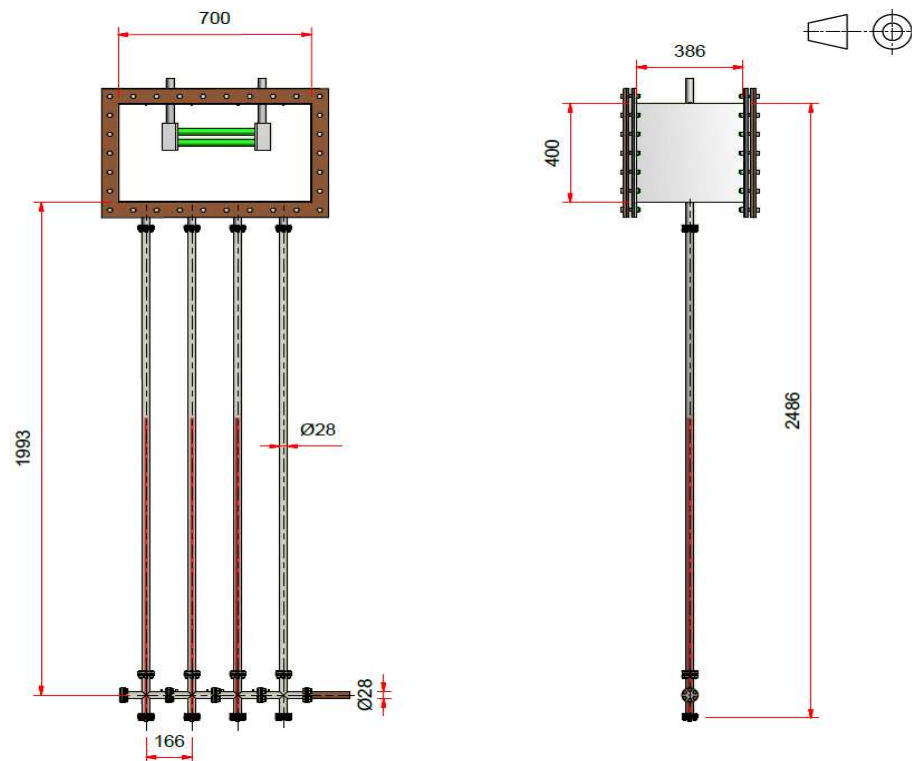


Figure 3.2: Experimental setup drawing

Expansion tank

The expansion tank was sized such that it was capable of carrying all the water in the steam drum and pipes. The system used the expansion tank to relieve pressure build-up. It was also used to add water to the system should the water level in the steam drum drop. The expansion tank was positioned above the steam drum to ensure that water ran into the system by gravity. The material used to construct the expansion tank was stainless steel because of its good anti-corrosion capabilities.

Heating method

The experimental system had three vertical heated channels connected to the steam drum. The heating was achieved by inserting three independent electrical heating elements into the bottom of each riser. Electrical heaters were a preferred option, as heat is controllable and has a fixed heat flux.

The heating elements were independently controlled and could be set to different powers using three separate rheostats. The heating elements were designed and manufactured specifically to meet the requirements of this study. Figure 3.3 shows the details of the designed electric heating elements.

The heater runs centrally through each riser from the bottom vertically up. The cold length was specified to run until just above the header and the rest of the rod to be a heated section. The outer shell material was specified to be stainless steel to reduce rust and corrosion rates, since the elements would be immersed in water. The heating elements were designed so that they should be connected with bolts to the cross-piece flange.

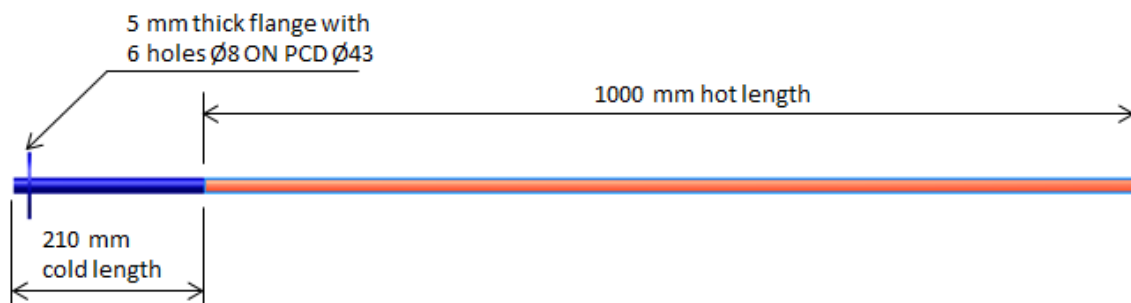


Figure 3.3: Electric heater details

Cooling method

A water condenser was sized and designed so that it was capable of removing the maximum power (9 kW) supplied into the system. The detailed design calculations for the condenser can be found in Appendix A. Different materials were considered to construct the condenser. Since water is corrosive, a corrosion-resistant material had to be used to construct the condenser.

Stainless steel and copper materials were considered for making this choice. Copper is known for its low reactivity (corrosion resistant), is ductile and a good thermal conductor (401 W/mK), while stainless steel is high in strength, self-defensive, hard and corrosion resistant, although it is not a good conductor of heat, with approximately 14.9 W/mK conductivity. Stainless steel's hardness increases machining costs and the low thermal conductivity property makes it less attractive for this application.

Copper was the preferred material for the condenser because is a good conductor of heat, easy to machine and join, affordable and available. Figure 3.4 shows the condenser view and configuration. The staggered condenser configuration was adopted to increase effectiveness.

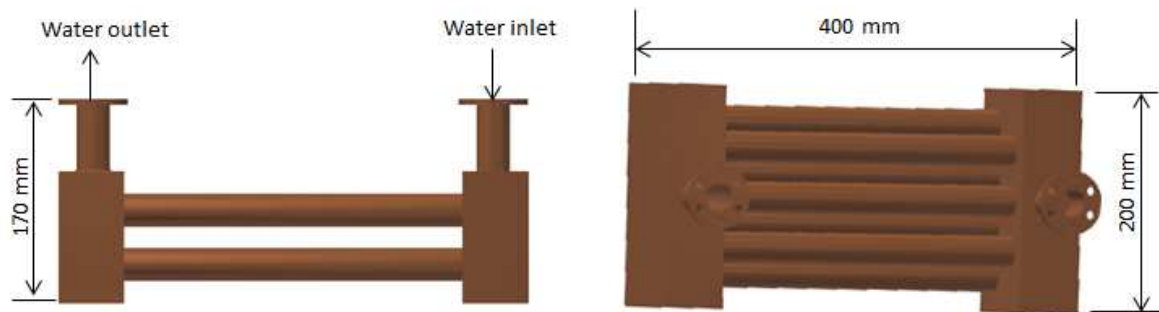


Figure 3.4: Condenser with 7 staggered \varnothing 15 mm tubes in two rows

Flow measurements

Fluid flow rate is one of the important parameters in studying the behaviour of natural circulation systems. Amongst plenty of flow measuring technologies, flow measurements device options were limited to only venturis and orifices.

The following summarises the factors that were considered for each flow meter type in deciding on the best option:

- Venturi meter
 - Requires modification to measure flow in both directions i.e. three pressure measuring points are required hence wider neck/nozzle
 - Not easy to build because of the nozzle's shape which requires extra effort to machine.
 - Low pressure head losses because there is no flow obstruction
 - More expensive than orifice meter because it is difficult to machine
- Orifice meter
 - High pressure losses because of the meter obstructing the flow
 - Easy to build because of its shape simplicity
 - Costs less than venturi meter because it is easy to machine

- Can be used to measure flow in both directions

The orifice meter was chosen as a flow obstruction device because it measures flow in both forward and reverse directions without modifications. Its low cost and easy manufacturing characteristics give flexibility to have different sizes if required to change the flow meter size. It also is easy to install and remove from the system.

Three identical orifice meters were designed based on the flow tube size where the flow meters were to be installed. The inner diameter of the orifice meter was decided to be half of the internal diameter of the flow tube, at 25 mm ID. Figure 3.5 shows the orifice meter

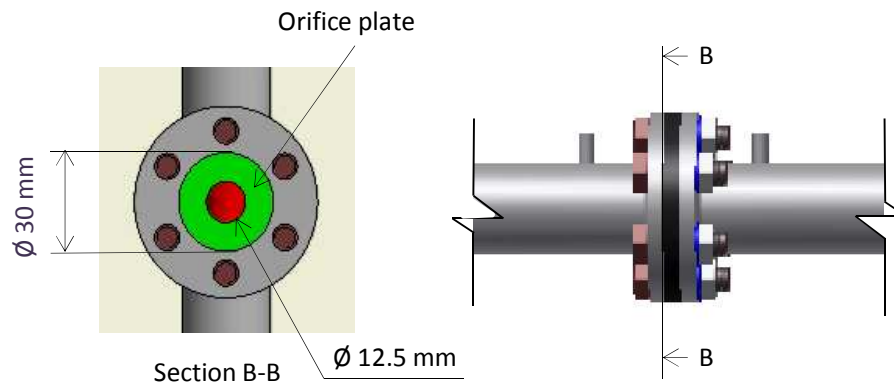


Figure 3.5: Orifice flow meter drawing and representation

The orifice meters were placed at the ends of the cross-piece connecting tubes, as shown in section B-B. The pressure drop was measured in front and after the orifice meter using differential pressure sensors. Flow rates through the risers and down-comer were calculated using the measured differential pressure sensors outputs and governed equations (see orifice calibration results). Brass material was used to construct the orifice meters because of its corrosion resistant capability.

Pressure sensors

Pressure sensors were required to measure flow rates through the channels and down-comer of the system. The pressure-measuring device to be used was required to be highly sensitive to capture the dynamics (signals) of the flow fast enough and send them to the data acquisition unit.

Two options were considered for obtaining the pressure drop across the flow meters. One was to use three differential pressure sensors which would provide pressure drop instantly. The other choice was to use six absolute pressure sensors, two sensors per flow meter, and calculate the difference between the two pressure points.

Both methods were viable except that one required more effort than the other. For instance, three absolute pressure sensors would have been used for the venture meter, workout the pressure difference between the nozzle and the front of the meter as well as between the nozzle and the back of the venture meter, and compare the two differential pressure values to be able to identify the flow direction. The specifications of both differential and absolute pressure sensors are presented in Table 3.3. The differential and absolute pressure sensors were readily available at the Stellenbosch University Mechanical Engineering Workshop.

Table 3.3: Performance comparison of differential and absolute pressure sensors

Sensor	Differential Pressure Sensor	Absolute Pressure Sensor
Product Maker	Honeywell Model Z	Honeywell 40 PC
Features		
Operating Temperature	-54 to 121°C	-45 to 125°C
Accuracy	+/-0.25% full scale	+/-0.2% full scale
Output	+/-5VDC	0V-4VDC
Sensitivity	2mV/V	40/133 mV/Pa
Max. overpressure	20.6 MPa	22.6 kPa
Repeatability	+/-0.05% full scale (non-repeatability)	+/-0.15% span
Linearity	+/-0.15% full scale	+/-2.00% span
Operating media	Gas, liquid	Dry gases only

High temperature (above 80°C) and water operation capabilities of the pressure device were among the requirements. Other major concerns included accuracy and sensitivity of the device. Table 3.3 shows that the absolute pressure sensor had relatively high operating temperatures and sensitivity, but worked with dry gases only.

Manometer for calibration purposes

The differential pressure sensors were calibrated with an Essen® Betz type 5000 micro-manometer. The micro-manometer was readily available at the Stellenbosch University Mechanical Engineering Laboratory and is considered as of the best devices for the calibration of pressure-measuring instruments with high accuracy. The specifications of the micro-manometer used are listed in Table 3.4.

Table 3.4: Betz 5000 micro-manometer

Specifications	Betz type 5000
Maker	Essen®
Range (in Pascal)	-100 to 5000 Pa
Accuracy of the read-out	0.04% FS
Resolution	0.2 Pa
Max. static pressure	100 kPa
Calibration temperature	20°C
Measuring liquid	Demineralized water with wetting agent

Temperature sensors

There were a wide range of options to select from when it came to a temperature measuring instrument. Amongst these options were thermistors, thermocouples and resistance temperature detectors (RTD). Thermocouples were selected because they are believed to render high accuracy, and the thermocouple calibrating unit was readily available at the laboratory. T-type thermocouples were used, as they measure acceptable temperatures even at high temperature (see the calibration results, section 3.3.3). The specifications of the thermocouples type T used include simplex, probe of diameter 3.0 mm, stainless steel 316, completed with potted seal (incl. relief spring) and Teflon-insulated flylead rated up to 250°C.

Agilent® data acquisition unit

There were two types of data acquisition units to select from that were readily available at the laboratory. The data acquisition unit to be used had to be able to connect all the thermocouples and pressures sensors on one card. It had to be able to be connected, and to log and continuously update data on a computer. The data acquisition unit had to respond fast to capture density wave oscillation instability. This would mean the unit had to be capable of detecting frequencies from as low as 1 Hz to 10 Hz. Tables 3.5 and 3.6 show the summaries of the specifications used to decide on the data acquisition unit.

Table 3.5: Agilent® data acquisition unit specifications

Product Code: 34972A	
Charecteristics	Specifications
Input channels	60 x 2 wire channels
Maximum sampling rate	2 GHz
Resolution	22-bit
Analog Output	+/- 10Volts @ 20mA
Usage	Laptop/Desktop
Connectivity	USB /LAN/IntuiLink Software/BenchLink/LXI Compliant

Table 3.6: Eagle® data acquisition unit features specifications

Product Code: USB-30A16-73T16	
Characteristics	Specifications
Input channels	16/32 Single Ended
Maximum sampling rate	250 kHz
Resolution	14-bit
Analog Output	+/- 10Volts @ 5mA
Usage	Portable/Laptop
Connectivity	USB

The Agilent data acquisition unit was chosen as it did not only have many (20) channels on one card and a high resolution, but it also had a screen to read, to monitor the setup and to measure values directly, unlike the Eagle unit. The Agilent data acquisition unit also offered a front panel for manual setup control and settings. There were quite a number of advantageous features offered by the Agilent data acquisition unit.

Connection

The polycarbonate parts were joined together using water-resistant Pratley® glue, as high temperature capabilities was the main requirement of the glue to be used. Obtaining a glue that operates continuously at temperatures above 80°C was a challenge. Other means such as transparent silicone gel had to be used to assist the glued parts adhere together and eliminate leaks at temperatures above 100°C. The flexibility of polycarbonate made it possible to join the risers and down-comers to the stainless steel drum part with bolt connections. High temperature-resistant silicon rubber was used to seal all intersections to make the system airtight and prevent water leakage.

3.3 Calibration of Instruments

To ensure that all instruments used in the experimental setup were measuring accurate results, each of them was calibrated. The calibration setup, procedures and results of all instruments are presented in the following sections.

3.3.1 Calibration setup

This section outlines the calibration setup for all the apparatus (pressure sensors, orifices and thermocouples) that were used to perform the experiments. The calibration setup for each instrument is presented below.

Pressure sensors

Three differential pressure sensors were used for the experiments, one for each orifice. A special setup was done to calibrate the differential pressure sensors. The calibration was done using a micro-manometer to measure extremely small differential pressures. The differential pressure sensors were calibrated at the same time, receiving the same input from the micro-manometer. The differential pressure sensors were subjected to the same input during calibration because they would be receiving the same input when the experiments were being performed.

The differential pressure sensor signals were measured using an Agilent data acquisition unit. However, the sensors had a different connection port to the Agilent data acquisition unit port and could not be connected directly. Hence, three data amplifiers had to be used to link the to the data acquisition unit independently. The calibration setup of the sensors is shown in Figure 3.6.

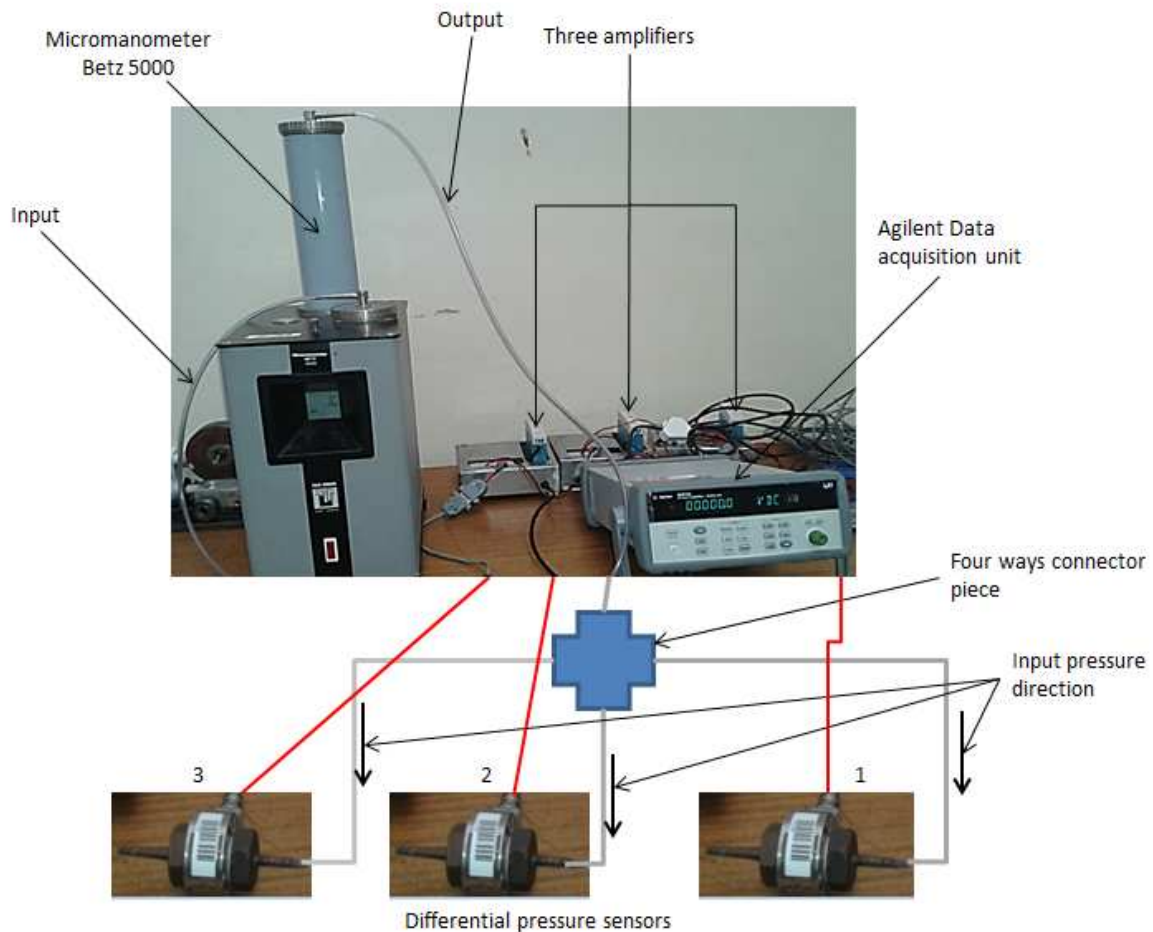


Figure 3.6: Differential pressure sensors calibration setup

The amplifier used in the calibration of an individual differential pressure sensor was assigned to that pressure sensor for the entire duration of the calibration and to perform the experiments. This was done so that there were no discrepancies in the output data as a result of different instrument usage.

Orifice flow meters

The three orifice flow meters were calibrated using the experimental setup, with the inlet connected to the tap and the outlet side connected to the drain, as shown in Figure 3.7. A weight scale and stopwatch were used to measure the mass flow rate, which was then converted to volumetric flow rate. The weight scale method of measuring the flow rate is considered the most accurate way of measuring flow rate, hence was used to calibrate the three orifice flow meters.

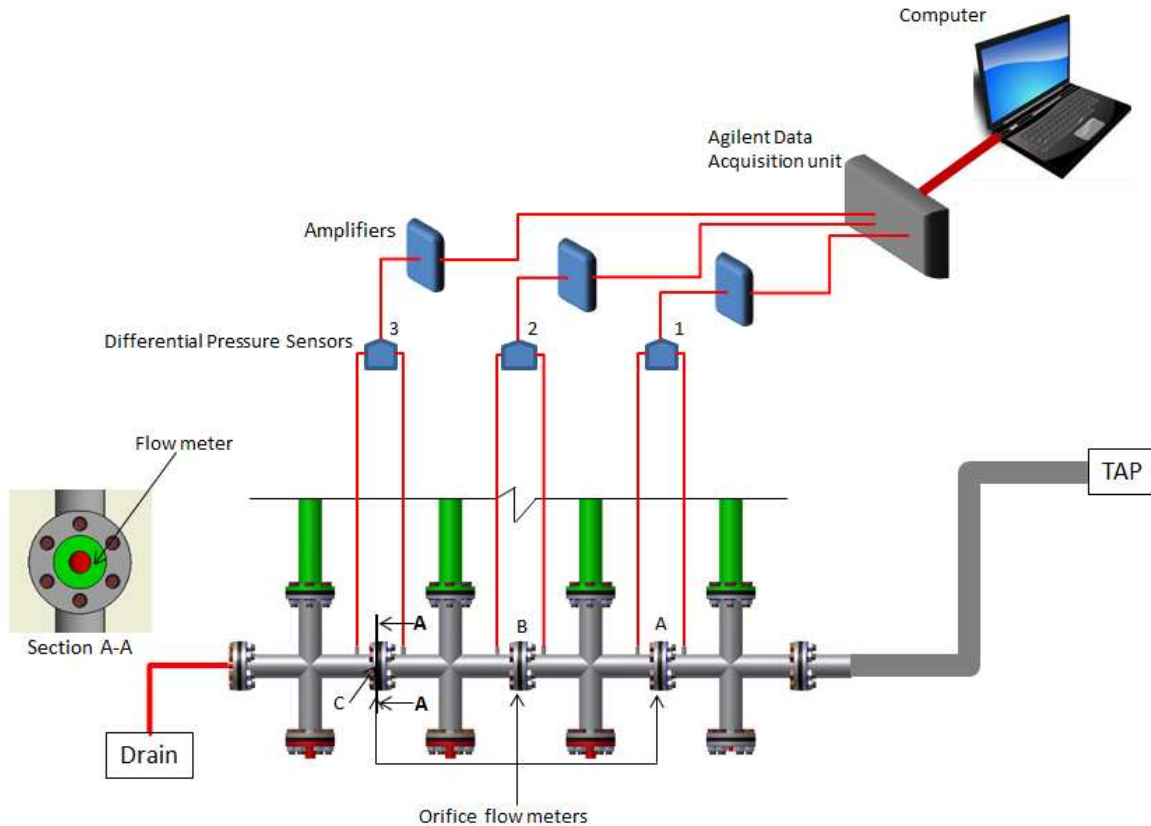


Figure 3.7: Orifices calibration setup

The differential pressure sensors were placed at a fixed position, approximately the same height as the orifices but away from the orifices. This was done so that both the orifices and differential pressure sensors were at the same absolute pressure point and to prevent water from accidentally spilling onto the sensors. The pipes connecting the sensors to the orifices were made short to minimise air bubbles from stacking into the pipes, causing problems in measuring minor differential pressures.

Thermocouples

The thermocouples were calibrated using a Fluke Field Metrology Wells (FMWs) unit, a calibrated platinum resistance thermometer (PRT), a Hewlett Packard multi-meter and an Agilent data acquisition unit. The Field Metrology Wells (FMW) unit was preferred to an oil bath system to set the thermocouples at different temperatures because FMW is easy to use and responds quickly to temperature variations.

3.3.2 Calibration procedures

This section presents the calibration procedures that were followed to calibrate all the instruments (pressure sensors, orifices and thermocouples) that were used to perform the experiments.

Pressure sensors

The three differential pressure sensors were connected to the micrometer at the same time by means of a four-way connector, the fourth way being connected to the micrometer. Each sensor was connected to the micrometer on one side and the other side was open to atmospheric pressure. The sensors were measuring differential pressure between the pressure input from the micro-manometer and the atmospheric pressure, while the micro-manometer was measuring the water level in millimetres, which was then converted to pressure by the hydrostatic pressure equation ρgh .

Prior to calibration it was ensured that the pipes connecting the micro-manometer to the sensors did not contain trapped pressurised air and that they sealed properly to the pressure sensors and the micro-manometer. The pressurised air in the pipes was released by disconnecting the pipes to allow air to escape. The calibration started by adjusting the micro-manometer to zero and recording the readings of the sensors. Different pressure levels were then applied to the micro-manometer. Every time pressure was applied to the micro-manometer, the amplifier received signals from the differential pressure sensor and sent them to the data acquisition unit. The data acquisition unit would then give the differential pressure sensors outputs in terms of direct current voltage.

Orifice flow meters

The calibration of the orifice flow meters started by ensuring that the experimental system was clean and free from solid particles that might hinder the flow, causing wrong measurements. The water was injected into the system by connecting the system to the tap on one end and connecting the other end to the drain. The water was injected into the system at different flow rates to check the effectiveness of the orifice meters. Every time the flow rate was changed, it was allowed to stabilise (2 minutes) and water was collected in a bucket, recording the collection time when the water was exiting the system.

The captured water was then weighed on a weight scale. The value measured by the weight scale in kilograms was converted to mass flow rate in kilograms per second. Three measurements were taken at each flow rate to verify the flow stability. The differential pressure sensors were sensing pressure drops across the orifices and sent the data to the data acquisition unit, where it was captured and stored on the computer.

Thermocouples

The thermocouples and the calibrated platinum resistance thermometer (PRT) were inserted into the electrically heated FMW unit. The thermocouples sent signals to the Agilent data acquisition unit and the PRT sent signals to the HEWLETT PACKARD 34401A data acquisition multi-meter. The FMW temperature was initially set at 20°C, after which it was increased in increments of 10°C.

Each time the temperature was increased, the FMW unit was given at least 10 min to heat up and stabilise at the new temperature.

3.3.3 Calibration results

Pressure sensors

The results obtained were plotted to see the correlation between the micro-manometer results and the pressure sensor results (see Figures 3.8, 3.9 and 3.10). To verify that the sensors were measuring correct results, a curve formed from the micro-manometer results and each differential pressure sensor was expected to be linear. The data obtained from each differential pressure sensor was linear to the pressures measured by the manometer, as indicated by the linear regression line in Figures 3.8, 3.9 and 3.10.

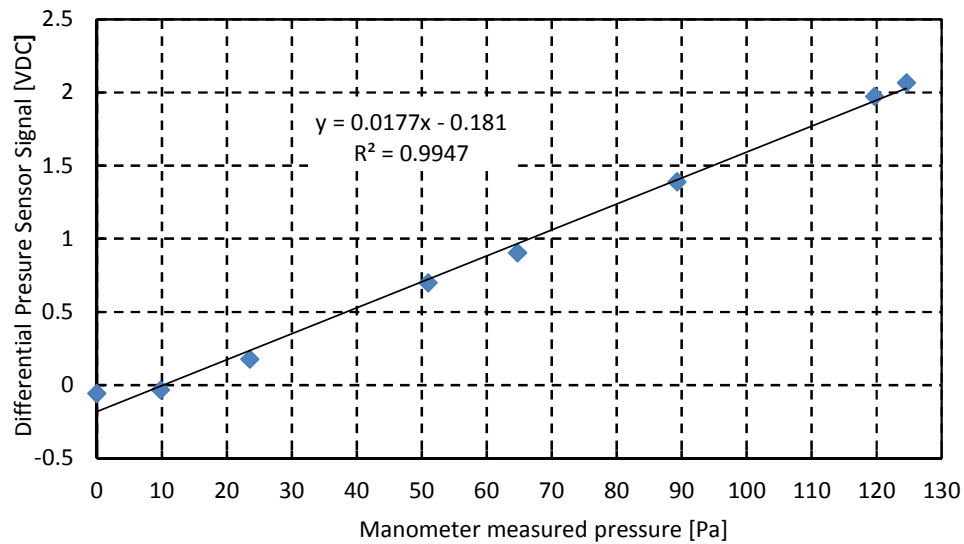


Figure 3.8: Differential pressure sensor 1 calibration results

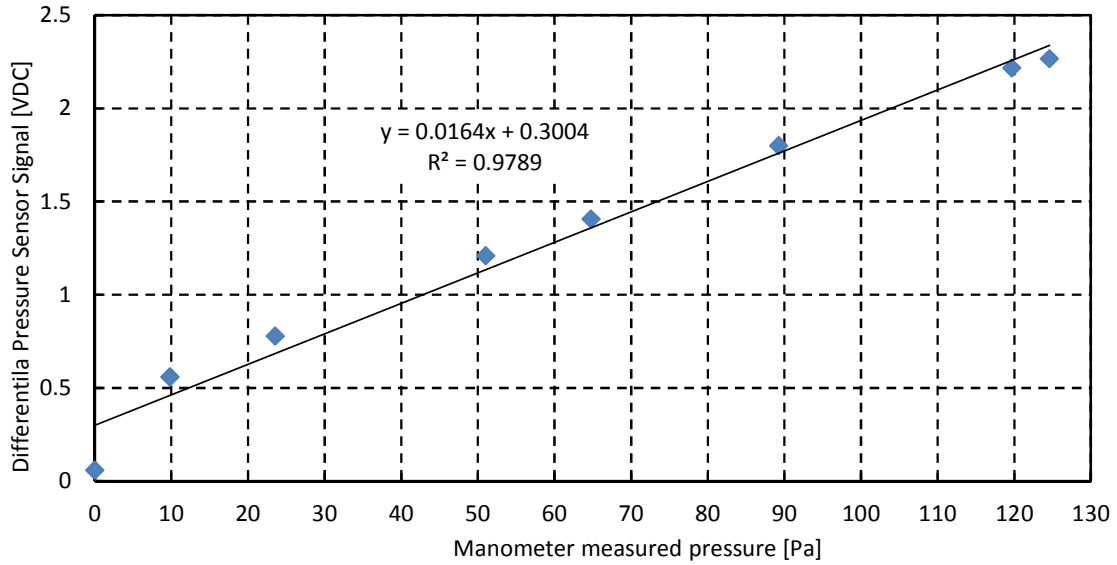


Figure 3.9: Differential pressure sensor 2 calibration results

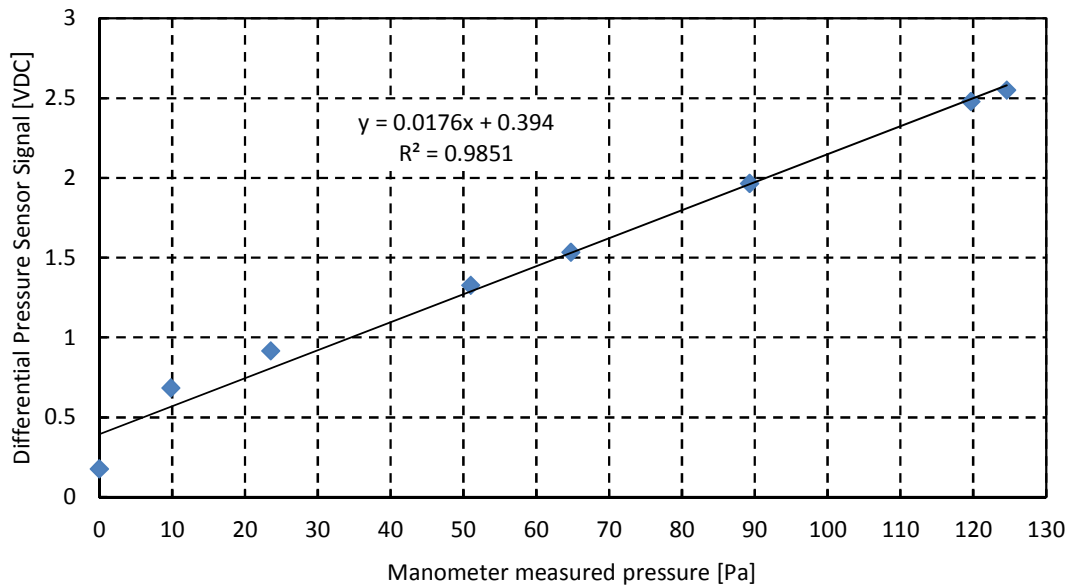


Figure 3.10: Differential pressure sensor 3 calibration results

The stated R^2 value for each differential pressure sensor is approaching unity, thus indicating that the data fits the linear trend very well. This means that the manometer measured pressure in Pascal (Pa) is directly proportional to the differential pressure sensor signal in Volts direct current (VDC). The calibration results also show that the differential pressure sensors are sensitive even at low pressures. Figures 8, 9 and 10 show good correspondence for all three differential pressure sensor calibration curves, with nearly the same values across the range of pressures. However, uncertainties are expected since the pressure was not practically equally divided across the four-ways connector piece.

The calibrated pressure sensors were then used in the calibration of the orifice flow meters and to perform the experiments.

Orifice flow meters

Some may argue that orifice flow meter calibration is not necessary, but according to Cengel and Cimbala (2006:383), meter calibration is required because the flow separates from the lip of the orifice and creates a flow tube narrower than the orifice diameter. The three orifice calibration results were plotted and are shown in Figures 3.11, 3.12 and 3.13.

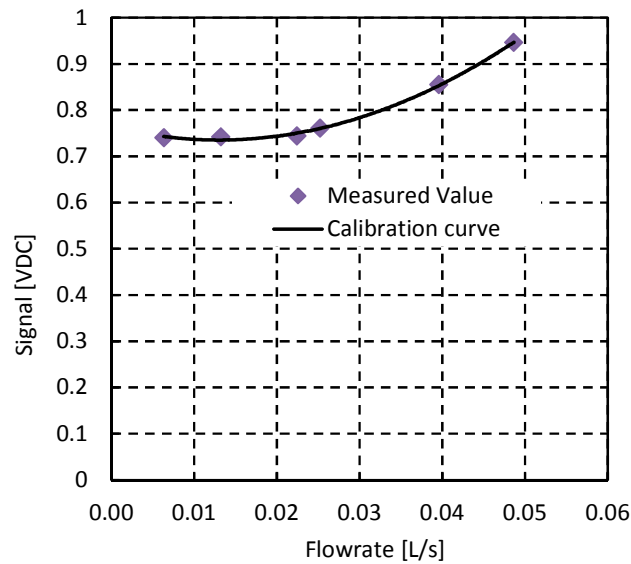


Figure 3.11: Orifice A calibration results

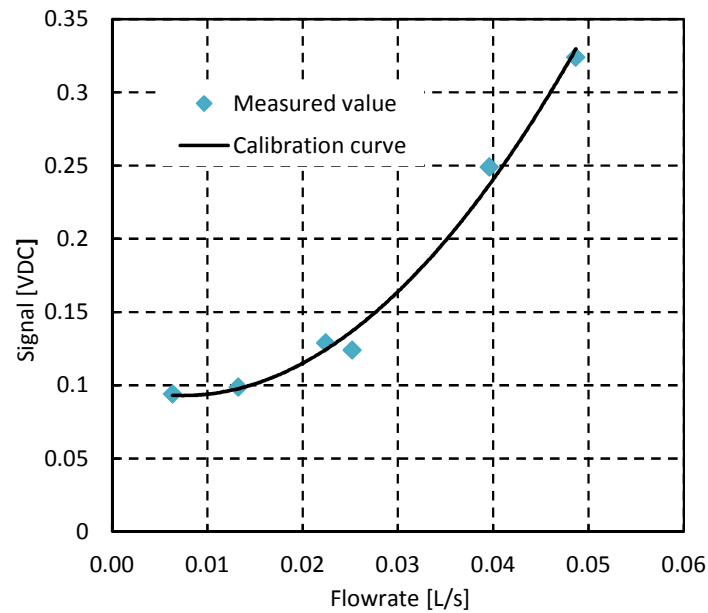


Figure 3.12: Orifice B calibration results

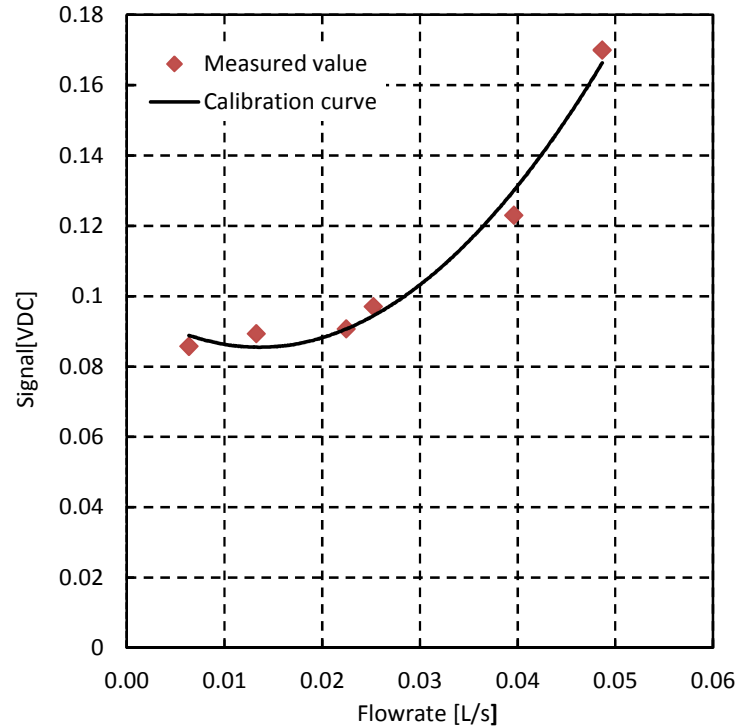


Figure 3.13: Orifice C calibration results

The above three figures show the voltage signals of the differential pressure sensors against the measured flow rate in the orifices in the direction of flow. The plotted data was also fitted with a quadratic curve for each graph. The quadratic equations resulting from the quadratic curves fitted are as follows:

- Orifice A: $y = 166.14x^2 - 4.3158x + 0.7634$ $R^2 = 0.9974$
- Orifice B: $y = 138.86x^2 - 2.0518x + 0.1006$ $R^2 = 0.9917$
- Orifice C: $y = 65.609x^2 - 1.7785x + 0.0975$ $R^2 = 0.9825$

where x represents the volumetric flow rate in litres/second and y denotes the differential pressure sensor signal, in direct current Volts. Figures 3.11, 3.12 and 3.13 show that the quadratic curves fit the data very well, and this is also indicated by the values of R-squared approaching unity. Also shown in the three graphs above is that the volumetric flow rate increases in a quadratic manner with voltage for all three orifice flow meters. Though in each case, the data had to be sorted and some points were omitted to obtain a sensible curve fit and the stated R^2 value. The calibrated orifice flow meters were used to perform the experiments.

The orifice meter could also be calibrated using literature equations to check the pressure drop it causes at a specific water velocity. However, this method (literature equations) involves trial and error analysis and therefore is assumed to be less accurate compared to practical calibrations. It could be interesting to compare the literature’s approximation to the practical orifice meter calibration, hence its recommended for future investigations. The literature equations that could be used to workout the flow rate across orifice meters are given as

$$\dot{V} = A_o C_d \sqrt{\frac{2(P_1 - P_2)}{\rho(1 - \beta^4)}}, \quad (\text{Cengel and Cimbala, 2006: 367})$$

Where $A_o = \frac{\pi d^2}{4}$ is the throat area and C_d is the discharge coefficient and is given by

$$C_d = 0.5959 + 0.0312\beta^{2.1} - 0.184\beta^8 + \frac{91.71\beta^{2.5}}{Re^{0.5}}, \quad (\text{Cengel and Cimbala, 2006: 367})$$

and $\beta = d/D$ is the ratio between diameters and $Re = \frac{\rho V D}{\mu}$ is the Reynolds number.

Thermocouples

The T-type thermocouple and the platinum resistance thermometer (PRT) were inserted into the data acquisition instrument and the multi-meter unit respectively.

The multi-meter was measuring resistance in Ohms from the PRT signals while the data acquisition unit was measuring temperature in degrees Celsius for T-type thermocouples.

The PRT resistances were converted into temperatures using the PRT certificate by Liedberg et al. (2003). The thermocouple measurements were compared to the PRT temperature measurements, as depicted in Table 3.7. The PRT temperatures were considered the most accurate and were used as the reference for the thermocouples.

Table 3.7: Thermocouples and platinum resistance thermometer measurements

PRT [Ω] Resistance	PRT [$^{\circ}\text{C}$] Measurement	T1 [$^{\circ}\text{C}$]	T2 [$^{\circ}\text{C}$]	T3 [$^{\circ}\text{C}$]	T4 [$^{\circ}\text{C}$]	T5 [$^{\circ}\text{C}$]	T6 [$^{\circ}\text{C}$]	T7 [$^{\circ}\text{C}$]	T8 [$^{\circ}\text{C}$]	T9 [$^{\circ}\text{C}$]	T10 [$^{\circ}\text{C}$]	T11 [$^{\circ}\text{C}$]	T12 [$^{\circ}\text{C}$]
107.8	20.00	20	20	20	20	20	20	20	20	19	19	19	19
115.5	40.00	40	40	40	40	39	39	39	39	39	39	39	39
119.4	50.00	50	50	50	50	49	49	49	49	49	49	49	49
123.1	59.90	59	60	59	59	59	59	59	59	59	59	59	59
127.0	69.94	69	70	69	69	69	69	69	69	69	69	69	69
130.8	79.94	79	80	79	79	79	79	79	79	79	79	79	78
134.6	89.86	89	89	89	89	89	89	88	89	88	88	88	88
138.3	99.85	99	99	99	99	98	99	98	99	98	98	98	98
142.1	109.84	109	109	109	109	108	109	108	109	108	108	108	108
145.9	119.75	119	119	119	119	118	119	118	119	118	118	118	118

The results from all the thermocouples were plotted in Figure 3.14 against the PRT results for convenience and analysed further. Note that, the temperature values were rounded off to the nearest unity to reduce the size of Table 3.7, so that it could fit within page margins. A conclusion drawn from the calibration results displayed in Figure 3.14 was that the thermocouple temperatures were close to accuracy, with only approximately $\frac{(119.75^{\circ}\text{C}-117.95^{\circ}\text{C})}{119.75^{\circ}\text{C}} \times 100\% = 1.5\%$ maximum uncertainties from the PRT readings at high temperatures, as shown in Figure 3.14. Hence, the calibrated T-type thermocouples were used to perform the experiments.

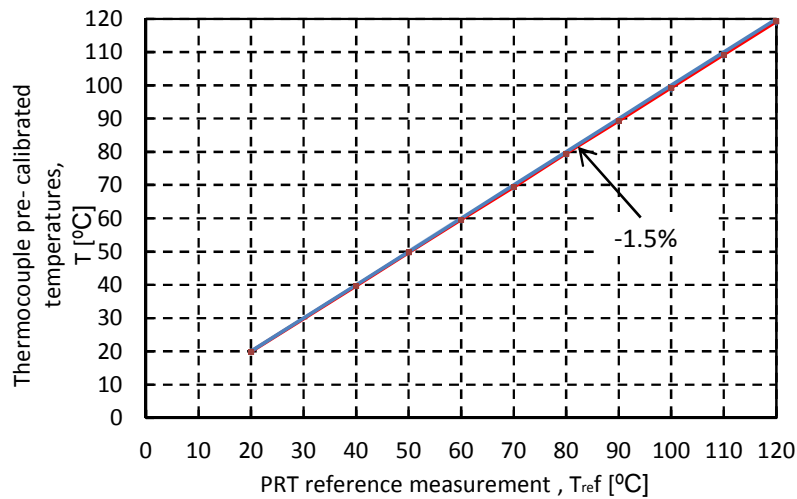


Figure 3.14: Thermocouple measurements vs. PRT reference temperatures

3.4 Experimental Procedure

Preparations and safety check

The experimental procedure started by filling the experimental set-up with water to the desired level in the steam drum (~100 mm) directly from the tap via the system's header. The system's header was then connected to the expansion tank open to the atmosphere to maintain the steam drum at constant pressure. The built-in pressure and visible air bubbles trapped in the system were released by opening the air release ball valve mounted on top of the steam drum. Air bubble dissipation was observed through the transparent channels and the steam drum's clear front and back views. The pressure gauge on top of the steam drum was also checked and monitored to ensure that it indicated atmospheric pressure. The valve on top of the steam drum was then closed and heat was injected at full power into the system through the three heating elements inserted into the risers. The condenser was supplied with tap water at a constant flow rate to stabilise the steam drum pressure and cool the system.

Dissolved air onset was again observed with the increase in fluid temperature to close to boiling. The system was allowed to boil and all the trapped air and built-in pressure were removed by opening the steam drum-mounted valve. The system was maintained at boiling for a few minutes until steady state was reached and air bubble formation was no longer observed. The heat was then switched off and the system was allowed to cool down for 4 (four) hours. This was done to ensure that the working fluid for the experimental tests was not contaminated by air. It was also to ensure that no air was trapped in the steam drum, creating an air-blanket between the condenser and the working fluid, blocking the cooling of the system.

The safety of the experimental set-up and operation was ensured by putting up safety notices alerting other laboratory users to the dangers of the set-up. All electrical appliances were visibly disconnected from the power supply after each test to minimise risks associated with fault currents. Another safety measure was to isolate the wet devices from the electrical equipment by housing the wet experimental system in a transparent protective frame.

Experiments

The experimental system was equipped with measuring instruments, as discussed in the apparatus section, and connected to an Agilent® data acquisition unit with 20 input channels per card (it had three cards). The data acquisition unit was coupled with thermocouples and differential pressure sensors. The unit could allow data acquisition at scanning intervals of 1ms. Temperatures were measured in the steam drum, header, top and bottom of the risers and down-comer, inlet and outlet of the condenser and room temperature.

The pressure drop was measured between the risers and down-comer at the header section using differential pressure sensors. The maximum temperature error measurement was $(119.75^{\circ}\text{C} - 117.95^{\circ}\text{C}) = 1.8^{\circ}\text{C}$ and pressure measurement uncertainty was $((1-0.9789)/1) \times 100\% = 2\%$. After completing the preparations and safety checks, the experiments were performed.

The experimental investigations were performed at three different power inputs, viz. 1kW, 2kW and 3kW per channel, to study the effect of power on the two-phase flow natural circulation response of the system and therefore investigate any unstable behaviour. The system was also operated with unequally heated channels to check and observe the behaviour of the system. The electrical heating elements were controlled independently using individual rheostats. At the same time, the heating elements' power was gradually and independently increased in steps of approximately 200W at a time. After the power rose to the desired value, the elements' power was maintained constant for nearly 30 min to ensure steady state was reached.

The natural circulation experimental investigation system was operated in three different modes, viz. open system, closed system and heat pipe mode. In the open system mode, the ball valve at the header was open so that the working fluid would expand to the expansion tank, therefore maintaining the system pressure at atmospheric pressure. For the closed system mode of operation, the expansion valve was closed and the steam drum pressure was maintained by the cooling system, the use of a safety valve and monitoring the pressure gauge to manually operate the air release valve if necessary. In the heat pipe mode of operation, the expansion valve was closed to maintain a constant volume, while the heating elements were switched off to suppress pressure increase and encourage boiling at low temperatures and pressures.

4 MATHEMATICAL MODEL

One of the objectives of this study was to develop and test a theoretical simulation program that predicted the experimental response of two-phase flow in a parallel multi-channel natural circulation loop. The following section provides a summary of equations derived from first principles (basic laws of fluid mechanics) and used to develop the computer code. A detailed derivation of the equations is provided in Appendix B.

4.1 Derivation of Equations

A one-dimensional (1-D) simulation program was developed from the equations of change derived from the fundamental principles of fluid mechanics and dynamics. The 1-D model predicts the temperatures and flow rates of a two-phase flow natural circulation in a three-parallel channel system subjected to constant (atmospheric) pressure operating conditions and different power inputs. The experimental loop was discretised into small control volumes, as shown in Figure 4.1. The theory was developed by applying the equations of change, i.e. conservation of mass, momentum and energy, to an arbitrary control volume to produce difference equations to be used in a computer code. The derivation of the 1-D mathematical model was based on the following assumptions:

- Flow in the loops is one-dimensional
- Fluid flow is incompressible and the two-phase flow is homogeneous
- The Boussinesq approximation is valid
- The sub-cooled boiling effect is negligible
- The thermodynamic equilibrium is applicable to both phases, i.e. particle velocity \ll speed of sound
- Heat flux input is constant as the system is electrically heated
- Heat losses from the system (transparent plastic piping) to the environment are negligible
- Hydrostatic pressure along the bottom of the loop is constant

The above assumptions were collected from various successful research resources (Nayak et al., 2006:652; Yun et al., 2008:666; White, 2011:26; Goudarzi & Talebi, 2013:116) and used to simplify the conservation equation. The reason behind considering each simplifying assumption is as follows: A one-dimensional method was used to model the experimental loop. This means that the working fluid properties varied in the axial direction of the flow tube only. Incompressible flow modelling means that there is no divergence in the fluid velocity, while homogeneous two-phase flow assumption implies that the liquid and vapour phases travel at the same velocity and the composition of water-vapour mixture is uniform and can be represented as a single fluid but with different properties.

Boussinesq approximation modelling assumes that the variation in inertia of the water-vapour mixture is negligible, but that the gravity is strong enough to differentiate the specific weights of the two fluids. Negligible sub-cooled boiling means the bubble formation during boiling would have insignificant impact on the flow rate. The thermodynamic equilibrium validity assumption implies that both phases would experience the same temperature instantaneously. Heat flux was assumed constant because heat addition into the system was done by electric heating rods. The effect of heat loss to the environment was assumed to be small such that it can be negligible, since polycarbonate material has fairly low thermal conductivity and most of the system parts were made from it. Pressure at the bottom of the loop (header) was assumed to be static, since natural circulation flows are usually low. Hence the header pressure was used as a pressure reference to simulate pressure at every point in the system.

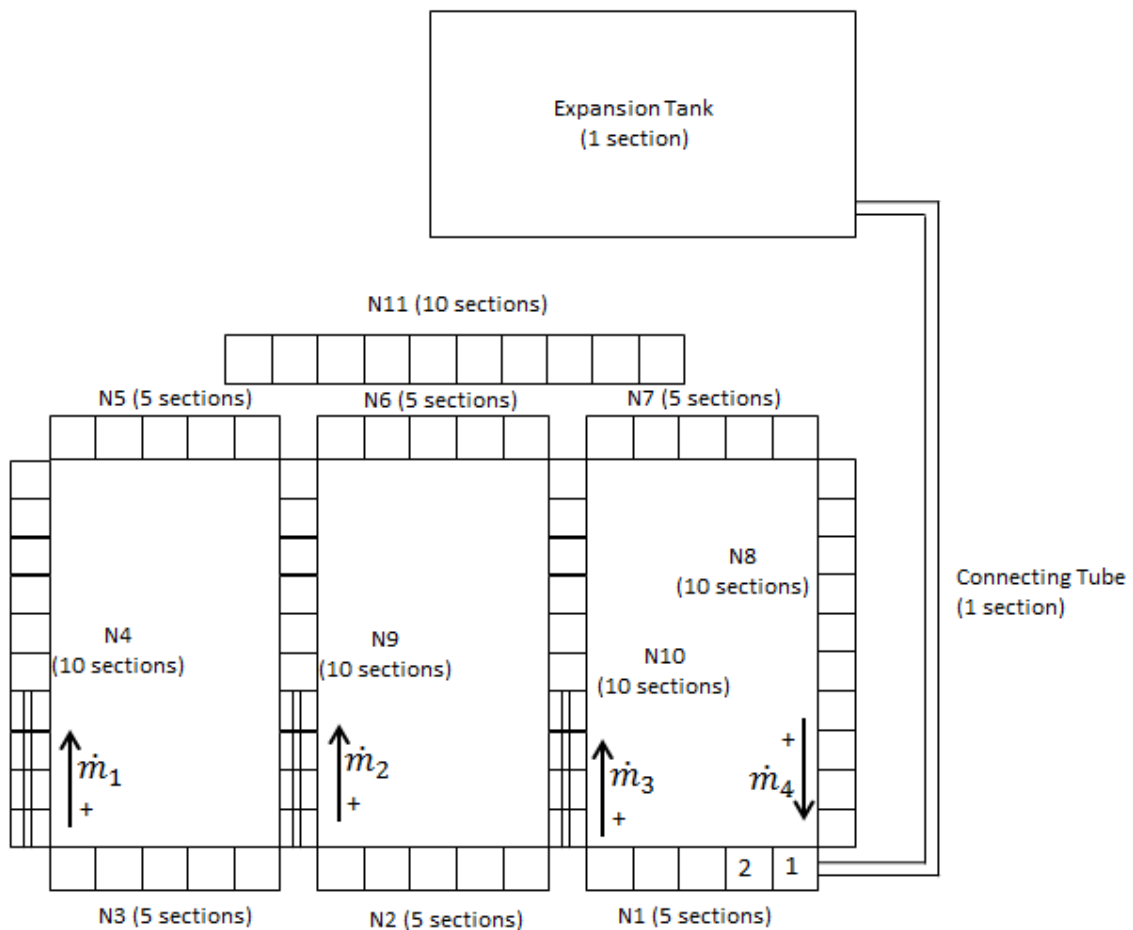


Figure 4.1: Discretized experimental model

These assumptions as explained above were used in conjunction with the fundamental principles in a form of the Reynolds transport theorem to shift from the system to the control volume formulation.

The conservation laws used were adapted from Cengel and Cimbala (2006:172, 201, 228) and are stated as follows:

Conservation of mass:
$$\frac{dm_{sys}}{dt} = 0 \quad (1)$$

Conservation of momentum:
$$\vec{F} = m\vec{a} = m\frac{d\vec{v}}{dt} = \frac{d(m\vec{v})}{dt} \quad (2)$$

Conservation of energy:
$$\dot{Q}_{net\ in} + \dot{W}_{net\ in} = \frac{d}{dt} \int_{sys} \rho e dV \quad (3)$$

The first equation states that the mass of a system undergoing a change remains constant. The second equation states that the rate of change of the momentum of a body is equal to the net force acting on the body. The third equation states that the energy content of a fixed quantity of mass can be changed by heat and work transfers. The three above equations were further expanded using the theory of Cengel and Cimbala (2006) and applied to fixed control volumes (Figure 4.2 a, b & c) by dividing the experimental system into smaller elements, as shown Figure 4.1 above.

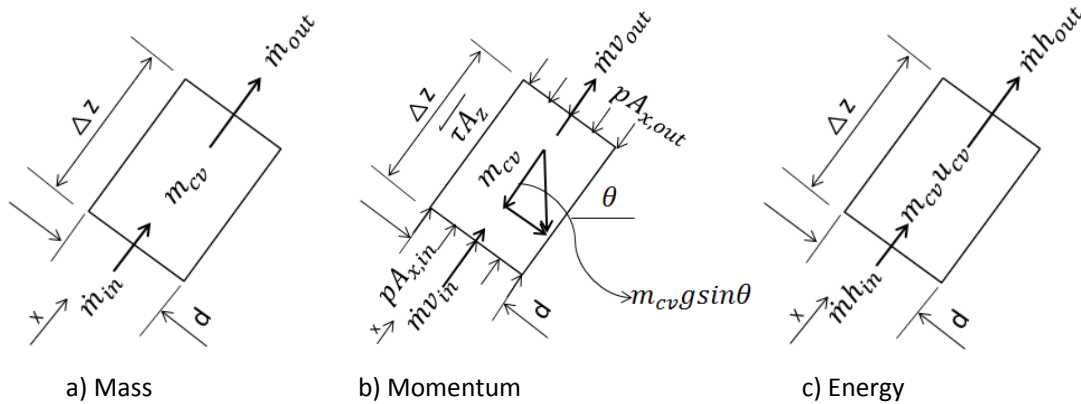


Figure 4.2: One-dimensional mass, momentum and energy control volumes

The derivation resulted in the following system mass flow rates and temperature equations:

By applying the conservation of momentum, as shown in Appendix B, the three mass flow rates in each riser may be represented by the following three equations:

$$S_1 \frac{\Delta(\dot{m}_1)}{\Delta t} - S_2 \frac{\Delta(\dot{m}_2)}{\Delta t} = -2F_1 \dot{m}_1 |\dot{m}_1| - gG_1 + M_1 \dot{m}_1^2 + 2F_2 \dot{m}_2 |\dot{m}_2| + gG_2 - M_2 \dot{m}_2^2 \quad (4)$$

$$S_2 \frac{\Delta(\dot{m}_2)}{\Delta t} - S_3 \frac{\Delta(\dot{m}_3)}{\Delta t} = -2F_2 \dot{m}_2 |\dot{m}_2| - gG_2 + M_2 \dot{m}_2^2 + 2F_3 \dot{m}_3 |\dot{m}_3| + gG_3 - M_3 \dot{m}_3^2 \quad (5)$$

$$(S_3 + S_4) \frac{\Delta(\dot{m}_3)}{\Delta t} + S_4 \frac{\Delta(\dot{m}_1)}{\Delta t} - S_4 \frac{\Delta(\dot{m}_2)}{\Delta t} = -2F_3 \dot{m}_3 |\dot{m}_3| - 2F_4 (\dot{m}_1 + \dot{m}_2 + \dot{m}_3) |\dot{m}_1 + \dot{m}_2 + \dot{m}_3| - gG_3 - gG_4 + M_3 \dot{m}_3^2 + M_4 (\dot{m}_1 + \dot{m}_2 + \dot{m}_3)^2 \quad (6)$$

where symbols S, G, F and M used in equations (4) to (5) are given by

$$\begin{aligned}
 S_n &= \sum_{i=b}^k \frac{L_i}{A_{x,i}} & P_n &= \sum_{i=b}^k \Delta p_i & F_n &= \sum_{i=b}^k \frac{L_i}{d_i} \frac{1}{\rho_i A_{x,i}^2} (C_{f,i} + K_{m,i}) \\
 G_n &= \sum_{i=b}^k \rho_i L_i \sin(\theta_i) & M_n &= \sum_{i=b}^k \frac{1}{A_{x,i}} \left(\frac{1}{\rho_{i-1} A_{x,i-1}} - \frac{1}{\rho_i A_{x,i}} \right)
 \end{aligned}$$

From the conservation of energy, the temperature is given explicitly, as derived and given as equation (B.44) in Appendix B as

$$\begin{aligned}
 T^{n+1} = T^n + \frac{\Delta t}{2\rho_i C_v L_i A_{x,i}} \left[\frac{V^2}{R} - h_{com,i} A_{z,i} (T_{s,i} - T_\infty) + \dot{m}^n C_p (T_{in} - T_{out}) - L_i A_{x,i} (2C_v T^n \frac{\Delta \rho}{\Delta t} \right. \\
 \left. + 2\rho_i T^n \frac{\Delta C_v}{\Delta t}) \right] \quad (7)
 \end{aligned}$$

The hydraulic and thermodynamic correlations such as friction factor, void fraction, friction multiplier heat transfer coefficient, etc. for calculating both single- and two-phase fluid properties to be used in equations (4) to (7) are given in Appendix B.4. The momentum equation was also applied to the discretised experimental system, assuming that steady flow conditions apply, to derive mass flow rate equations applicable to the steady-state condition (see Appendix C). However, the mass flow rate equations resulting from this assumption (steady state) were not used in the simulation program to test the system's performance. Equations (4) to (7) were used to develop the simulation program to calculate mass flow rates and temperatures for a single- and two-phase flow natural circulation system for each time step. Pressure losses, pressure, heat losses, densities, etc. were also calculated for each time step.

4.2 Simulation Computer Program

A computer code was developed, written and tested to predict the start-up transient and steady-state response of the natural circulation two-phase flow multichannel system. The computer code was developed from White's (2011) computer program, where he coded a dual loop parallel system. In this study, single and two-phase flow natural circulation in a triple parallel channel and one down-comer system was programmed. The program was able to predict the experimental behaviour (pressures, mass flow rates and temperatures) of the multichannel natural circulation loop, such that it could be evaluated against a specially designed and constructed transparent experimental loop.

The results of the simulation program were expected to possess reasonable comparison to the experimental outcomes. The following is a layout of the computer program's analysis.

- Define arrays to store up to 99 numbers corresponding to the control volume in an array
- Define system constants such as thermodynamic properties and material properties

$g = 9.81$: $PIE = 3.14159$: $C_{pg} = 2094$: $C_{vg} = 1564$ $C_{pl} = 4226$: $h_{fg} = 2441700$ '(@ 25degC, Cengel):
 $C_{vlv} = 4266$: $u_{fg} = 2304300$ '(@ 25degC, Cengel): $P_{crl} = 2.212E7$: $\rho_{wall} = 1200$: $C_{pw} = 1260$:
 $k_{wallpol} = 0.2$: $C_{pws} = 468$: $\rho_{wallss} = 8238$: $k_{wallss} = 13.4$

- Define liquid properties and condenser dimensions

$W_{cw} = 0.0363$: $C_{pcw} = 4180$: $C_{vcw} = 3718$: $ID_{cw} = 0.394$: $OD_{cw} = 0.025$: $OD_c = 0.028$: $AX_{cw} = 7 * PIE * (OD_{cw}^2) / 4$: $De_{qcw} = (ID_{cw} - 7 * OD_c) : L_{cw} = 0.333$: $AZID_{cw} = 7 * (L_{cw} * OD_{cw} * PIE)$:
 $AZOD_{cw} = 7 * (L_{cw} * OD_c * PIE)$: $T_{wall} = 0.0015$: $k_{wall} = 401$: $C_{pwall} = 385$: $\rho_{wallcop} = 8933$

- Define system geometric grid dimensions
- Define initial conditions such as initial temperature, time step, atmospheric pressure, etc.

$V_{supply} = 230$: $DTIME = .05$: $time = 0$: $TSTEP = 0$: $Tbegin = 21.0$: $T_{cwi} = 20$: $T_a = 23.7$: $T_{tankbeg} = 21$: $Patm = 100700$: $Rhot = 17.63$

- Define friction factors, environmental heat loss factor, heat exchanger cooling factor, run time and power factor

$xf = 1$ 'friction
 $xl = 1$ 'environmental losses
 $xc = 1$ 'cooling
 $tm = 80$ 'run time in minutes
 $xp = 1$ 'power factor

- Define the geometric dimensions of the expansion tank

$L_{tank} = .694$: $B_{tank} = .394$: $Z_{tank} = .2$: $P_{tank} = 2 * (L_{tank} + B_{tank})$: $L_{pipe} = 3.3$: $D_{pipe} = .025$:
 $Z_{pipe} = 3.015$: $VOL_g = 0$: $T_{tank} = T_{tankbeg}$: $M_{tank} = fnRltemp(T_{tank}) * (L_{tank} * B_{tank} * Z_{tank} + PIE * (D_{pipe}^2 / 4) * L_{pipe})$

- Determine first cell hydrostatic pressure from expansion tank open to the atmosphere
 $P_1 = Patm + fnRltemp(T_{tank}) * g * (Z_{pipe} + Z_{tank})$
- Calculate a cell's geometric properties around the main loop
- Calculate minor losses in pressure for each cell located at tees, bends, contraction and expansions
- Determine the initial cell interface pressures
- Determine the initial average pressure and initial saturation temperature

```

FOR k = 1 TO (N - N11)
PB(k) = ((P(k) + P(k + 1)) / 2)
Tsats(k) = fnTsatsP(abs(PB(k)))
NEXT k
FOR k = (N - N11 + 1) to N
PB(k) = Patm + fnRltemp(T)*g*Zpipe
NEXT k

```

- Assign initial temperatures and quality values to each cell in the main loop. This assumes that there is liquid only and no air and vapour in the system initially.

```

FOR k = 0 TO (N - N11): T(k) = Tbegin: Twall(k) = Tbegin: X(k) = 0: NEXT k

```

- Calculate densities and mass flow rates of each cell

```

FOR k = 1 TO (N - N11)
Rg = fnRg(k): Rl = fnRl(k)
ALPHA(k) = fnALPHA(X(k))
R(k) = fnR(X(k), Rg, Rl)
M(k) = VOL(k) * R(k)
NEXT k

```

- Calculate the cooling water cell temperatures and masses

```

FOR k = (N - N11 + 1) to (N)
T(k) = Tcwi: Mcw(k) = fnRcw(k) * AXcw * L(k)
NEXT k

```

- Calculate the net heat flows for each cell: the program performs an energy balance for each cell for each time step
- Assign zero index values to each of the defined arrays: this assures continuity from the beginning to the end points in the loop
- Give a warning to close the output text file
kill "LUCY_Test11.txt"
- Open the output text file and write the heading titles, program specifications, etc.
Open "LUCY_Test11.txt" for append as #1
- Close the output file
close #1

START THE MAIN LOOP: Program returns to this point after each time step's calculation

```

Initialise all four mass flow rates to zero
W1 = 0: W2 = 0: W3 = 0: W4 = Ws = 0

```

Run the simulation until the specified run time is reached and then exit the loop and end the program.

[mainLoop]

IF time > (tm*60.0) THEN

GOTO [exitLoop]

END IF

Calculate each cell's new net heat flows for looping purposes

$Q_{cw5b} = 0$: $Q_{cw6} = 0$: $Q_{cw7a} = 0$

if TSTEP mod 2000 = 0 then

print ""

end if

Assign mass flows to an array for passing to functions

Assign outer heat transfer coefficients to an array

Determine enthalpies per cell

Determine heat lost to the wall to heat it up

for k = 1 to (N1 + N2 + N3 + N4a + N4b)

$Tw_{new}(k) = fnTw(k)$

$Q_w(k) = M_w(k) * C_{pw} * (Tw_{new}(k) - Tw_{all}(k))$

next k

for k = (N1 + N2 + N3 + N4a + N4b + 1) to (N1 + N2 + N3 + N4a + N4b + N5a + N5b + N6 + N7a + N7b)

$Tw_{new}(k) = fnTw(k)$

$Q_w(k) = M_w(k) * C_{pwss} * (Tw_{new}(k) - Tw_{all}(k))$

next k

for k = (N1 + N2 + N3 + N4a + N4b + N5a + N5b + N6 + N7a + N7b + 1) to (N - N11)

$Tw_{new}(k) = fnTw(k)$

$Q_w(k) = M_w(k) * C_{pw} * (Tw_{new}(k) - Tw_{all}(k))$

next k

Determine new cell temperatures and qualities

Calculate new densities for main cells

FOR k = 1 TO (N - N11)

$R_g = fnR_g(k)$: $R_l = fnR_l(k)$

$R_{new}(k) = fnR(X_{new}(k), R_g, R_l)$

$M_{new}(k) = VOL(k) * R_{new}(k)$

$ALPHA_{new}(k) = fnALPHA(X_{new}(k))$

NEXT k

Calculate new densities at the nodes

Calculate the internal energies from an energy balance and determine the new control volume qualities and temperatures

Determine the condenser's new inlet and outlet temperatures

Calculate new densities of the working fluid in the system

Determine new average expansion tank temperature

Determine new mass flow rates

Calculate the flow regime and governing friction model by

$$Re_D = \frac{4\dot{m}}{\pi\mu D}$$

if $Re < 2000$ then the flow is laminar and the friction factor is $f = \frac{64}{Re}$ or

if $Re > 2000$ then the flow is turbulence and the friction factor on smooth walls is

$$f = \left[-1.8 \log \left(\frac{6.9}{Re_D} \right)^{-2} \right]$$

Calculate applicable constants for the differential equations for equations (4) to (7) of

section 4.1 nodes analysis performed on the basis of flow rates from previous time step

Calculate the full step equations similar to equations (4) to (7) in section 4.1 and calculate

mass flow rates in each leg, using the full momentum equation as given by

$$\sum_{i=b}^k \frac{L_i}{A_{x,i}} \frac{\Delta \dot{m}_n}{\Delta t} = - \sum_{i=b}^k \Delta p_i - 2 \sum_{i=b}^k \frac{L_i}{d_i} \frac{\dot{m}_n |\dot{m}_n|}{\rho_i A_{x,i}^2} (C_{f,i} + K_{m,i}) - g \sum_{i=b}^k \rho_i L_i \sin(\theta_i) + \sum_{i=b}^k \frac{\dot{m}_n^2}{A_{x,i}} \left(\frac{1}{\rho_{i-1} A_{x,i-1}} - \frac{1}{\rho_i A_{x,i}} \right)$$

Calculate new pressures at cell interfaces

Calculate new total pressures by determining friction, momentum and buoyancy pressures per cell

Based on the total cell pressures, calculate saturation temperatures at each cell

Calculate volumetric flow rates per leg by converting mass flow rates of each leg

Replace the old array values with the corresponding new system property arrays, to

prepare for the new cycle

Print the key parameters to the output text file, including run times, mass flow rates, temperatures, etc.

Repeat all the steps in the main loop until total run time is reached

End the main loop

Define all functions to be called by the main program to perform calculations, such as

function fnRltemp(T)

fnRltemp = (ar1 + ar2 * (T + 273.15) + ar3 * (T + 273.15)² + ar4 * (T + 273.15)⁶ + 1e-3)⁻¹

end function

4.3 Debugging Phase

After correcting all errors and bugs, the program started running and executed results on the output text file. The outputs contained temperatures, mass and volumetric flow rates as a function of time. The results sample generated by the program powered at 1kW per riser, are included in Appendix E. The results were graphically represented, further analysed and compared to the experimental outcomes in the following section.

5 RESULTS AND DISCUSSION

Experimental and theoretical results were performed at different power excitations and various operation modes to study the behaviour of a two-phase natural circulation in a multi-parallel channel system. The system was excited at 3kW, 6kW and 9kW on various occasions. The three heating legs were subjected to equal power inputs simultaneously by independent electrical heating elements. The following sections describe the general observations from the experimental investigation. The results, a discussion and conclusions drawn from both the experimental and simulation studies are also outlined in the following sections.

5.1 Experimental Observations

Experiments started by switching on the power, which triggered the development of natural circulation single-phase flow. The single-phase natural circulation was measured by the differential pressure sensors and could be observed through the transparent tubes. Single-phase flow natural circulation was observed as wave-front fluid with no air bubbles flowing along the loops (three risers connected to a common down-comer). The flow was evident, accelerating upwards through the risers after few minutes of power injection. Two-phase flow was established at a channel power greater than 800W. The increase in power and temperature of the working fluid resulted in the onset of air bubbles and increased pressure. The system was observed expanding and breathing through the expansion tank in the open system operating mode. The remaining air and built-in pressure were evacuated by opening the valve mounted on top of the steam drum, and this was also applicable to the closed system and heat pipe operation mode.

The two-phase flow open system operation mode went through three different flow regimes, viz. bubbly, slug and churn flow patterns. The interpretation of the flow patterns was adapted from Mills (1999:703). Only the bubbly flow regime was evident in the closed and heat pipe system operation modes. The power was maintained at the desired level in all three risers (heating elements) for at least 30 minutes for the system to reach steady state. Before the steady state was reached, a repeated sudden release series of voids pursued by a single-phase liquid was witnessed. During this phase the flow was oscillating widely and even reversed several times. Dissolved air trapped in the system was observed as bubbles accelerating into the steam drum. The ventilation system mounted on top of the steam drum was operated repeatedly until there was no more visible air bubble formation.

5.2 Experimental Results

The experimental system was operated as an open system, closed system and in heat pipe mode. Temperatures and differential pressures (DPs) were measured at various locations, as shown in Figure 5.1. The results obtained from all three modes of operation are documented and interpreted in the next sections.

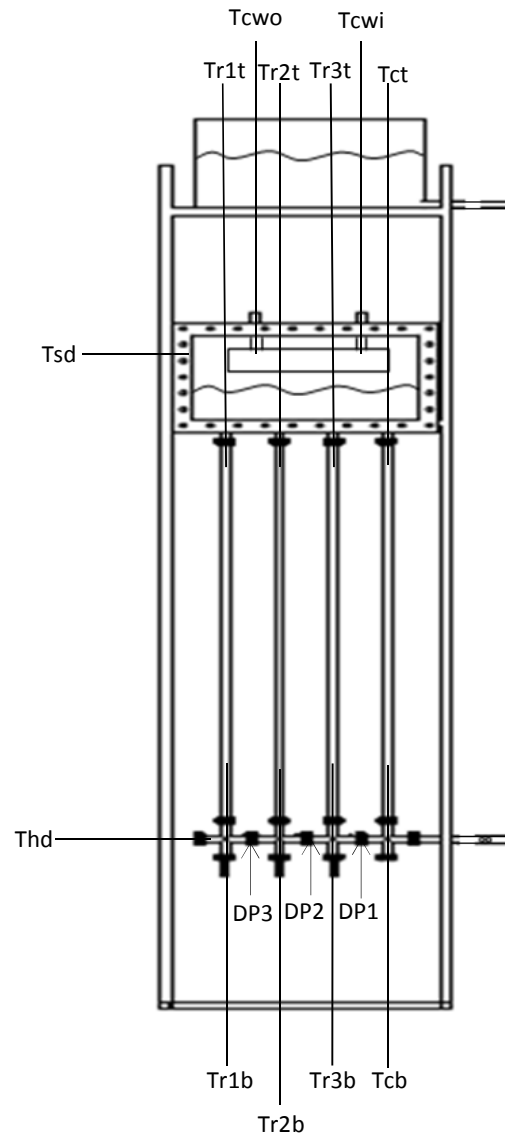


Figure 5.1: Experimental temperatures and pressure drops measuring locations

- Tr1t - top temperature of the left riser
- Tr1b - bottom temperature of the left riser
- Tr2t - top temperature of the middle riser
- Tr2b - bottom temperature of the middle riser

- Tr3t - top temperature of the right riser
- Tr3b - bottom temperature of the right riser
- Tct - top temperature of the down-comer
- Tcb - bottom temperature of the down-comer
- Tcwo - outlet temperature of the cooling water
- Tcwi - inlet temperature of the cooling water
- Thd - Temperature at the header
- Tam - ambient temperature
- Tsd - steam drum surface temperature

Temperatures were measured at the top and bottom of the risers and common down-comer using T-type thermocouples, as explained in the instrument section in 3.2. The condenser outlet and inlet water temperatures were also measured in degrees Celsius. Pressure drops were measured across the three orifice plates using differential pressure sensors. The differential pressure sensor output was in DC Volts, which was converted into mass flow rates using the orifice calibration curves equations (see the calibration results in section 3.3.3).

5.2.1 Open expansion valve operating mode

In this mode the system was connected to the expansion tank open to the atmosphere. The condenser was connected to a cold water tap kept at a constant rate for the entire duration of the test. The water tap was initial fully open to evacuate air, if any, trapped in the condenser and to clear air bubbles. The condenser cooling water flow rate was then adjusted to the required flow rate (0.032kg/s) and maintained for the entire duration of the experiment and for all three different power input tests (3kW, 6kW and 9kW). The water outlet of the condenser was connected to a drain via a transparent plastic pipe. The mass flow rate of the cooling fluid was regularly checked by collecting the outlet water with a bucket while measuring time with a stop watch. The collected water was then weighed on a scale in kilograms and converted to kilograms per second.

Experiments were performed over weekends when nobody was performing water activities that might cause disturbance in the cooling water flow rate while the experiment setup was in operation. The experimental open system operating mode results for the two-phase flow natural circulation in a multi-parallel channel system are presented below for the different power inputs.

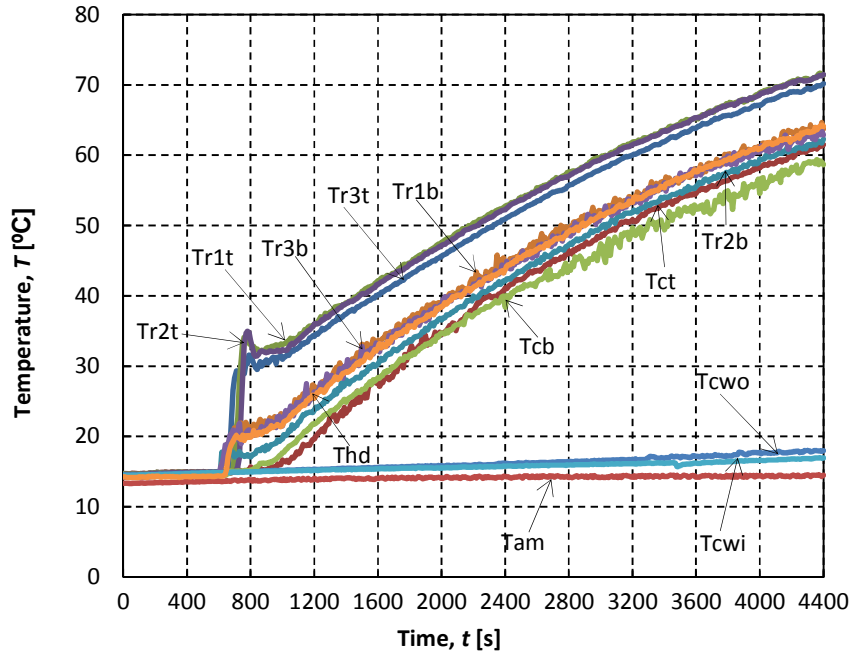


Figure 5.2: Temperature as a function of time of a 3kW (1kW per riser) test open system

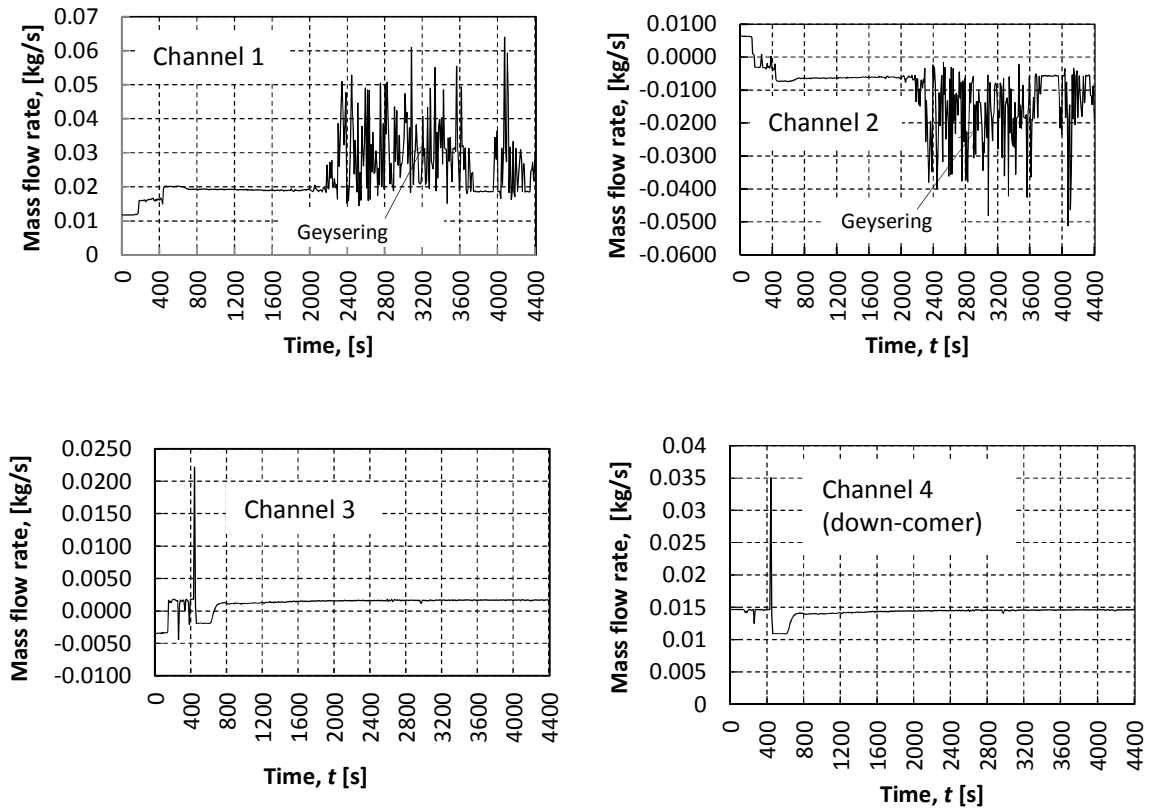


Figure 5.3: Mass flow rate as a function of time in channels 1, 2, 3 & 4 of a 3kW test open system

At low power conditions (3kW) with the system open to the atmosphere, the temperatures took longer to reach temperature stability (see Figure 5.2), because of low power inputs into the system. Therefore, it was assumed that there would be no major flow behaviour changes even after the temperature has reached stability. The system exhibited a transient response characteristic during the start-up, i.e. for approximately the first 800 seconds, as shown in Figure 5.3 (channels 1, 2, 3 and 4). In this phase, temperatures in the three risers increased sharply until the density gradient between the heated channels and the cold channel (down-comer) was established to overcome friction and the fluid started flowing. After overcoming friction, temperatures dropped due to cold fluid mixing with hot fluid. The temperatures then rose smoothly in all channels and fluid started flowing efficiently in all channels, exhibiting single-phase loop features.

The commencement of the two-phase flow features was witnessed after approximately 2 000 seconds when temperatures started rising rather rapidly and the mass flow rates in channels 1 and 2 began to be chaotic. According to Figure 5.3 (channels 1 and 2), most of the fluid in channel 1 was flowing into channel 2, causing channel 2 to flow in the reverse direction (downward). Approximately all the fluid from channel 2 was recirculating to channel 1. Hence, channel 2's mass flow rate showed the same behaviour as that of channel 1, but in a reverse direction. Figure 5.3 (channel 3) shows that, after the transient response, the fluid in channel 3 was flowing upward (positive direction) all the time and coming back through the cold channel (down-comer). However, the mass flow rate in channel 3 clearly was stable but small in magnitude compared to the other channels. It can further be witnessed in Figure 5.3 (channels 1, 2, 3 and 4) that a small percentage of the fluid from channel 1 was coming back through the down-comer as well.

Figures 5.3 (channels 1 and 2) shows a sudden increase in mass flow rate associated with high-amplitude oscillations due to a continuous increase in power. At this point, the loop was believed to be operating in two-phase fluid, hence the buoyancy force increased as a result of steam void formation in the risers. Figure 5.2 shows that the system was operating with low-quality steam, as temperatures stabilised just below 80°C and rose no further. For this reason, the system was experiencing Type I instability, where the low power triggered oscillatory flow conditions in low-quality fluid.

According to Figure 5.3, there was very little if any of the fluid from channel 2 was flowing into the down-comer. Hence, channels 3 and 4 showed similar conduct. This is also evident from the temperature graph in Figure 5.2, where channel 3's top temperature (Tr3t) remained lower than the top temperatures of channels 1 (Tr1t) and 2 (Tr2t), irrespective of their equal heating. The inlet temperature of the condenser remained constant while the outlet temperature was gradually rising, indicating heat removal from the system.

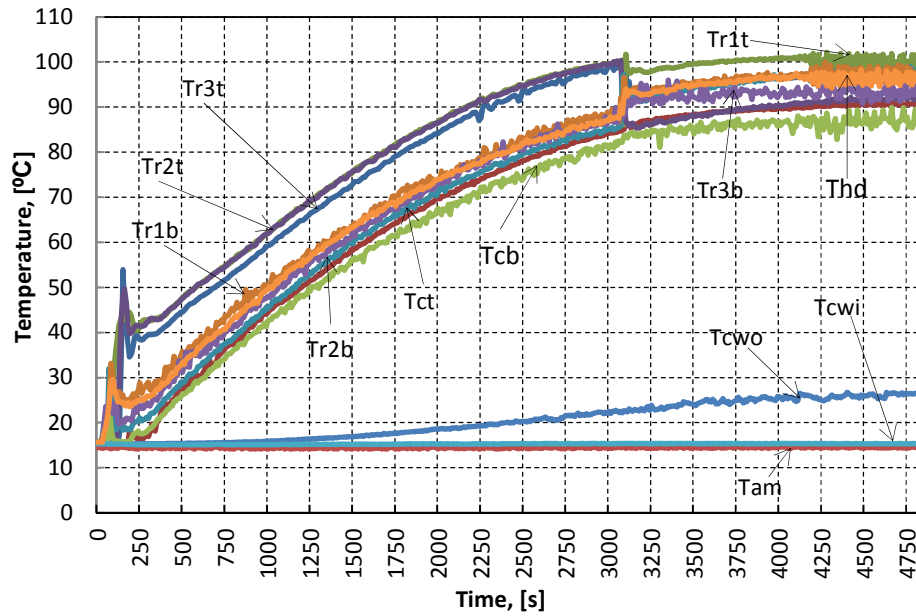


Figure 5.4: Temperature as a function of time of 6kW (2kW per riser) open system

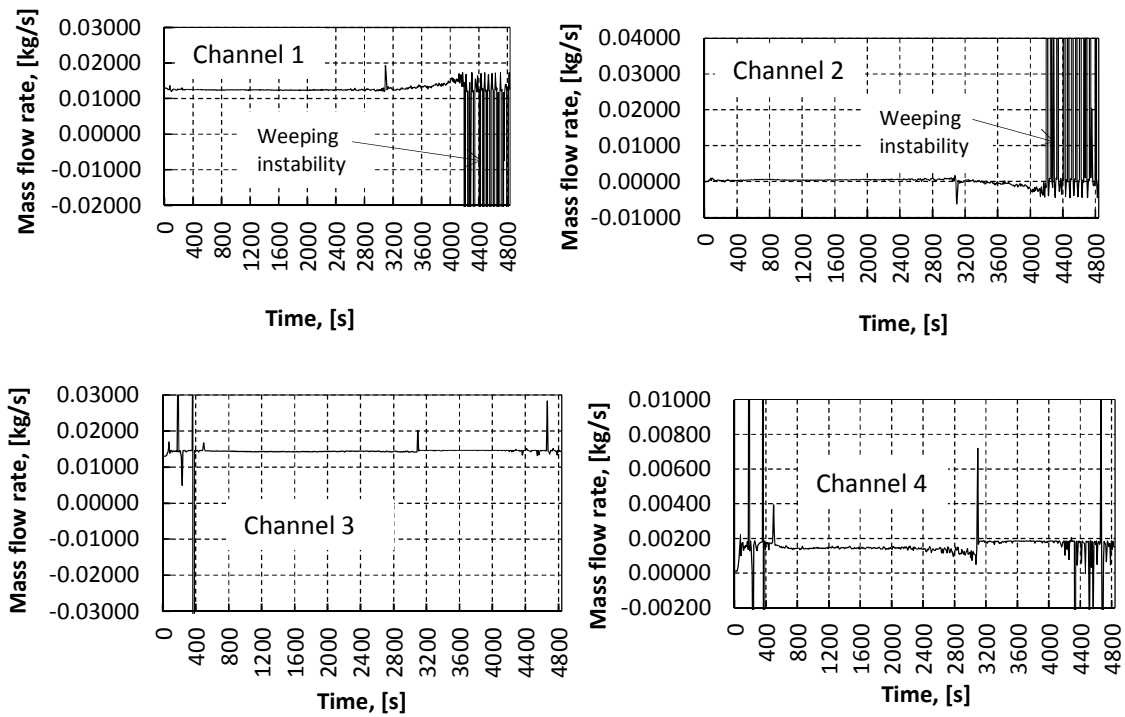


Figure 5.5: Mass flow rate as a function of time in channels 1, 2, 3 & 4 of a 6kW open system

Under medium power conditions (6kW), the system's transient start-up response was experienced during the first 400 seconds (see Figure 5.4 and Figure 5.5, channels 1, 2, 3 and 4). After friction was overcome, temperatures underwent a stable increase until boiling was reached at 100°C. Figure 5.4 shows that the risers' top temperatures reached steady-state condition after 3 000 seconds. The top temperatures of channels 2 and 3 dropped to below 100°C and stabilised there, while top temperature of riser 1 maintained a stable condition just above 100°C. The inlet temperature of the cooling water in the condenser remained constant at 16°C, while the outlet temperature rose rapidly after 1 250 seconds and stabilised just above 25°C during the steady boiling phase (approximately after 4 000 seconds).

It is observed from Figure 5.5 (channels 1, 2, 3 and 4) that all the channels initially demonstrated the same performance, although the rise in power introduced the commencement of flow oscillations. Figure 5.5 (channels 1, 2, 3 and 4) show that there was a sudden increase in flow at 3 000 seconds due to the increasing temperature. However, the system achieved stable flow, after which it decreased slightly in some channels (Figure 5.5, channels 1 and 2), resulting in weeping oscillations (repeated oscillations with higher amplitudes) in channels 1 and 2 as the temperature continued to increase. Under this condition, a buoyancy-dominated instability with regard to power increase was witnessed. Also noted was the interaction among channels. It is clear from Figure 5.5 (channels 1, 2, 3 and 4) that the mass flow rates of channels 1 and 2 were out of phase, while the flow rates of channels 3 and 4 were in phase.

Also shown in Figure 5.5 (channels 1, 2, 3 and 4) is that the total mass flow rate from all three risers initially was coming down through the down-comer, although this was interrupted by a sudden overpass due to the commencement of bubbly boiling resulting from the continuous increase addition of heat to the system. After steady boiling was reached, the mass flow rate in channel 2 started becoming violent and chaotic, with most of its fluid flowing into channel 1 and part of it into riser 3 and the down-comer(channel 4), causing both channels 1 and 3 to flow in the reverse direction.

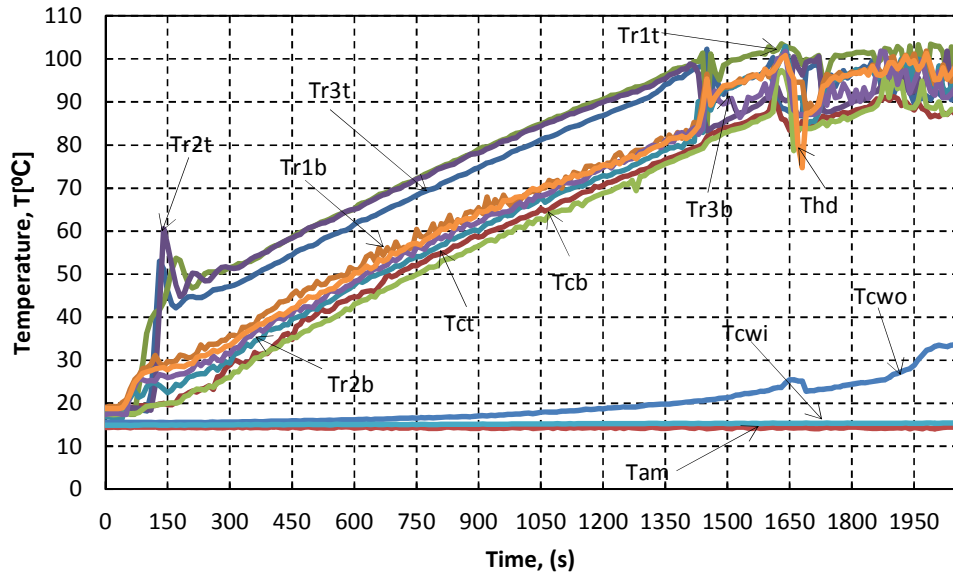


Figure 5.6: Temperature as a function of time of a 9kW (3kW per riser) test open system

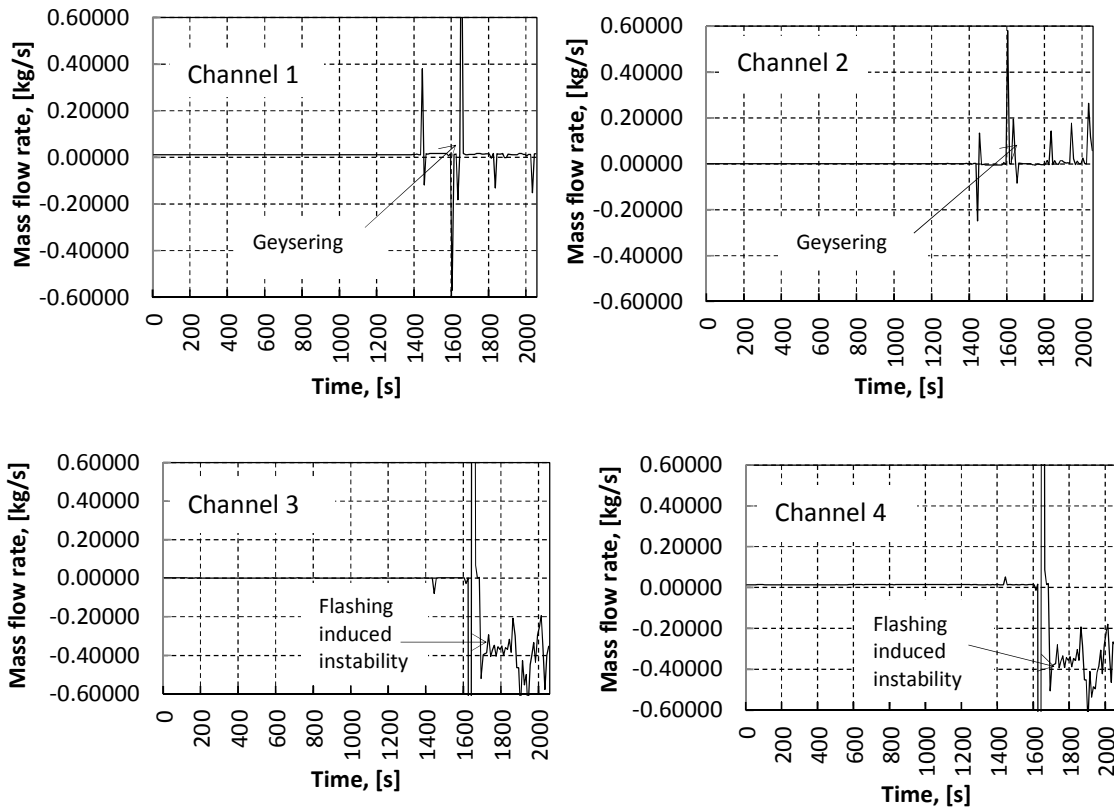


Figure 5.7: Mass flow rate as a function of time in channels 1, 2, 3 & 4 of a 9kW open system

Under high power conditions (9kW), the system's transient start-up response phase persisted no longer than 200 seconds, as is evident in Figure 5.6. After friction was phased out (buoyancy force overcoming gravitational force and material's resistivity), temperatures continued to rise effortlessly to 100°C, where bubbly boiling commenced. During the rising mode of temperatures in the system (the first 1 400 seconds), the mass flow rates in all three risers were flowing in the positive direction, i.e. upward and coming down as a sum through the down-comer. Overshooting of a two-phase mass flow rate at the steady bubbly boiling condition was evident past 1 400 seconds (see Figure 5.7, channels 1, 2, 3 and 4). The mass flow rates in both channels 1 and 2 seemed to stabilise with occasional overshoots, whereas channel 3 was flowing in the reverse direction, causing the down-comer to flow in the opposite direction (upward) after 1 600 seconds.

Figure 5.7 shows that channels 1 and 2 were intermingling, while riser 3 and the down-comer possessed in-phase behaviour. It can be observed in Figure 5.7 that the continuous increase in energy input introduced flow oscillations in all the channels. It is evident from Figure 5.6 that, during the oscillatory region the two-phase fluid was dominated with high quality since boiling is trending above 100°C. It can be seen from Figure 5.7 (channels 1 and 2) that a further increase in temperature resulted in the reduction of the amplitude of the oscillations. However, in channels 3 and 4, a continuous increase of power in the system resulted in flow reversal with reduced amplitude of the oscillations.

In this case, the flow behaviour shifted from the buoyancy-dominated region to the friction-dominated phase. Under these operating conditions, the system encountered Type II instability, where high power gave rise to flow oscillations due to high friction (boiling). Flashing instability in channels 3 and 4 was also observed as bottom riser temperatures approached top riser temperatures (header temperatures approached steam drum temperatures). These kinds of instabilities were also observed by Jain et al. (2010) and Jiang et al. (1995) in their investigations of two-phase flow natural circulation systems.

5.2.2 Closed expansion valve system mode

After each open system test had reach steady-state conditions, the valve connecting the expansion tank to the system's header was closed and the power was switched off for a few minutes. This was done to settle down the system before operating it as a closed system. After the system had settled down, power was turned-on to the desired level to study the behaviour of a two-phase flow multi-parallel channel system. In this operation mode, the cooling water was maintained constant as in the operation mode for the open system. The system was powered at different inputs (3kW, 6kW and 9kW) to study the effect of various heat inputs on the system under investigation. The water level was maintained at the same level (100 mm high in the steam drum) for all operation modes. Release of built-in pressure did not have a significant impact on the level of water in the system. A mark was made on the steam drum at 100 mm to ensure that the same level of water was maintained for all tests. The level of water was observed through the clear front and back parts of the steam drum.

For closed system operation the program was pre-set to the workout system's pressure using Bernoulli's equation, $P = P_{steam\ drum} + \rho gh$ with reference to the liquid pressure in the steam drum at saturation temperature. In this case the system's pressure was changing, with temperature and volume assumed to be constant, as breathing through the expansion tank was terminated by closing the valve. The volumetric expansion of the system as a result of pressure built in during operation was assumed to be small enough to be ignored. Figure 5.8 shows a simple version of a two-phase natural circulation system operated at constant volume (closed system).

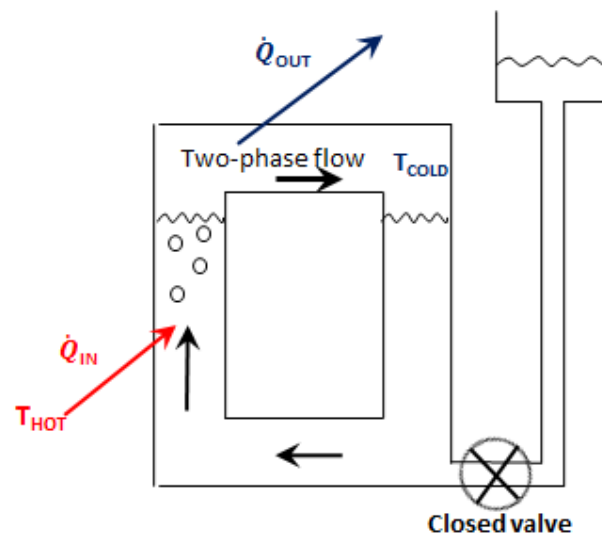


Figure 5.8: Two-phase natural circulation constant volume loop

This system operation (closed loop) possesses heat pipe features where the system is subjected to vacuum pressure, causing boiling to be achieved at low temperatures. The cooling system was active for the duration of this test to stabilise the pressure in the steam drum and prevent volumetric expansion. Temperature and mass flow rate data obtained during each time step under different power inputs are plotted and analysed in the following graphs.

Built-in pressure was monitored through the pressure gauge and released through the ventilation system mounted on top of the steam drum whenever the need arose. Air bubble formation was not observed in this operation mode, and the system appeared to be less violent, even at higher temperatures.

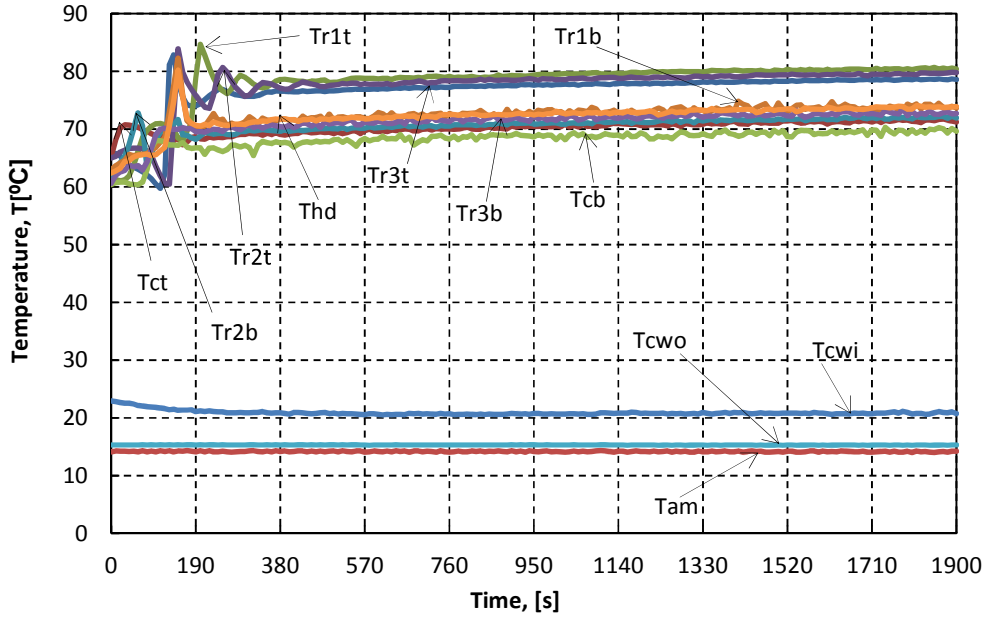


Figure 5.9: Temperature as a function of time of 3kW test closed system

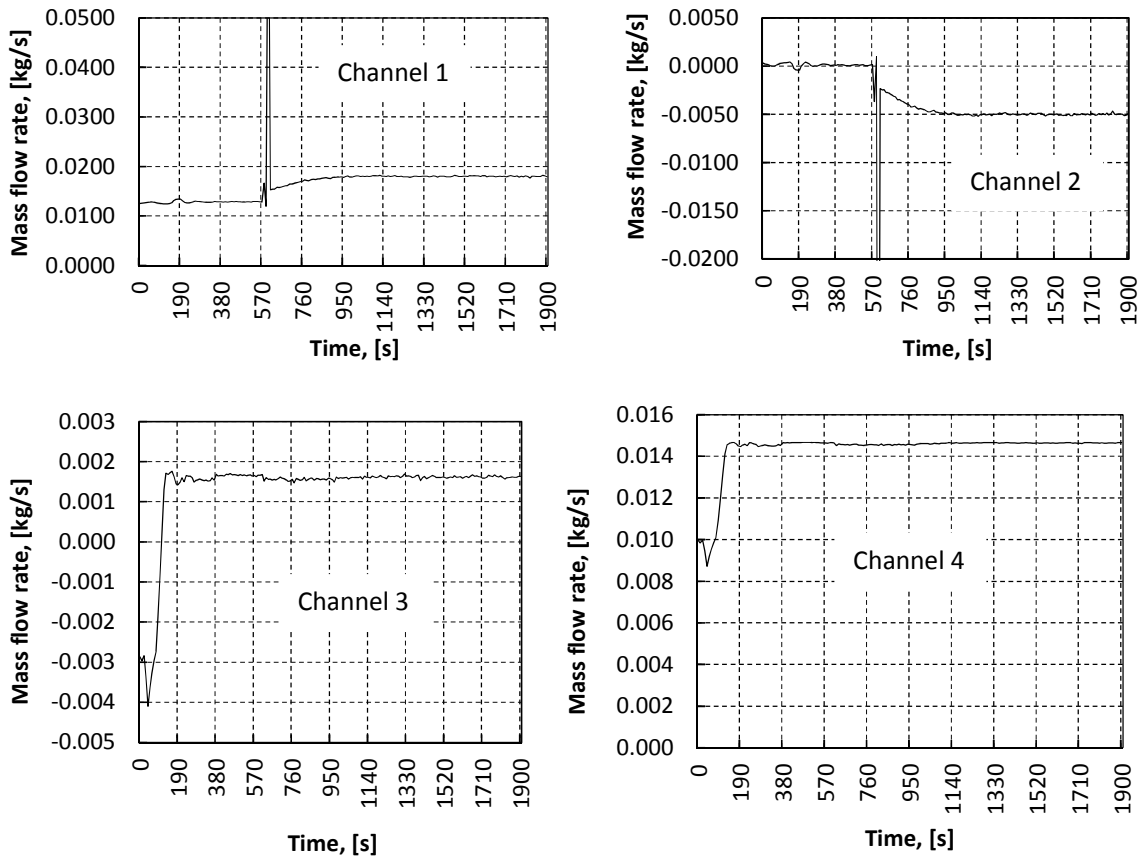


Figure 5.10: Mass flow rate as a function of time in channels 1, 2, 3 & 4 of a 3kW closed system

With the system closed (not open to the atmosphere), the system experienced a start-up transient response during the first 190 seconds at low power operating conditions (3kW). After overcoming friction the temperatures rose rather rapidly and reached the steady-state condition at approximately 1 140 seconds, with the highest temperature of just above 80°C (see Figure 5.9). The mass flow rate graphs (Figure 5.10, channels 1, 2, 3 and 4) show that the flow was smooth after overcoming friction, with channel 2 flowing in the reverse direction at a low flow rate out of phase with channel 1. According to Figure 5.10, the mass flow rate in channel 1 was split into two in the steam drum, part of it flowing through channel 2 and the rest flowing through the down-comer. The mass flow rate of channel 3 remained fairly low, but in the forward direction. Also shown in Figure 5.10 (channels 3 and 4) is the similar pattern between channel 3's mass flow rate and the down-comer.

The onset of two-phase flow is observed in Figure 5.10 (channels 1 and 2), after the sudden increase in mass flow rate at 570 seconds due to the continuous increase in temperature and steam void formation. Such conduct is classified as Type I instability. It was further noted that operating the system as a closed system reduced the vibrations and chaotic behaviour of the system at low power operation conditions. It was further noted that the mass flow rate did not necessarily increase or decrease as a result of isolating the system from the atmosphere, but rather stabilised the system with no overshoots.

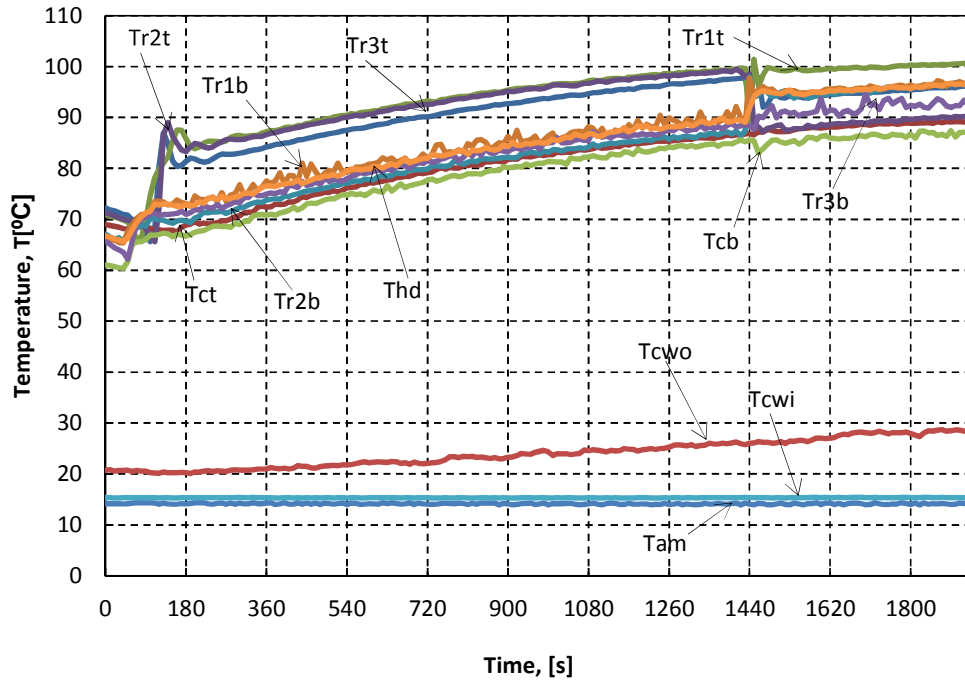


Figure 5.11: Temperature as a function of time of a 6kW test closed system

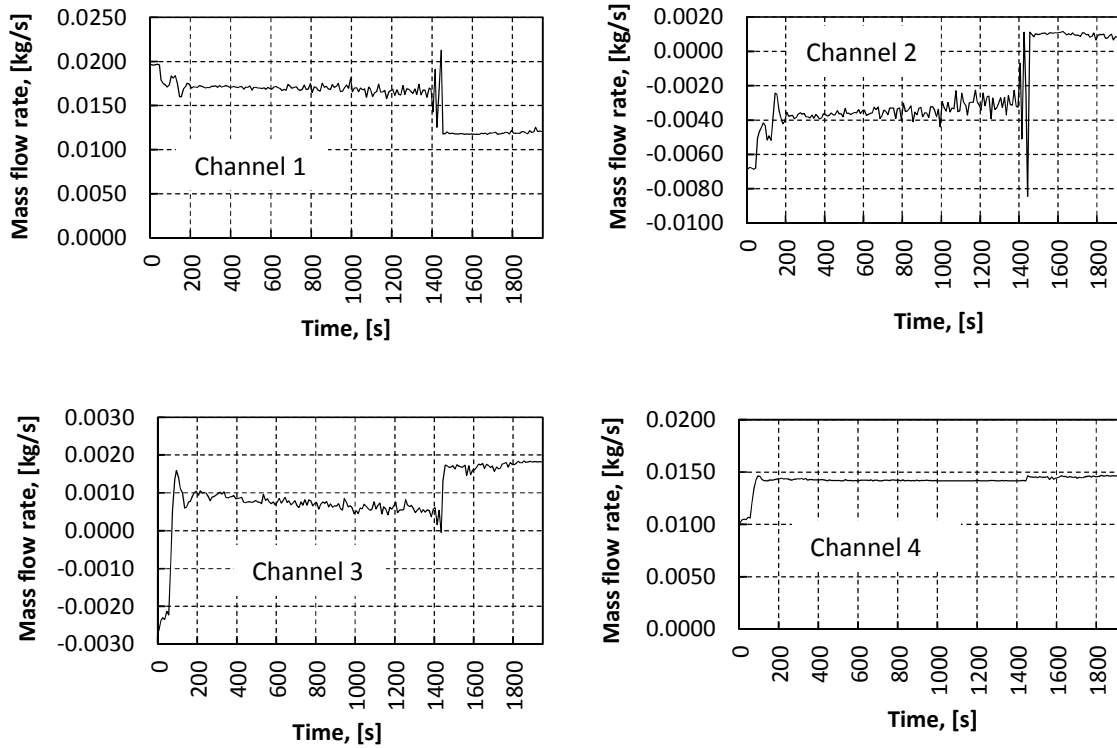


Figure 5.12: Mass flow rate as a function of time in channels 1, 2, 3 & 4 of a 6kW closed system

Under medium power operating conditions (6kW) with the valve closed, the start-up transient response did not last longer than 200 seconds, after which the system started operating smoothly with temperatures rising fast and the mass flow rate maintaining stable movement in all the channels. Figures 5.11 and 5.12 show that there was an overshoot at approximately 1 440 seconds before the temperatures reach the steady-state condition. The mass flow rate pattern was also affected by this overshoot, which caused channel 2 to flow in the positive direction and channel 1 to slow down but still flow in the positive direction.

The sudden increase in flow rates in channels 2, 3 and 4 was as a result of an additional buoyancy force from the formation of steam voids with an increase in power. It can be seen in Figure 5.12 (channels 2, 3 and 4) that the mass flow rates in these channels become more stable with damped oscillations after the transition from low to high flow. However, channel 1 experienced a sudden reduction in flow rates with a continuous rise in power. This channel (channel 1) was going through a friction-dominated zone, which led to a more stable regime with reduced oscillations (see Figure 5.12, channel 1). This behaviour is certainly categorised as Type II instability. It is interesting to note that the channels were experiencing various instabilities with the continuous heat addition.

It is evident from the graphs that channel 2 was initially flowing in the reverse direction until the temperature reached 100°C and the overshoot occurred, after which it then flowed in the positive direction (forward motion). All the other channels were flowing in the forward direction prior to the overshoot and continued to flow in the positive direction, with minor changes in magnitude post the explosion. The flow was smooth for the entire duration of this test (6kW closed system), with a minor transition period. The mass flow rate did not generally increase at this operating condition, but the oscillations minimised.

Out-of-phase behaviour between channel 1 and channel 2 was again observed, as was in-phase conduct between channel 3 and channel 4 (down-comer). The condenser's output temperature increased, peaked and stabilised just below 30°C at steady-state conditions.

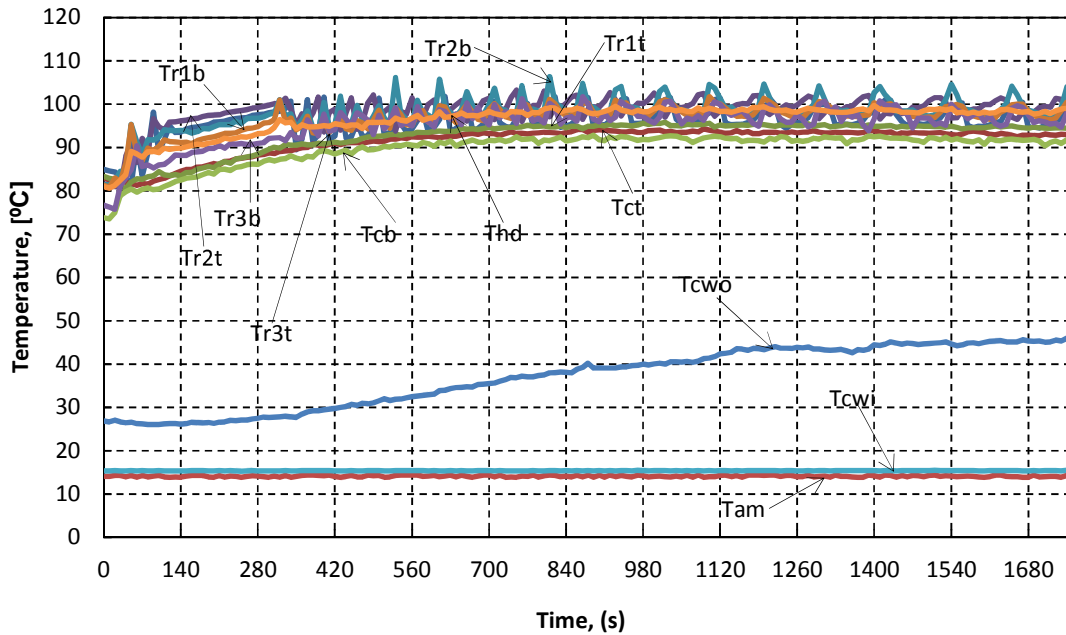


Figure 5.13: Temperature as a function of time of a 9kW test closed system

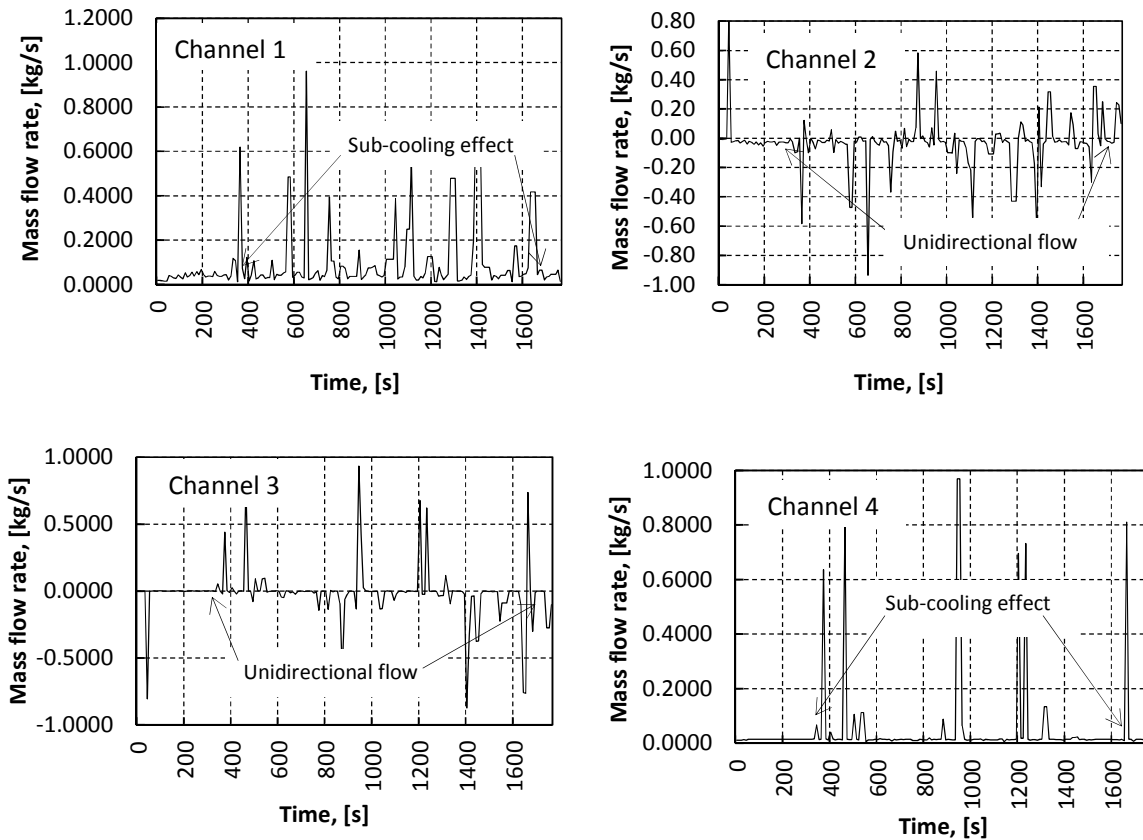


Figure 5.14: Mass flow rate as a function of time in channels 1, 2, 3 & 4 of a 9kW closed system

At high-power operating conditions (9kW), with the system operating not open to the atmosphere, the start-up transient conditions were limited below 140 seconds. At this operating condition, the temperature rose rather rapidly from 75°C, reaching stability at approximately 350 seconds after a minor overshoot. The system maintained steady-state temperature conditions for the entire duration of the test after that. It is clear from Figure 5.13 that the top temperatures of the risers were fluctuating around 100°C, hitting 105°C at times, while the cooling system's outlet temperature rose noticeably and settled just above 45°C. The mass flow rates in Figure 5.14 (channels 1, 2, 3 and 4) show that the fluid movement was stable but with periodic oscillations, unlike at low- and medium-power operating conditions, when oscillations were not so severe.

Interaction between channels 2 and 3 can be witnessed in Figure 5.14 (channels 2, 3 and 4), which shows that the flow rates in channel 2 and 3 were low on average, with back and forth (forward and reverse flow) overshoots. The actions of channel 2 affected the flow and stability of channel 3. Similar conduct between riser 1 and the down-comer's mass flow rates can also be noted in Figure 5.14 (channels 1 and 4). Channels 2 and 3 were general flowing in the reverse direction, while channel 3 and the down-comer remained in the forward flow direction (see Figure 5.14, channels 1, 2, 3 and 4).

Channels 1 and 4 were buoyancy dominated, while channels 2 and 3 were unidirectional with mixed-mode oscillations with a further increase in temperature. The average magnitude of the mass flow rate did not change at this power input (9kW) after closing the valve, but definitely increased the amplitude of the oscillations. It is evident from Figure 5.14 that the flow was pulsating as the quality of fluid increases (vapour generation), which caused periodic oscillations with high peaks. Vibrations were minimised rigorously and the manageability of the system was acquired quicker under this operating condition.

5.2.3 Heat pipe mode

One of the objectives of this study was to operate the two-phase flow multi-channel parallel system as a heat pipe. Heat pipes transfer heat from an evaporator to a condenser over comparatively long distances through vaporising the working fluid. The vapour transports heat to the heat sink, where heat is released to a cooling medium. The condensate is taken back to the evaporator through gravitational force. Heat pipes are commonly utilised where a simple, flexible and lightweight heat-removal structure is required and the use of conventional heat pipes is not viable. This method of heat removal is known to be the most common passive heat removal in two-phase heat transfer systems, hence it was investigated in this study to examine its performance in a multichannel parallel-loop system.

In this operation, the valve connecting the experimental setup with the expansion tank open to the atmosphere was closed. The cooling was initially switched off and the ventilation system was opened to release built-in pressure and steam as the power was progressively increased. The system was powered at 9 kW and maintained for at least 30 minutes. The flow started as a single-phase smooth flow and transited to two-phase flow as heat was continuously injected into the system. The system was heated continuously until boiling was reached. This was evident by the steam escaping in the ventilation system. Steam was allowed to escape for some time to relieve the system of pressure build-up and air stemming from liquid breakdown. The pressure gauge was monitored constantly for any increase in pressure to beyond atmospheric pressure. No rise was observed in the pressure gauge after the ventilation system was opened to maintain the system at atmospheric pressure during power increases.

After steady boiling was ascertained, the power and ventilation system were simultaneously switched off. At the same time cooling was turned on at full rate from the water tap to rapidly cool the system. At this point, bubbly boiling of the water in the steam drum was observed and the entire system was experiencing the bubbly boiling regime. The pressure gauge mounted on the steam drum indicated a gradual pressure drop to below atmospheric pressure. Bubbly boiling continued in all the channels and the steam drum while pressure continued to fall to minus one (-1) bar. After the pressure in the system had reached -1 bar, it rose gradually while boiling was uninterrupted. Bubbly boiling in the system stopped when the pressure gauge indicated minus half (-1/2) bar in rising mode.

Temperatures and pressure drops were measured using thermocouples and differential pressure sensors. Data was captured using an Agilent data acquisition unit and plotted in the figures below for further analysis.

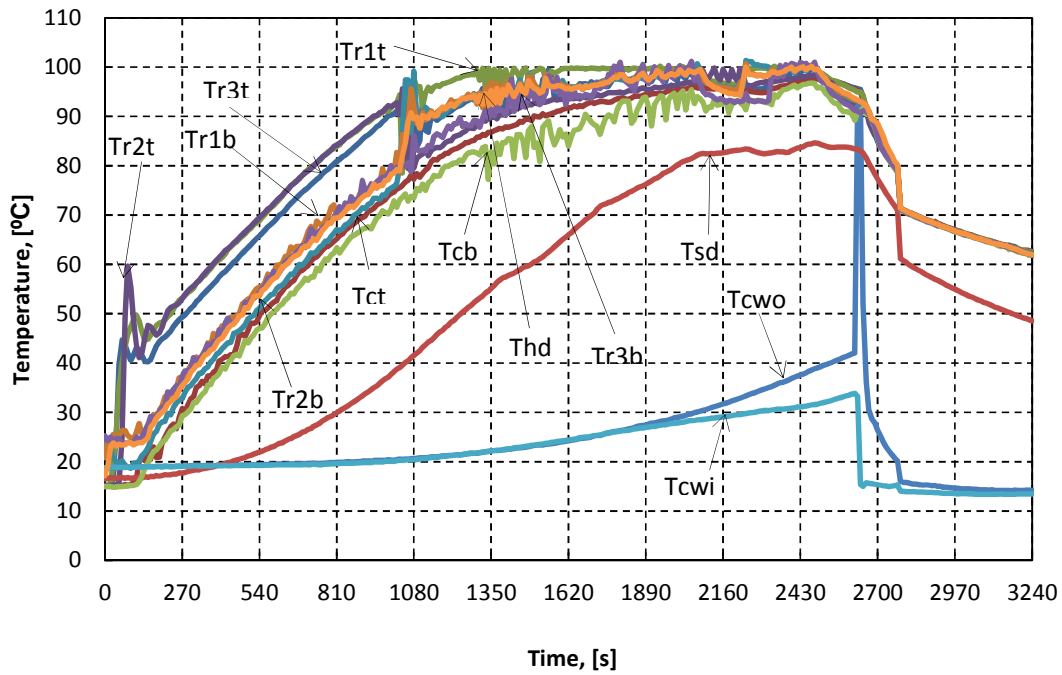


Figure 5.15: Temperature as a function of time of a 3x3kW test heat pipe operation mode

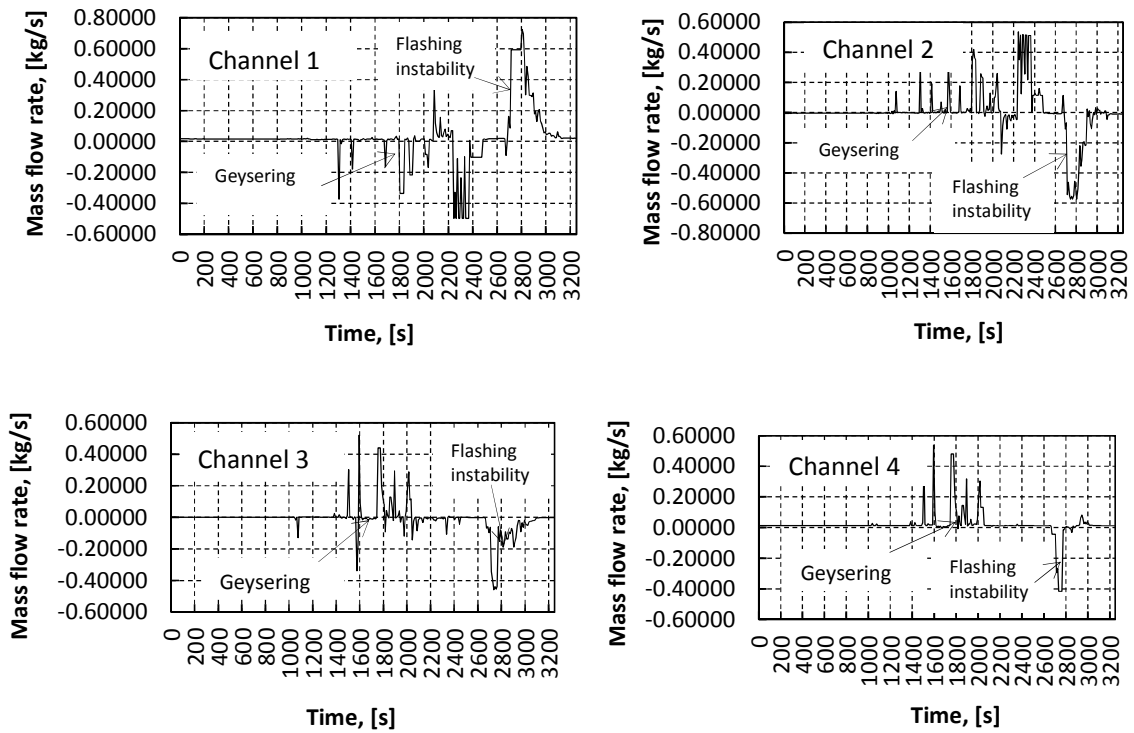


Figure 5.16: Mass flow rate as a function of time in channels 1, 2, 3 & 4 of a 3X3kW heat pipe mode

For heat pipe mode operation the system was powered at 3 X 3kW for the intervals as explained above. Under this condition a typical transient start-up response was noticed in approximately the first 50 to 150 seconds when, after overcoming friction, the system's temperature rose sufficiently. Figure 5.15 shows that a minor overpass was experienced at approximately 1 080 seconds before the two-phase flow reached stability, with a maximum temperature of 100°C. The system maintained boiling at steady conditions without cooling being turned on. The power and ventilation system were then both switched off and cooling was simultaneously turned on at 1 890 seconds and the entire system started bubbly boiling instantaneously.

The cooling system (water-cooled condenser) removed heat rapidly from the experimental set-up, dropping temperatures severely and maintaining pressure in the steam drum. Under this condition (heat pipe mode), the system sustained bubbly boiling even at low temperatures (approximately 65°C). Boiling ceased when temperatures fell to below 60°C.

Figure 5.16 shows that the fluid was initially flowing with no major instabilities in all four channels in a forward direction. The smooth flow was terminated shortly after the overshoot at 1 080 seconds and bubbly boiling commenced thereafter. The sudden introduction of oscillations materialised from an additional buoyancy force in the system due to a continuous increase in temperature. The two-phase flow rates become chaotic, with occasional reversal mode in all channels during the bubbly boiling phase. This mass flow rate conduct was sustained even at low temperatures. According to the mass flow rate graphs, there was a robust interaction (out-of-phase) between the fluid flow of riser 1 and 2, whereas channel 3 and the down-comer experienced a sudden shift from out of phase to in phase.

The heat pipe mode operation possessed Type II geysering and flashing-induced instabilities. Type II instability is associated with high power operation and steam void formation, as explained in the previous sections. Flashing instability materialised from the combination of high power and increased inlet (bottom) temperatures. Geysering instability resulted from the system operating with low pressure and low steam quality. For heat pipe mode operation, the system was functioning at pressures below atmospheric pressure and boiling was established at temperatures below 100°C. The quality of steam generated was fairly low due to the low system pressure. These kinds of instabilities in a two-phase natural circulation system operated at low pressure were also witnessed by Jiang et al. (1995) and Marcel et al. (2010).

5.3 Theoretical Simulation Program Results

One of the objectives of this study was to develop a computer program that would simulate the two-phase flow response in a multi-parallel channel system. The program was developed and tested using the same inputs as the experimental setup. The geometric configuration and material properties of the experimental investigations were also used in the simulation code. The reasoning behind the development of the program was for one to be able to predict the comporment of a passive two-phase flow system and make reasonable engineering decisions without conducting experimental investigations. The heating elements were subjected to three different power inputs (2kW, 6kW and 9kW) and various kinds of operations. The sequencer was simulated to provide temperature and mass flow rate data for each time step exploited from the locations, as indicated in Figure 5.17.

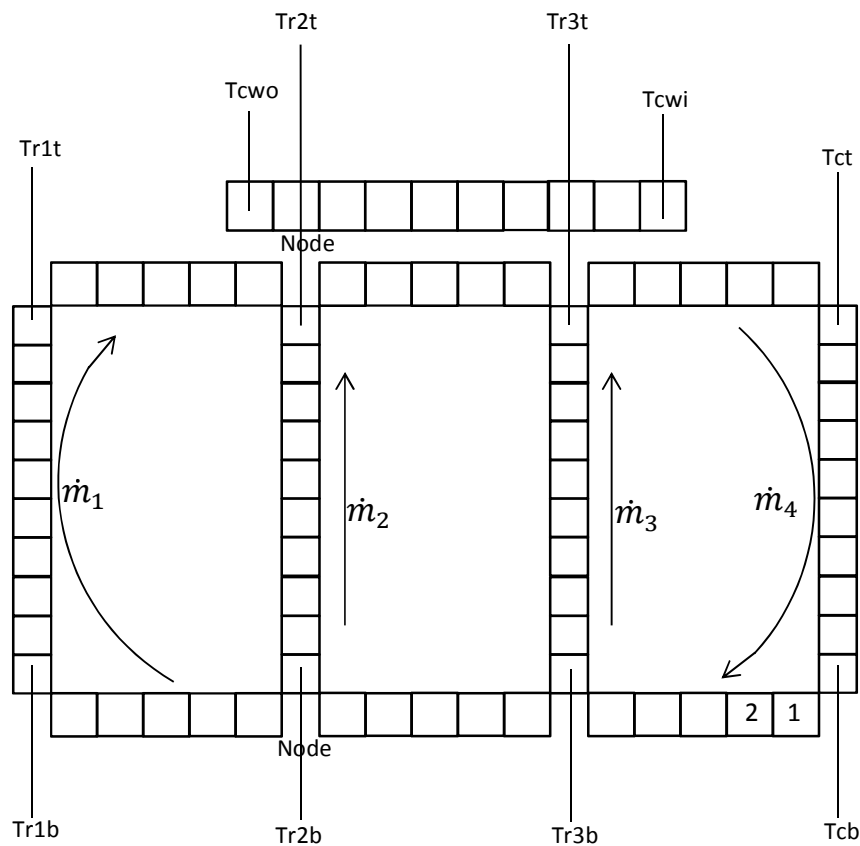


Figure 5.17: Simulation mass flow rates and temperature measuring locations

- Tr1t - top temperature of the left riser
- Tr1b - bottom temperature of the left riser
- Tr2t - top temperature of the middle riser
- Tr2b - bottom temperature of the middle riser

- Tr3t - top temperature of the right riser
- Tr3b - bottom temperature of the right riser
- Tct - top temperature of the down-comer
- Tcb - bottom temperature of the down-comer
- Tcwo - outlet temperature of the cooling water
- Tcwi - inlet temperature of the cooling water

The down-comer's mass flow rate was achieved by summing the instantaneous mass flow rate in each channel. The data obtained from different powering inputs and various modes of operation is plotted and analysed in the following sections.

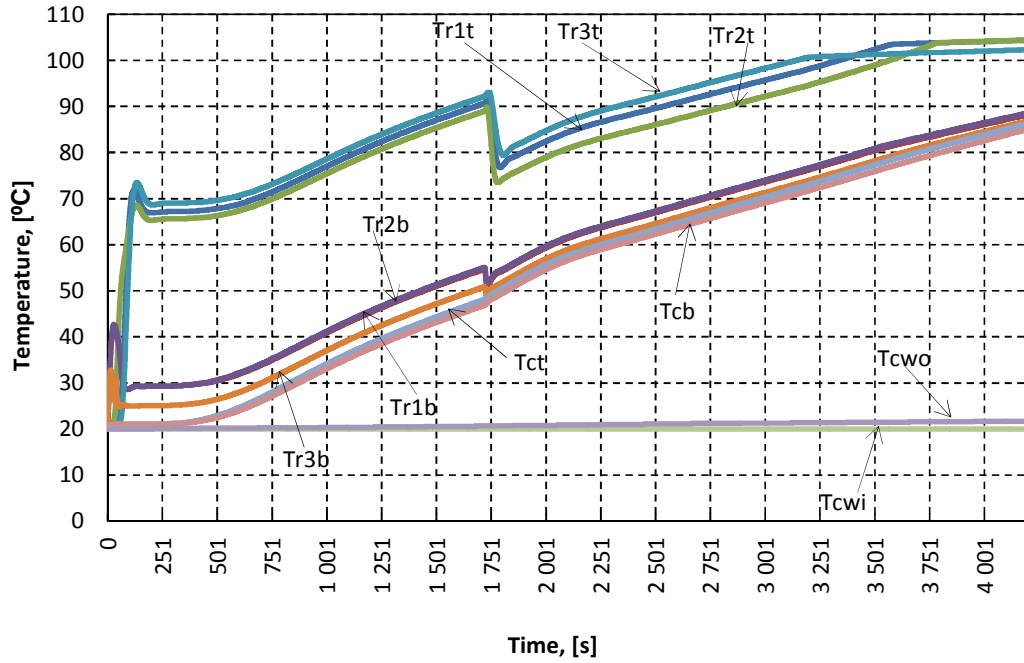


Figure 5.18: Temperature as a function of time of a 3kW test

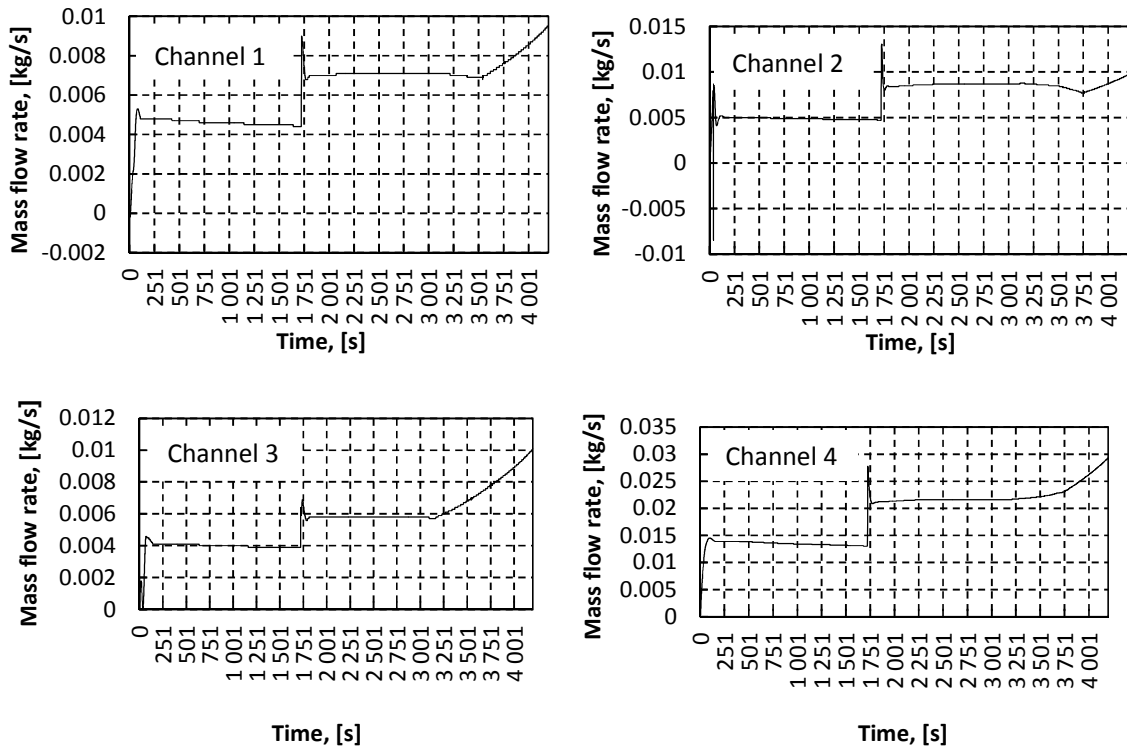


Figure 5.19: Mass flow rate as a function of time in channels 1, 2, 3 & 4 of a 3kW test

Under low-power operating conditions (3kW), the system experienced start-up transient response in the first 250 seconds (see Figures 5.18 and 5.19). After overcoming the friction, the temperatures rose faster while the mass flow rates in all the channels flowed at a constant rate in the forward direction. The graphs show that an overshoot was experienced at 1 750 seconds, after which temperature fell and picked up again smoothly until steady-state conditions were obtained after 3 250 seconds. After the overshoot at 1 750 seconds, all mass flow rates went up and settled at a higher rate than prior to the overpass. A sudden increase in mass flow rate resulted from additional buoyancy generation due to a continuous heat addition and steam void formation. It can be observed in Figure 5.19 (channels 1, 2, 3 and 4) that the mass flow rates maintained the higher rate persistently until yet another gain in buoyancy force as the top risers' temperatures were settling at 103°C. From this point onward, the system was dominated by buoyancy force, hence the mass flow rates in all the channels were rising linearly. This kind of performance is indeed associated with Type I instability.

It was noted in relation to this condition that the simulation result eventually reaches temperature stability, unlike the experimental test subjected to similar conditions and duration. It was further noted that the maximum settling temperature for the simulation was 103°C, while the experimental test settled at approximately 80°C maximum. In the simulation test the transient start-up response duration was less than in the experimental study, viz. 250 and 800 seconds respectively. The simulation test is more slick (less violence and chaos) than the experimental results, and none of the channels (risers and down-comer) experienced reversal flow at low-power operating conditions. In general, the flow performance and categories of instabilities experienced during the practical test were also confirmed in the simulation test. However, the simulation test revealed that all channels assumed in-phase conduct, while the experimental test states that only channels 3 and 4 were in phase.

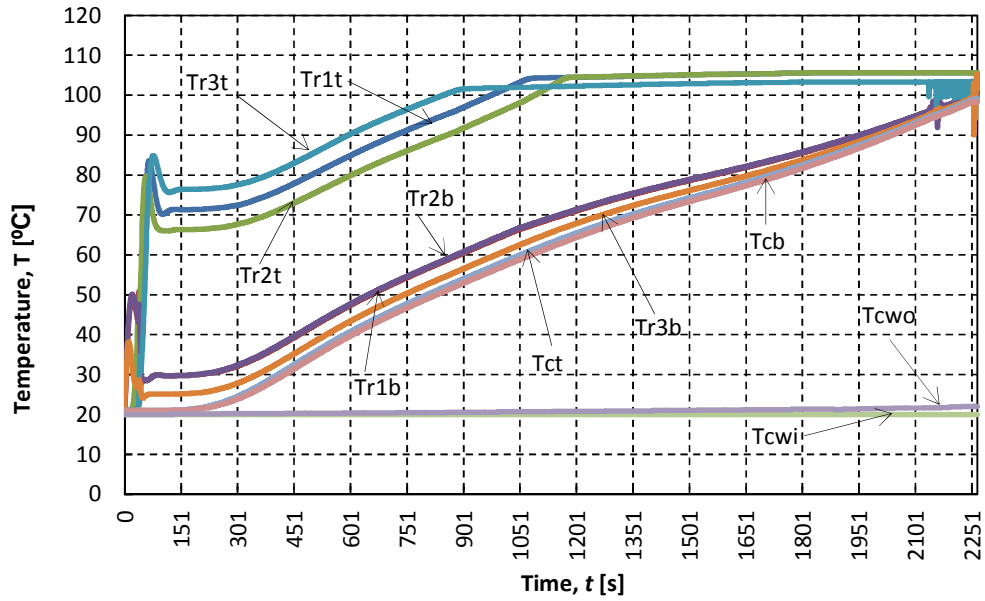


Figure 5.20: Temperature as a function of time of a 6kW test

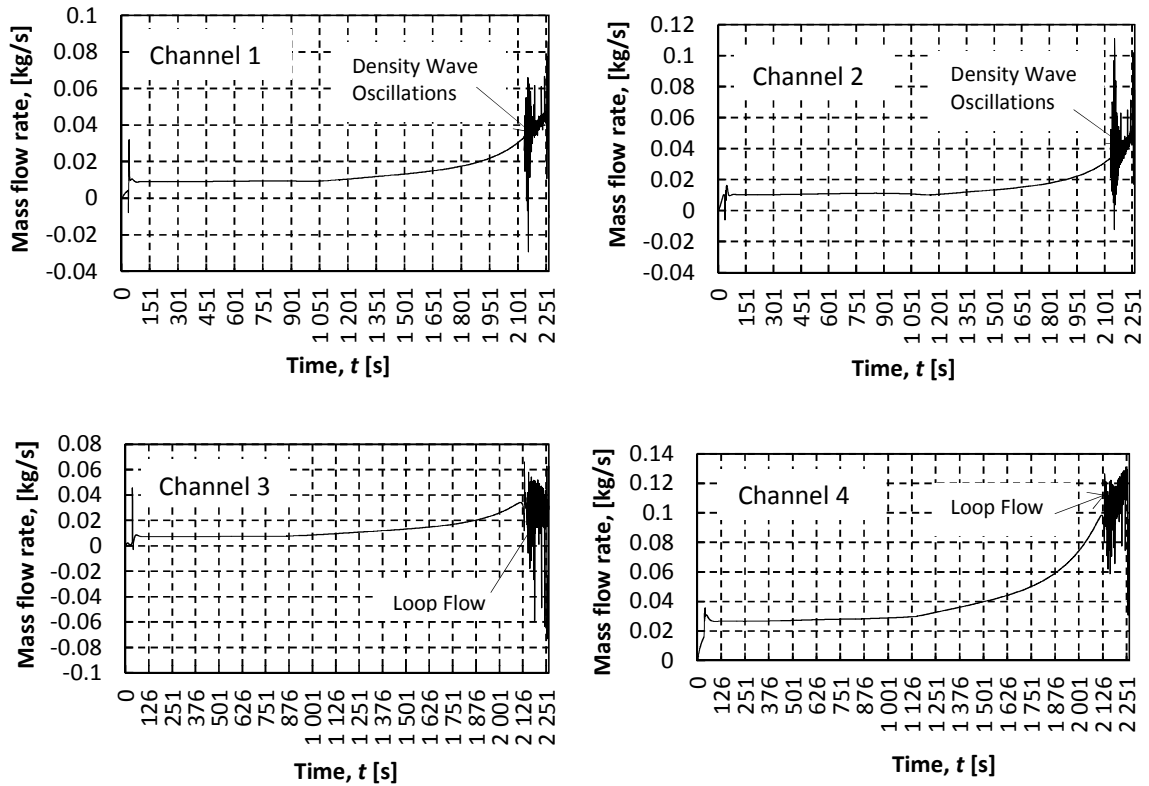


Figure 5.21: Mass flow rate as a function of time in channels 1, 2, 3 & 4 of a 6kW test

According to Figures 5.20 and 5.21, at medium power conditions (6kW), the system experienced a start-up transient response where the temperature increased rapidly with fluid being motionless due to gravitational force overtaking buoyancy force. The duration of the start-up transient response lessened to below 150 seconds compared to the 250 seconds of the experimental test under the same conditions. After overcoming friction, temperatures rose effortlessly until the risers' top temperatures reached a steady-state condition of 105°C maximum at approximately 1 200 seconds. The mass flow rate maintained steady circulation for at least the first 1 000 seconds after overcoming friction. However, the mass flow rates started increasing effortlessly in all channels after the top temperatures of the risers settled above 100°C (see Figure 5.21, channels 1, 2, 3 and 4). The increase in mass flow rates was triggered by the formation of the steam void and the gradual buoyancy force generation from continuous heat addition into the system.

The riser's bottom temperatures continued to rise past 1 200 seconds. Riser 3's top temperature converted to chaotic conduct as the bottom temperatures of the risers approached the top temperatures of the risers; at this point the entire system was undergoing bubbly boiling. Bubbly boiling of the entire system between 2 100 and 2 250 seconds is also evident in the mass flow rate graphs. It is evident from Figure 5.21 that, in this region, the two-phase flow formed loops dominated by buoyancy force as the power continued to increase. This kind of performance is associated with Type II instabilities and flashing-induced instability. Flow behaviour maintained in-phase relations between channels 1 and 2, while a shift from in-phase to out-of-phase conduct between channels 3 and 4 is apparent from Figure 5.21 (channels 1, 2, 3 and 4). The chaotic behaviour of channel 3's top temperature materialised from fast-rising sub-cooled liquid at the header (from the down-comer) into the steam drum through channel 3 due to an increased buoyancy force.

In general, the mass flow rates were flowing in the forward direction for the duration of this test, with minor overshoots in the reverse direction during bubbly boiling of the entire system. Again, there was a strong correlation between the experimental results and the simulation test.

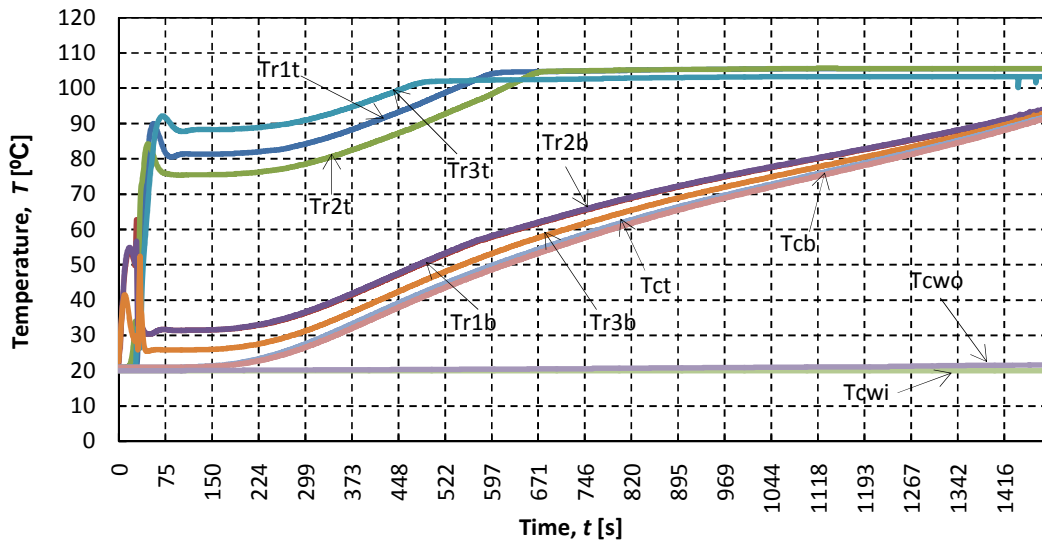


Figure 5.22: Temperature as a function of time of a 9kW test

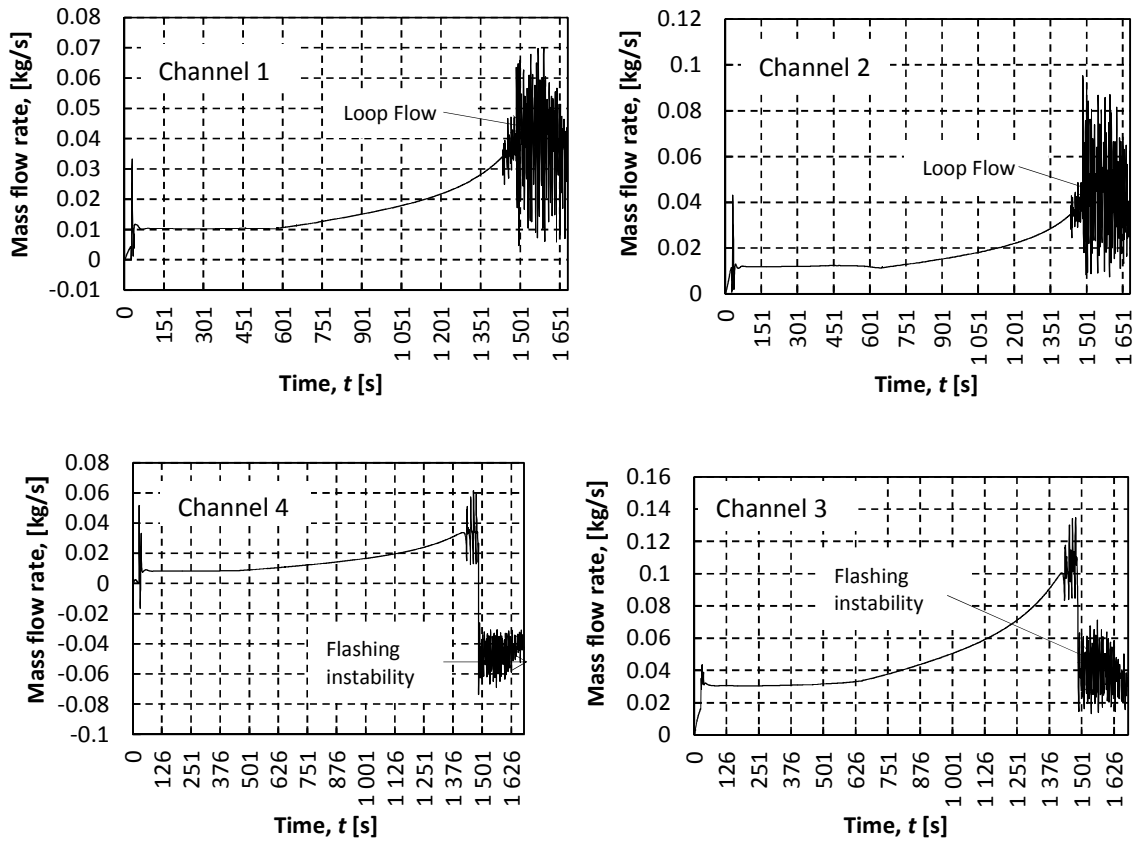


Figure 5.23: Mass flow rate as function of time in channels 1, 2, 3 & 4 of a 9kW test

Under high power (9kW) operating condition, the transient start-up response duration reduced to nearly 75 seconds (see Figures 5.22 and 5.23). After overcoming friction, the temperatures dropped slightly and rose efficiently, with the risers' top temperatures reaching steady-state conditions at roughly 670 seconds. The bottom temperatures of the risers and down-comer rose effortlessly beyond 90°C, after which channel 3's top temperature started showing minor instabilities due to the entire system reaching bubbly boiling and sub-cooled boiling rising fast into the steam drum through channel 3.

The mass flow rate graphs (Figure 5.23, channels 1, 2, 3 and 4) show that the two-phase fluid was flowing at a constant rate of approximately 0.01 kg/s in all the channels after disabling friction. The constant circulation rate started increasing forcefully shortly after the risers' top temperatures reached stability at 670 seconds. After the bottom temperatures of the risers increased past 90°C, the mass flow rates became oscillatory in all channels, with riser 3 flowing in the reverse direction. In this region the system was undergoing flashing-induced instability. At this phase, the down-comer's mass flow rate fell, but it maintained its forward directional flow. This simulation test possessed Type II instability, where the continuous increase in temperature generated a buoyancy force, which later created reverse flow in channel 3.

Figure 5.23 show that channels 1 and 2 possessed similar mass flow rate demeanour (in-phase), while channel 3 and the down-comer responded in the same manner (in phase). Similar conduct was also observed in the experimental test operated as an open system powered at 9kW. It is interesting to see that the channels do not necessarily assume the same behaviour, even if are heated equally. It is further noted that increasing power does not necessarily increase average flow rate.

6 CONCLUSIONS AND RECOMMENDATIONS

This study examined the start-up transient and steady-state response of a two-phase fluid natural circulation in a multi-parallel channel system. A three parallel loop system was designed, built and used to perform the practical investigations. A one-dimensional computer program was also coded to study the response of the test facility subjected to various power inputs at constant pressure (atmospheric). It is evident from the experimental investigations of this study that heat transfer into a fluid results in water breakdown and air materialisation, no matter how airtight the system is. This was also encountered by Vyas et al. (2010) in their investigations in which demineralised water was used. Hence, a pressure release and air ventilation system is a basic requirement of any system undergoing heat addition. The simulation model predictions were validated with the experimental observations (see Chapter 5).

Investigations were carried out over a range of process parameters, i.e. varying power inputs and operation modes under two-phase natural circulation. At least four kinds of instability were observed in this study from different operating factors: Type I instability, Type II instability, geysering and flashing instability. Open system operation mode possessed start-up transient responses that lasted longer compared to the closed system mode of operation. Geysering instability and out-of-phase periodical oscillations between adjacent channels were commonly observed for all the open system natural circulation power excitations. The existence of flashing instability accompanied by mechanical vibrations at high inlet temperatures was one of the instabilities encountered at high power excitation in an open system. Lakshmanan and Manmahan (2010) discovered the same instabilities in their experimental and numerical investigations in parallel-channel natural circulation boiling systems.

To numerically analyse the performance of the designed two-phase natural circulation multi-parallel channel system, the one-dimensional transient equations of change: mass, momentum and energy, were solved through a discretised model for the enforced power excitations and fixed system pressure (atmospheric). The simulation seemed to indicate Type I instability, Type II instability, density wave oscillations, loop flow and flashing-induced instability from various power excitations. The low power performance was dominated by Type I instability with no major oscillations, while the rest of the instabilities were evident at medium and high power inputs. In general, there is a reasonable correlation between the experimental results and the simulation tests, for instance by comparing Figure 5.7 and Figure 5.23 on pages 60 and 79 respectively. The experimental results (Figure 5.7) show that the mass flow rate was flowing with no visible oscillations for at least the first 1400 seconds (see Figure 5.7) in all channels. However instabilities initiated shortly after boiling commencement.

The channels went through different flow instabilities where channels 1 and 2 experienced geysering instability whereas channels 3 and 4 were flashing induced instability dominated (Figure 5.7).

Though, the numerical results (Figure 5.23) show that the flow initially experienced start-up transient response which lasted not longer than 120 seconds which after the fluid's buoyancy force overcame the material's resistivity. And the flow started flowing with no visible instabilities to the forward direction and rose effortless until at approximately 1400 seconds, where all channels went through different instabilities due to the entire system approaching boiling (bottom temperatures of the risers and down-comer approaching 90°C). In this case, channels 1 and 2 went through loop flow instability whereas channels 3 and 4 were flashing instability dominated.

The results obtained through the developed simulation model were also compared to results from similar work done by other researchers (Yun et al., 2008; Jain et al., 2010; Marcel et al., 2010), see Appendix F and were found to be in good agreement. The model predicted the experimental setup performance satisfactorily and therefore is recommended to be used to predict the behaviour of a two-phase natural circulation system and make good engineering decisions. It is recommended that the sub-cooling effect be taken into account in modelling a natural circulation system, as it proved to have an impact on the behaviour of the flow in the system.

Instabilities associated with closed system operation include Type II instability, unidirectional flow and sub-cooling effects at high power excitation. It was evident from this study that mechanical vibrations and chaotic flow rate were drastically minimised at this operating condition, particularly for low- and medium-power inputs. In general, the stability of the two-phase natural circulation in a multi-parallel channel system improved significantly and the low density wave oscillation was eradicated in the closed system operation. Walter (2007) theoretically investigated density wave oscillations in the horizontal parallel tube paths of a natural circulation heat-recovery steam generator and concluded that the stability of the system could be improved by increasing the system pressure. Jiang et al. (1995:122) and Jain et al. (2010:787) also concluded that boiling inception at high pressure is less chaotic and that flow oscillation amplitudes are small.

Heat pipe mode operation instabilities included the geysering effect, followed by flashing instability and boiling. Low steam quality density wave instability was also observed in this operation mode. According to Jiang et al. (1995:117), these instabilities are associated with low pressurised systems. In this mode of operation, mechanical vibrations were minimised and boiling at low temperature was achieved. Heat pipes transfer heat over long distances and are a considerable cheaper method of removing heat in any system.

A further investigation of their applicability, effectiveness and improvement in light water reactors is strongly recommended. This test could be used to provide suggestions for design developments to avoid undesired effects.

It is concluded that the start-up transient response decreases with an increase in power excitation. The increase in power excitation does not necessarily increase the flow rate in the system, but results in more oscillations and flow reversal in some channels. This was also confirmed by Jain et al. (2010:786), Nayak et al. (2006:652) and Zhang et al. (2009:7) in their investigations. According to Nayak et al. (2006:651-652), the channel's mass flow rate could be increased by shortening the riser's length and increasing the area. However, the geometric effect was not considered in this study and is highly recommended to be validated using the closed system operation. Medium power inputs seemed to be less chaotic, more stable and considerably reduced the flow reversal effect in both the closed-system experimental tests and simulation outcomes.

Boiling commencement along with flow reversal and random oscillations are the major challenges of natural circulation systems, even when the channels are heated equally. In-phase and out-of phase behaviour between adjacent channels is another concern for two-phase natural circulation in a multi-parallel channel system. The sub-cooling effect was not considered in this study, but it is highly recommended that is taken into consideration in future investigations.

The interaction effect between adjacent channels was evident at low power operation in the experimental investigation, where the large intensification in channel 1 flow caused reversed flow to occur in channel 2 as a result of the enormous inertia of the coolant in the down-comer. This upturned flow forced hot coolant to be reheated in channel 2, and the process is repeated. Marcel et al. (2010) encountered a similar problem in their experimental study on flashing-induced instabilities in dual parallel channels. The statement of Lee and Pan (1999:32) was validated in this study, namely that a dual-channel system exhibits similar conduct to a three- or more channel system. This was confirmed by comparing the results of this study with those obtained by White (2011) in a dual-loop system and Jain et al. (2010) in a quadrilateral channel system, which turned out to display similar conduct.

7 REFERENCE

- Cengel Y.A. 2006. *Heat and mass transfer: A practical approach*, 3rd ed., New York: McGraw-Hill.
- Cengel Y.A. & Cimbala J.M. 2006. *Fluid mechanics: Fundamentals and applications*, 1st ed., New York: McGraw-Hill.
- Dobson R.T. 2014. Personal meeting. February. Stellenbosch.
- Dobson R.T. & Ruppertsberg J.C. 2008. A novel closed loop thermosyphon heat pipe reactor cavity cooling system (RCCS) for a pebble bed modular reactor (PBMR).
- Dobson R.T. 2006. One dimension computer simulation of a natural circulation system.
- Furuya M., Inada F., Van der Hagen T.H.J.J. 2005. Flashing-induced density wave oscillations in a natural circulation BWR-mechanism of instability and stability map. *Nuclear Engineering and Design*. 235 (2005): 1557-1569.
- Goudarzi N. & Talebi S. 2013. Linear stability of a double-channel two-phase natural circulation loop. *Progress in Nuclear Energy*. 67 (2013): 114-123.
- IAEA-TECDOC-1474. 2005. Natural circulation in water cooled nuclear power plants: phenomena, models, and methodology for system reliability assessments. November 2005.
- Jain V., Kulkarni P.P., Nayak A.K., Vijayan P.K., Saha D., Sinha R.K. 2011. Steam drum level dynamics in a multiple loop natural circulation system of a pressure-tube type boiling water reactor. *Annals of Nuclear Energy*. 38 (2011): 2227-2237.
- Jain V., Nayak A.K., Vijayan P.K., Saha D., Sinha R.K. 2010. Experimental investigations on the flow instability behaviour of a multi-channel boiling natural circulation loop at low-pressures. *Experimental Thermal and Fluid Science*. 34 (2010): 776-787.
- Jiang S.Y., Yao M.S., Bo J.H., Wu S.R. 1995. Experimental simulation study on start-up of the 5MW nuclear heating reactor. *Nuclear Engineering and Design*. 158 (1995): 111-123.
- Krepper E. & Beyer M. 2010. Experimental and numerical investigations of natural circulating phenomena in passive safety systems for decay heat removal in large pools. *Nuclear Engineering and Design*. 240 (2010): 3170-3177.
- Kröger D.G. 1998. Air-cooled heat exchangers and cooling towers: Thermal flow performance evaluation and design. Stellenbosch: Stellenbosch University.
- Lakshmanan S.P. & Pandey M. 2010. Numerical investigations of startup instabilities in parallel-channel natural circulation boiling systems. *Science and Technology of Nuclear Installations*. 2010: 1-8.
- Lee J.D. & Pan C. 1999. Dynamics of multiple parallel boiling channel systems with forced flows. *Nuclear Engineering and Design*. 192 (1999):31-44.
- Liedberg H., Jonker D., Brealz M.B. 2003. Certificate of calibration of a platinum resistance thermometer (PRT). *CSIR national metrology laboratory (NML)*. May 2003.

Lu D., Xiao Z., Chen B. 2010. A new method to derive one set of scaling criteria for reactor natural circulation at single and two-phase conditions. *Nuclear Engineering and Design*. 240 (2010): 3851-3861.

Marcel C.P., Rohde M., Van der Hagen T.H.J.J. 2010. Experimental investigations on flashing induced instabilities in one and two-parallel channels: A comparative study. *Experimental Thermal and Fluid Science*. 34 (2010): 879-892.

Mills A. F. 1999. Heat transfer, 2nd ed., Prentice Hall, Upper Saddle River.

Nayak A.K. & Sinha R.K. 2007. Role of passive systems in advanced reactors. *Progress in Nuclear Energy*. 49 (2007): 486-498.

Nayak A.K., Lathouwers D., Van der Hagen T.H.J.J., Schrauwen F., Molenaar P., Rogers A. 2006. A numerical study of boiling flow instability of a reactor thermosyphon system. *Applied Thermal Engineering*. 26 (2006): 644-653.

Rao N.M., Sekhar C., Maiti B., Das P.K. 2006. Steady-state performance of a two-phase natural circulation loop. *International Communication in Heat and Mass Transfer*. 33 (2006): 1042-1052.

Reyes J. & Cleveland J. 2005. Natural circulation in water cooled nuclear power plants: Phenomena, models, and methodology for system reliability assessments. IAEA-TECDOC-1474. November 2005.

Ruppersberg J.C. 2008. Transient modelling of a loop thermosyphon. MScEng thesis. Stellenbosch. Stellenbosch University.

Schulz T.L. 2006. Westinghouse AP1000 advanced passive plant. *Nuclear Engineering and Design*. 236 (2006): 1547-1557.

Sinha R.K. & Kakodkar A. 2006. Design and development of the AHWR – the Indian thorium fuelled innovative nuclear reactor. *Nuclear Engineering and Design*. 236 (2006): 683-700.

Swapnalee B.T. & Vijayan P.K. 2011. A generalized flow equation for single phase natural circulation loops obeying multiple friction laws. *International Journal of Heat and Mass Transfer*. 54 (2011): 2618-2629.

Vecchiatto P. 2014. Nuclear power at the centre of SA'S energy mix, says Joemat-Pettersson, <http://www.bdlive.co.za/business/energy/2014/07/21/nuclear-power-at-the-centre-of-sas-energy-mix-says-joemat-pettersson>

Vijayan P.K. & Austregesilo H. 1994. Scaling laws for single-phase natural circulation loops. *Nuclear Engineering and Design*. 152 (1994): 331-347.

Vyas H.P., Raj V.V., Nayak A.K. 2010. Experimental investigations on steady state natural circulation behavior of multiple parallel boiling channel system. *Nuclear Engineering and Design*. 240 (2010): 3862-3867.

Walter H. 2007. Density wave oscillations in the horizontal parallel tube paths of the evaporator of a natural circulation heat recovery steam generator – A theoretical investigation. *WSEAS Transactions on Heat and Mass Transfer*. Vol. 2 (2007): 1-27.

White F.M. 1999. *Fluid Mechanics*, 4th ed. New York: McGraw-Hill.

White H.A. 2011. Investigating instabilities in a multi-channel thermosyphon Loop. Final-year project. Stellenbosch. University of Stellenbosch.

World Nuclear Association. 2014a. Chernobyl Accident 1986, <http://www.world-nuclear.org/info/Safety-of-Plants/Chernobyl-Accident>

Yun G., Qiu S.Z., Su G.H., Jia D.N. 2008. Theoretical investigations on two-phase flow instability in parallel multichannel system. *Annals of Nuclear Energy*. 35 (2008): 665-676.

Zhang Y.J., Su G.H., Yang X.B., Qiu S.Z. 2009. Theoretical research on two-phase flow instability in parallel channels. *Nuclear Engineering and Design*. Vol. 239 (2009): 1-10.

APPENDIX A: CONDENSER DESIGN CALCULATIONS

The condenser's size calculation was adapted from Cengel (2006: Chapter 10) under the boiling and condensation section. Since the maximum saturated steam temperature was expected to reach 105°C, the outer surface temperature of the condenser was assumed to be 95°C when the inlet cooling water temperature was at 20°C. It was decided to stagger the configuration of the condenser for optimum heat evacuation and simplicity. The material of the condenser was copper based because it is easier to machine and is a good conductor of heat. Copper is also cheaper than stainless steel and also withstands rust and corrosion to a certain extent. Copper tubes were also readily available at the Stellenbosch University Mechanical Engineering Laboratory, so it made sense to utilise it to cut down the costs of the project.

The maximum power to be injected into the system was decided to be 9 kW, i.e. 3 kW per heating element, based on the size of the system that was designed and the amount of working fluid to be heated. Table A.1 shows the optimum size of the condenser required to evacuate all the heat (9 kW) injected into the system. However, the condenser constructed for this experimental facility was twice the optimum size due to the copper tube size (28 mm, OD) that was available at the laboratory and to be able to increase the power injection, if need be. The calculations were done in Microsoft Excel® for simplicity and easier updating.

Table A.1: Condenser sizing calculations

Design Calculations of the Condenser		
Parameters	Optimum Design	Actual Design
Outer pipe surface Temperature, T_s , [°C]	95	95
Steam Temperature, T_{sat} , [°C]	105	105
Enthalpy of vaporization at 105 °C, h_{fg} , [kJ/kg]	2.24E+06	2.24E+06
Density of vapor at 105 °C, ρ_v , [kg/m ³]	0.171205	0.171205
Film Temperature, T_f , [°C]	100	100
Liquid density at film temperature, ρ_l , [kg/m ³]	957.9	957.9
Liquid dynamic viscosity at film temperature, μ_l , [kg/m.s]	2.82E-04	2.82E-04
Liquid specific heat at film temperature, c_{pl} , [J/kg.K]	4217	4217
Liquid thermal conductivity, k_l , [W/m.K]	0.679	0.679
Modified heat of vaporization, h_{fg}^* , [J/kg]	2272175.6	2272175.6
Heat transfer coefficient, h , [W/m ² .°C]	15912.41095	12301.17165
Outside diameter of each tube, D_o , [m]	0.01	0.028
Length of the tube, l , [m]	0.291	0.291
Heat transfer surface area per tube, A_s , [m ²]	0.009142035	0.025597697
Rate of heat transfer during condensation per tube, \dot{Q} , [kW]	1.454718119	3.148816638
Total number of pipes	7	7
Total rate of heat transferred to the condenser, \dot{Q}_{tot} , [kW]	10.18302683	22.04171647
Rate of steam condensation per pipe, \dot{m}_{cond} , [kg/s]	0.000640231	0.001385816
Total rate of steam condensation, $\dot{m}_{totalcond}$, [kg/s]	0.00448162	0.00970071

Formulae, adapted from Cengel (2006)

Film temperature is given by:
$$T_f = \frac{(T_{sat} + T_s)}{2}, [\text{°C}]$$

Modified latent of heat of vaporisation is:
$$h_{fg}^* = h_{fg} + 0.68C_{p,l}(T_{sat} - T_s), [\text{J/kg}]$$

Heat transfer coefficient per horizontal tube is:
$$h = h_{horiz} = 0.729 \left[\frac{g\rho_l(\rho_l - \rho_v)h_{fg}^*k_l^3}{\mu(T_{sat} - T_s)D} \right]^{1/4},$$

[W/m².°C]

The rate of heat transfer during this condensation process becomes:
$$\dot{Q} = hA_s(T_{sat} - T_s), [\text{kW}]$$

where heat transfer surface area per tube is :
$$A_s = \pi D_o L, [\text{m}^2]$$

The rate of steam condensation per pipe is:
$$\dot{m}_{condensation} = \frac{\dot{Q}}{h_{fg}^*}, [\text{kg/s}]$$

APPENDIX B: DETAILED DERIVATION OF THE EQUATIONS OF CHANGE FOR THE MATHEMATICAL MODEL

This section gives the derivation of the equations of change used in the simulation program. The fundamental principles of fluid mechanics and dynamics were used in the derivation of the equations of change. These fundamental principles were used in the form of the Reynolds transport theorem to shift from the system to the control volume formulation, as shown in Figure B.1 and Figure B.2

B.1 Conservation of Mass Flow Rate /Continuity Equation

The conservation of mass relation for a closed system undergoing a change requires that the mass of the system remains constant during the process. However, for a control volume, mass can cross the boundaries, as depicted in Figure B.1.

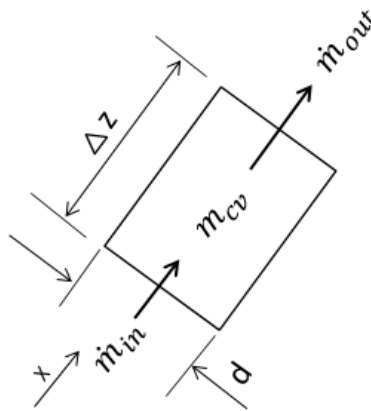


Figure B.1: Fixed control volume for continuity

The change in mass with respect to time of the fixed control volume through which a fluid is flowing can be expressed simple as

$$\frac{\Delta m_{cv}}{\Delta t} = \dot{m}_{in} - \dot{m}_{out} \quad (\text{B. 1})$$

which can be stated as

$$\left(\begin{array}{c} \text{Net change in mass flow} \\ \text{rate within the control} \\ \text{volume during } \Delta t \end{array} \right) = \left(\begin{array}{c} \text{Total mass flow rate} \\ \text{entering the control} \\ \text{volume} \end{array} \right) - \left(\begin{array}{c} \text{Total mass flow rate} \\ \text{leaving the control} \\ \text{volume} \end{array} \right)$$

where \dot{m}_{in} and \dot{m}_{out} are the total rates of mass flow into and out of the control volume, and dm_{cv}/dt is the rate of change of mass within the control volume boundaries.

B.2 Conservation of Momentum

Newton's second law states that the sum of all external forces acting on a system is equal to the time rate of change in linear momentum. Applying the Reynolds transport theorem to the system to formulate the system using control volumes, the general linear momentum equation (Cengel & Cimbala, 2006:234) can be expressed as

$$\sum \vec{F} = \frac{d}{dt} \int_{cv} \rho \vec{v} dv + \int_{cs,out} \rho \vec{v} (\vec{v}_r \cdot \vec{n}) dA_x - \int_{cs,in} \rho \vec{v} (\vec{v}_r \cdot \vec{n}) dA_x \quad (\text{B.2})$$

which can be stated as

$$\left(\begin{array}{l} \text{The sum of all} \\ \text{external forces} \\ \text{acting on a CV} \end{array} \right) = \left(\begin{array}{l} \text{The time rate of change} \\ \text{of the linear momentum} \\ \text{of the contents of the CV} \end{array} \right) + \left(\begin{array}{l} \text{The net flow rate of linear} \\ \text{momentum out of the control} \\ \text{surfaces (CS) by mass flow} \end{array} \right)$$

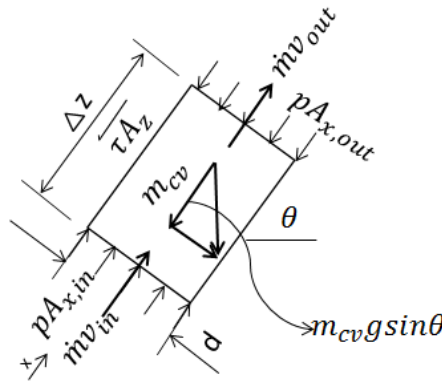


Figure B.2: Fixed control volume for 1-D flow linear momentum (Figure 4.2 repeated)

According to Cengel and Cimbala (2006:234), for a fixed control volume the fluid velocity relative to the control surface $\vec{v}_r = \vec{v}$, and then equation (B.2) becomes

$$\sum \vec{F} = \frac{d}{dt} \int_{cv} \rho \vec{v} dv + \int_{cs,out} \rho \vec{v} (\vec{v} \cdot \vec{n}) dA_x - \int_{cs,in} \rho \vec{v} (\vec{v} \cdot \vec{n}) dA_x \quad (\text{B.3})$$

Applying equation (B.3) to the control volume in Figure B.2, the term on the LHS of equation (B.3) becomes

$$\sum \vec{F} = pA_{x,in} - pA_{x,out} - \tau A_z - m_{cv} g \sin \theta \quad (\text{B.4})$$

where $m_{cv} = \rho A_x \Delta z$, and substituting into equation (B.4) results in

$$\sum \vec{F} = pA_{x,in} - pA_{x,out} - \tau A_z - \rho A_x \Delta z g \sin \theta \quad (\text{B.5})$$

The integral terms of equation (B.3) can be written in algebraic form on the assumption that density and average velocity across the control volume are nearly constant, hence ρ and v can be taken out of the integral, which results in

First term:

$$\begin{aligned} \frac{d}{dt} \int_{cv} \rho v dV &= \frac{\Delta}{\Delta t} \rho v \int_{cv} dV = \frac{\Delta}{\Delta t} (\rho v \cdot V), \text{ where } V = A_x \Delta z \text{ is the volume of the control volume} \\ &= \frac{\Delta}{\Delta t} (\rho v A_x \Delta z) \end{aligned}$$

Knowing that $\dot{m} = \rho v A_x$, results in

$$\frac{d}{dt} \int_{cv} \rho v dV = \frac{\Delta}{\Delta t} (\dot{m} \Delta z) = \Delta z \frac{\Delta}{\Delta t} (\dot{m}) \quad (\text{B. 6})$$

Second and third terms:

Control surfaces are normal to the flow inlet and outlet areas, then $(\vec{v} \cdot \vec{n}) dA_x = v dA_x$ (Cengel & Cimbala, 2006:236).

$$\begin{aligned} \int_{A_{x,out}} \rho \vec{v} (\vec{v} \cdot \vec{n}) dA_x &= \rho v \int_{A_{x,out}} (\vec{v} \cdot \vec{n}) dA_x \\ &= \rho v \int_{A_{x,out}} v_{out} dA_x \\ &= \rho v A_{x,out} v_{out} \\ &= (\dot{m} v)_{out} \end{aligned} \quad (\text{B. 7})$$

$$\begin{aligned} \int_{A_{x,in}} \rho \vec{v} (\vec{v} \cdot \vec{n}) dA_x &= \rho v \int_{A_{x,in}} (\vec{v} \cdot \vec{n}) dA_x \\ &= (\dot{m} v)_{in} \end{aligned} \quad (\text{B. 8})$$

Substituting equations (B.5), (B.6), (B.7) and (B.8) into equation (B.2) results in

$$p A_{x,in} - p A_{x,out} - \tau A_z - \rho A_x \Delta z g \sin \theta = \Delta z \frac{\Delta(\dot{m})}{\Delta t} + (\dot{m} v)_{out} - (\dot{m} v)_{in} \quad (\text{B. 9})$$

Rearranging equation (B.9) such that the first term on the RHS of equation (B.9) is the subject of the formula results in

$$\Delta z \frac{\Delta(\dot{m})}{\Delta t} = p A_{x,in} - p A_{x,out} - \tau A_z - \rho A_x \Delta z g \sin \theta + (\dot{m} v)_{in} - (\dot{m} v)_{out} \quad (\text{B. 10})$$

The tube diameter is constant, therefore $A_{x,out} = A_{x,in} = A_x$.

Dividing equation (B.10) by A_x results in

$$\frac{\Delta z}{A_x} \frac{\Delta(\dot{m})}{\Delta t} = p_{in} - p_{out} - \tau \frac{A_z}{A_x} - \rho \Delta z g \sin \theta + \left(\frac{(\dot{m}v)_{in} - (\dot{m}v)_{out}}{A_x} \right) \quad (\text{B. 11})$$

Knowing that $-\Delta p = p_{in} - p_{out}$, and $v = \frac{\dot{m}}{\rho A_x}$, equation (B.11) becomes:

$$\frac{\Delta z}{A_x} \frac{\Delta(\dot{m})}{\Delta t} = -\Delta p - \tau \frac{A_z}{A_x} - \rho \Delta z g \sin \theta + \frac{\dot{m}^2}{A_x} \left(\frac{1}{\rho A_{x,in}} - \frac{1}{\rho A_{x,out}} \right) \quad (\text{B. 12})$$

Let $\Delta z = L$, noting that $A_x = \frac{\pi d^2}{4}$ and $A_z = \pi d L$, then $\frac{A_z}{A_x} = \frac{\pi d L}{\frac{\pi d^2}{4}} = \frac{4L}{d}$. Furthermore, τ is the shear

stress opposing movement of the control volume and is represented by both frictional flow and minor losses in a pipe as $\tau = \tau_f + \tau_m$, where

$$\tau_f = \frac{1}{2} C_f \rho v^2 = \frac{1}{2} C_f \frac{\dot{m}^2}{\rho A_x^2} \text{ and } \tau_m = \frac{1}{2} K_m \rho v^2 = \frac{1}{2} K_m \frac{\dot{m}^2}{\rho A_x^2}$$

Therefore,

$$\tau = \frac{1}{2} C_f \frac{\dot{m}^2}{\rho A_x^2} + \frac{1}{2} K_m \frac{\dot{m}^2}{\rho A_x^2} = \frac{1}{2} \frac{\dot{m}^2}{\rho A_x^2} (C_f + K_m) \quad (\text{B. 13})$$

Replacing \dot{m}^2 with $\dot{m}|\dot{m}|$ in equation (B.13) so as to ensure that the shear stress always opposes the flow direction, equation (B.12) becomes

$$\frac{L}{A_x} \frac{\Delta(\dot{m})}{\Delta t} = -\Delta p - 2 \frac{L}{d} \frac{\dot{m}|\dot{m}|}{\rho A_x^2} (C_f + K_m) - \rho L g \sin \theta + \frac{\dot{m}^2}{A_x} \left(\frac{1}{\rho A_{x,in}} - \frac{1}{\rho A_{x,out}} \right) \quad (\text{B. 14})$$

Assign numbers in each control volume, as shown in Figure B.3, and let variable i be the control volume counter in each branch. Furthermore, assigning variable n to count each branch of flow, then equation (B.14) can be expressed as

$$\frac{L_i}{A_{x,i}} \frac{\Delta \dot{m}_n}{\Delta t} = -\Delta p_i - 2 \frac{L_i}{d_i} \frac{\dot{m}_n |\dot{m}_n|}{\rho_i A_{x,i}^2} (C_{f,i} + K_{m,i}) - \rho_i g L_i \sin(\theta_i) + \frac{\dot{m}_n^2}{A_{x,i}} \left(\frac{1}{\rho_{i-1} A_{x,i-1}} - \frac{1}{\rho_i A_{x,i}} \right) \quad (\text{B. 15})$$

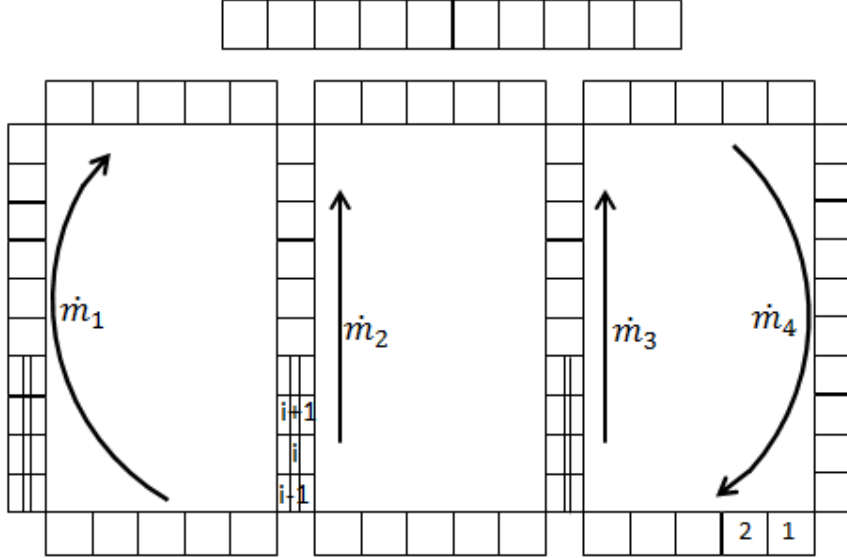


Figure B.3: Discretised experimental model

Figure B.3 shows the discretised experimental model, the control volumes and positive flow rate directions in the different branches.

Branch mass flow rate analysis

In order for all four branches to satisfy the momentum equation (B.15) simultaneously, it was assumed that the pressure difference across the nodes in Figure B.3 is equal for each leg. Furthermore, equation (B.15) was integrated over each branch independently to obtain four equations that were then solved simultaneously to obtain the mass flow rate in each branch. The integration yielded equation (B.16) for each branch, where n and i count as the branch number and control volume numbers per branch respectively. The letters b and k signify the beginning and end control volume numbers of each branch.

$$\int_b^k \frac{L_i}{A_{x,i}} \frac{\Delta \dot{m}_n}{\Delta t} = - \int_b^k \Delta p_i - 2 \int_b^k \frac{L_i}{d_i} \frac{\dot{m}_n |\dot{m}_n|}{\rho_i A_{x,i}^2} (C_{f,i} + K_{m,i}) - \int_b^k \rho_i g L_i \sin(\theta_i) + \int_b^k \frac{\dot{m}_n^2}{A_{x,i}} \left(\frac{1}{\rho_{i-1} A_{x,i-1}} - \frac{1}{\rho_i A_{x,i}} \right) \quad (\text{B.16})$$

The integration manifested itself as a summation due to the control volumes being finite and not infinitesimally small, resulting in equation (B.17).

$$\sum_{i=b}^k \frac{L_i}{A_{x,i}} \frac{\Delta \dot{m}_n}{\Delta t} = - \sum_{i=b}^k \Delta p_i - 2 \sum_{i=b}^k \frac{L_i}{d_i} \frac{\dot{m}_n |\dot{m}_n|}{\rho_i A_{x,i}^2} (C_{f,i} + K_{m,i}) - g \sum_{i=b}^k \rho_i L_i \sin(\theta_i) + \sum_{i=b}^k \frac{\dot{m}_n^2}{A_{x,i}} \left(\frac{1}{\rho_{i-1} A_{x,i-1}} - \frac{1}{\rho_i A_{x,i}} \right) \quad (\text{B.17})$$

Some terms in equation (B.17) were replaced with other variables for simplicity, as follows:

$$S_n = \sum_{i=b}^k \frac{L_i}{A_{x,i}} \quad P_n = \sum_{i=b}^k \Delta p_i \quad F_n = \sum_{i=b}^k \frac{L_i}{d_i} \frac{1}{\rho_i A_{x,i}^2} (C_{f,i} + K_{m,i})$$

$$G_n = \sum_{i=b}^k \rho_i L_i \sin(\theta_i) \quad M_n = \sum_{i=b}^k \frac{1}{A_{x,i}} \left(\frac{1}{\rho_{i-1} A_{x,i-1}} - \frac{1}{\rho_i A_{x,i}} \right)$$

Equation (B.17) becomes:

$$S_n \frac{\Delta(\dot{m}_n)}{\Delta t} = -P_n - 2F_n \dot{m}_n |\dot{m}_n| - gG_n + M_n \dot{m}_n^2 \quad (\text{B.18})$$

Applying equation (B.18) to each one of the four branches results in the following four explicit difference equations:

$$(i) \quad S_1 \frac{\Delta(\dot{m}_1)}{\Delta t} = -P_1 - 2F_1 \dot{m}_1 |\dot{m}_1| - gG_1 + M_1 \dot{m}_1^2 \quad (\text{B.19})$$

$$(ii) \quad S_2 \frac{\Delta(\dot{m}_2)}{\Delta t} = -P_2 - 2F_2 \dot{m}_2 |\dot{m}_2| - gG_2 + M_2 \dot{m}_2^2 \quad (\text{B.20})$$

$$(iii) \quad S_3 \frac{\Delta(\dot{m}_3)}{\Delta t} = -P_3 - 2F_3 \dot{m}_3 |\dot{m}_3| - gG_3 + M_3 \dot{m}_3^2 \quad (\text{B.21})$$

$$(iv) \quad S_4 \frac{\Delta(\dot{m}_4)}{\Delta t} = P_4 - 2F_4 \dot{m}_4 |\dot{m}_4| - gG_4 + M_4 \dot{m}_4^2 \quad (\text{B.22})$$

$$(v) \quad \dot{m}_4 = \dot{m}_1 + \dot{m}_2 + \dot{m}_3 \quad (\text{B.23})$$

Note that the term for the pressure drop in equation (B.22) is positive due to downwards mass flow in the fourth leg of the system. The mass flow rates were solved simultaneously from the above four equations, as follows:

Subtracting equation (B.20) from equation (B.19) results in:

$$S_1 \frac{\Delta(\dot{m}_1)}{\Delta t} - S_2 \frac{\Delta(\dot{m}_2)}{\Delta t} = -P_1 - 2F_1 \dot{m}_1 |\dot{m}_1| - gG_1 + M_1 \dot{m}_1^2 + P_2 + 2F_2 \dot{m}_2 |\dot{m}_2| + gG_2 - M_2 \dot{m}_2^2$$

But $P_1 = P_2 = P_3 = P_4 = P$ (pressure drop is equal for all legs)

Therefore,

$$S_1 \frac{\Delta(\dot{m}_1)}{\Delta t} - S_2 \frac{\Delta(\dot{m}_2)}{\Delta t} = -2F_1 \dot{m}_1 |\dot{m}_1| - gG_1 + M_1 \dot{m}_1^2 + 2F_2 \dot{m}_2 |\dot{m}_2| + gG_2 - M_2 \dot{m}_2^2 \quad (a)$$

Subtracting equation (B.21) from equation (B.20) results in:

$$S_2 \frac{\Delta(\dot{m}_2)}{\Delta t} - S_3 \frac{\Delta(\dot{m}_3)}{\Delta t} = -2F_2\dot{m}_2|\dot{m}_2| - gG_2 + M_2\dot{m}_2^2 + 2F_3\dot{m}_3|\dot{m}_3| + gG_3 - M_3\dot{m}_3^2 \quad (b)$$

Substituting equation (B.23) into equation (B.22) results in:

$$(vi) \quad S_4 \frac{\Delta(\dot{m}_1 + \dot{m}_2 + \dot{m}_3)}{\Delta t} \\ = P_4 - 2F_4(\dot{m}_1 + \dot{m}_2 + \dot{m}_3)|\dot{m}_1 + \dot{m}_2 + \dot{m}_3| - gG_4 + M_4(\dot{m}_1 + \dot{m}_2 + \dot{m}_3)^2$$

Adding equation (B.23) and the above equation results in:

$$S_3 \frac{\Delta(\dot{m}_3)}{\Delta t} + S_4 \frac{\Delta(\dot{m}_1 + \dot{m}_2 + \dot{m}_3)}{\Delta t} = -P_3 - 2F_3\dot{m}_3|\dot{m}_3| - gG_3 - gG_4 + M_3\dot{m}_3^2 + P_4 \\ - 2F_4(\dot{m}_1 + \dot{m}_2 + \dot{m}_3)|\dot{m}_1 + \dot{m}_2 + \dot{m}_3| + M_4(\dot{m}_1 + \dot{m}_2 + \dot{m}_3)^2$$

$$(S_3 + S_4) \frac{\Delta(\dot{m}_3)}{\Delta t} + S_4 \frac{\Delta(\dot{m}_1)}{\Delta t} S_4 \frac{\Delta(\dot{m}_2)}{\Delta t} = -2F_3\dot{m}_3|\dot{m}_3| - 2F_4(\dot{m}_1 + \dot{m}_2 + \dot{m}_3)|\dot{m}_1 + \dot{m}_2 + \dot{m}_3| \\ - gG_3 - gG_4 + M_3\dot{m}_3^2 + M_4(\dot{m}_1 + \dot{m}_2 + \dot{m}_3)^2 \quad (c)$$

Substitute \dot{m}_1 with x , \dot{m}_2 with y , and \dot{m}_3 with z , for convenience, and also let the right-hand sides of equations (a), (b) and (c) equal eqA , eqB , and eqC , respectively. The equations become:

$$S_1x_{t+1} - S_2y_{t+1} = S_1x_t - S_2y_t + \Delta t[eqA] \quad (B.24)$$

$$S_2y_{t+1} - S_3z_{t+1} = S_2y_t - S_3z_t + \Delta t[eqB] \quad (B.25)$$

$$(S_3 + S_4)z_{t+1} + S_4x_{t+1} + S_4y_{t+1} = (S_3 + S_4)z_t + S_4x_t + S_4y_t + \Delta t[eqC] \quad (B.26)$$

All values on the RHS of equations (B.24), (B.25) and (B.26) are values of the previous time step (old values) and are used to determine the new mass flow rates. These equations constitute a system of three simultaneous equations in x_{t+1} , y_{t+1} and z_{t+1} , and setting the right-hand sides of equations (B.24), (B.25) and (B.26) equal to EQ_1 , EQ_2 and EQ_3 respectively, results in the following equations:

$$x_{t+1} = \frac{EQ_1 + S_2y_{t+1}}{S_1} \quad (B.27)$$

$$z_{t+1} = \frac{S_2 y_{t+1} - EQ_2}{S_3} \quad (\text{B.28})$$

Substituting equations (B.27) and (B.28) into equation (B.26) results in:

$$(S_3 + S_4) \frac{S_2 y_{t+1} - EQ_2}{S_3} + S_4 \left(\frac{EQ_1 + S_2 y_{t+1}}{S_1} \right) + S_4 y_{t+1} = EQ_3$$

$$\frac{(S_3 + S_4)}{S_3} S_2 y_{t+1} - \frac{(S_3 + S_4)}{S_3} EQ_2 + \frac{S_4}{S_1} EQ_1 + \frac{S_4 S_2}{S_1} y_{t+1} + S_4 y_{t+1} = EQ_3$$

$$\left(\frac{(S_3 + S_4)}{S_3} S_2 + \frac{S_4 S_2}{S_1} + S_4 \right) y_{t+1} = EQ_3 + \left(\frac{(S_3 + S_4)}{S_3} \right) EQ_2 - \frac{S_4}{S_1} EQ_1$$

$$y_{t+1} = \frac{EQ_3 + ((S_3 + S_4)/S_3)EQ_2 - (S_4/S_1)EQ_1}{((S_3 S_2 + S_4 S_2)/S_3) + (S_4 S_2/S_1) + S_4} \quad (\text{B.29})$$

Now, $\dot{m}_1^{new} = x_{t+1}$, $\dot{m}_2^{new} = y_{t+1}$, $\dot{m}_3^{new} = z_{t+1}$ and $\dot{m}_4^{new} = x_{t+1} + y_{t+1} + z_{t+1}$

New mass flow rates around each branch were calculated at every time step.

B.3 Conservation of Energy

Cengel and Cimbala (2006:171) state that it is convenient to separate mechanical energy from thermal energy and to consider the conversion of mechanical energy to thermal energy as a result of frictional effects as mechanical energy loss. Then the energy equation becomes the mechanical energy balance. The conservation-of-energy principle requires that the net energy transfer to or from a system during a process be equal to the change in the energy content of the system. Consider the energy control volume in Figure B.4.

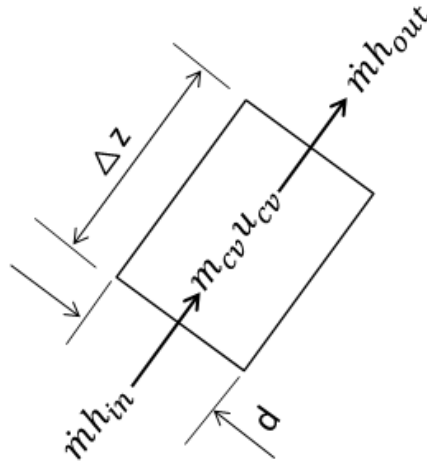


Figure B.4: Energy control volume

Control volumes involve energy transfer via mass flow and the conservation-of-energy principle, also called the energy balance, is expressed as

$$\dot{E}_{in} - \dot{E}_{out} = \frac{dE_{cv}}{dt} \quad (\text{B. 30})$$

where \dot{E}_{in} and \dot{E}_{out} are the total rates of energy transfer into and out of the control volume respectively, and $\frac{dE_{cv}}{dt}$ is the rate of change of energy within the control volume boundaries.

According to Cengel and Cimbala (2006), the energy content of a fixed quantity of mass (a closed system) can be changed by two mechanisms, viz. heat transfer Q and work transfer W . For a fixed control volume, the energy equation can be expressed as

$$\dot{Q}_{net,in} + \dot{W}_{shaft,net,in} = \frac{d}{dt} \int_{cv} e \rho dV + \int_{cs} \left(\frac{p}{\rho} + e \right) \rho (\vec{v} \cdot \vec{n}) dA \quad (\text{B. 31})$$

In this study, $\dot{W}_{shaft,net,in} = 0$, no shaft is involved to drive the flow in the system, and then the energy equation becomes

$$\dot{Q}_{net,in} = \frac{d}{dt} \int_{cv} e \rho dV + \int_{cs} \left(\frac{p}{\rho} + e \right) \rho (\vec{v} \cdot \vec{n}) dA \quad (\text{B. 32})$$

Rewriting the second integral term in terms of average velocities and mass flow rates through the inlets and outlets, and assuming that $\left(\frac{p}{\rho} + e\right)$ is nearly uniform across the inlet and outlets, it can then be taken out of the integral (Cengel & Cimbala, 2006:205). Noting that $\dot{m} = \int_{A_x} \rho (\vec{v} \cdot \vec{n}) dA_x$ across the inlet and outlet, then equation (B.32) becomes

$$\dot{Q}_{net,in} = \frac{d}{dt} \int_{cv} e \rho dV + \left(\dot{m} \left(\frac{p}{\rho} + e \right) \right)_{out} - \left(\dot{m} \left(\frac{p}{\rho} + e \right) \right)_{in} \quad (\text{B. 33})$$

where $e = u + \frac{v^2}{2} + gz$, is the total energy per unit mass for both the control volume and the flow stream, and substituting back into equation (B.33) results in

$$\begin{aligned} \dot{Q}_{net,in} = \frac{d}{dt} \int_{cv} \left(u + \frac{v^2}{2} + gz \right) \rho dV + \left(\dot{m} \left(\frac{p}{\rho} + u + \frac{v^2}{2} + gz \right) \right)_{out} \\ - \left(\dot{m} \left(\frac{p}{\rho} + u + \frac{v^2}{2} + gz \right) \right)_{in} \end{aligned} \quad (\text{B. 34})$$

Knowing the definition of enthalpy $h = u + pv = u + \frac{p}{\rho}$, equation (B.34) becomes

$$\dot{Q}_{net,in} = \frac{d}{dt} \int_{cv} \left(u + \frac{v^2}{2} + gz \right) \rho dV + \left(\dot{m} \left(h + \frac{v^2}{2} + gz \right) \right)_{out} - \left(\dot{m} \left(h + \frac{v^2}{2} + gz \right) \right)_{in} \quad (\text{B. 35})$$

Considering the fact that kinetic energy and potential energy are very small compared to the enthalpy, and therefore can be discarded, then equation (B.35) becomes

$$\dot{Q}_{net,in} = \frac{d}{dt} \int_{cv} u \rho dV + (\dot{m}h)_{out} - (\dot{m}h)_{in} \quad (\text{B. 36})$$

Integrating the integral term in equation (B.36) over the control volume for the finite time step, and knowing that internal energy for a fixed control volume $u = C_v T$, results in

$$\frac{d}{dt} \int_{cv} u \rho dV = \frac{d}{dt} (u \rho V) = \frac{d}{dt} (u \rho A_x L) = L A_x \frac{d}{dt} (\rho C_v T) \quad (\text{B. 37a})$$

$$\begin{aligned} \text{But } \frac{d}{dt} (\rho C_v T) &= \rho \frac{d}{dt} (C_v T) + C_v \frac{d}{dt} (\rho T) + T \frac{d}{dt} (\rho C_v) && \text{(by chain rule)} \\ &= 2C_v T \frac{d\rho}{dt} + 2\rho T \frac{dC_v}{dt} + 2\rho C_v \frac{dT}{dt} \end{aligned}$$

Then equation (B.37a) becomes

$$\frac{d}{dt} \int_{cv} u \rho dV = LA_x \frac{d}{dt} (\rho C_v T) = LA_x \left(2C_v T \frac{d\rho}{dt} + 2\rho T \frac{dC_v}{dt} + 2\rho C_v \frac{dT}{dt} \right) \quad (\text{B.37b})$$

Substituting equation (B.37b) into equation (B.36) results in the following energy equation:

$$\dot{Q}_{net,in} = LA_x \left(2C_v T \frac{d\rho}{dt} + 2\rho T \frac{dC_v}{dt} + 2\rho C_v \frac{dT}{dt} \right) + (\dot{m}h)_{out} - (\dot{m}h)_{in} \quad (\text{B.38})$$

The LHS equation (B.38) can be expanded as follows

$$\dot{Q}_{net,in} = \dot{Q}_{in} - \dot{Q}_{out} \quad (\text{B.39})$$

The source of heat into the system is the electric heating elements, hence $\dot{Q}_{in} = \frac{V^2}{R}$, where V and R are the voltage and resistance of the heating element respectively. \dot{Q}_{out} is the convection heat loss to the surroundings. $\dot{Q}_{out} = h_{com} A_z (T_s - T_\infty)$, where T_s is the temperature of the surface of the system and T_∞ is the temperature of the surroundings or atmosphere, h_{com} is the combination of convection and radiation heat-transfer coefficients, and A_z is the surface area. Substituting into equation (B.39) results in

$$\dot{Q}_{net,in} = \frac{V^2}{R} - h_{com} A_z (T_s - T_\infty) \quad (\text{B.40})$$

Substituting equation (B.40) into equation (B.38) results in

$$\frac{V^2}{R} - h_{com} A_z (T_s - T_\infty) = LA_x \left(2C_v T \frac{d\rho}{dt} + 2\rho T \frac{dC_v}{dt} + 2\rho C_v \frac{dT}{dt} \right) + (\dot{m}h)_{out} - (\dot{m}h)_{in} \quad (\text{B.41})$$

Knowing that enthalpy $h = C_p T$, then $(\dot{m}h)_{out} - (\dot{m}h)_{in} = \dot{m} C_p (T_{out} - T_{in})$, substituting back into equation (B.41), gives

$$\frac{V^2}{R} - h_{com} A_z (T_s - T_\infty) = LA_x \left(2C_v T \frac{d\rho}{dt} + 2\rho T \frac{dC_v}{dt} + 2\rho C_v \frac{dT}{dt} \right) + \dot{m} C_p (T_{out} - T_{in}) \quad (\text{B.42})$$

Solving for $\frac{dT}{dt}$ in equation (B.42) results in

$$\frac{dT}{dt} = \frac{1}{2\rho C_v LA_x} \left[\frac{V^2}{R} - h_{com} A_z (T_s - T_\infty) + \dot{m} C_p (T_{in} - T_{out}) - LA_x \left(2C_v T \frac{d\rho}{dt} + 2\rho T \frac{dC_v}{dt} \right) \right] \quad (\text{B.43})$$

Writing equation (B.43) in finite differences results in

$$T^{n+1} = T^n + \frac{\Delta t}{2\rho_i C_v L_i A_{x,i}} \left[\frac{v^2}{R} - h_{com,i} A_{z,i} (T_{s,i} - T_\infty) + \dot{m}^n C_p (T_{in} - T_{out}) - L_i A_{x,i} (2C_v T^n \frac{\Delta \rho}{\Delta t} + 2\rho_i T^n \frac{\Delta C_v}{\Delta t}) \right] \quad (\text{B. 44})$$

B.4 Closure Equations

This section provides the equations required for calculating fluid properties and friction factors for both single- and two-phase fluids. The resulting equations were used to determine channel mass flow rates using the derived momentum equation given in Appendix A.2.

The thermodynamic properties of water and air were adapted from the appendices of Kröger (1998) according to White (2011:58), and this source offers enthalpy, density, etc., equations appropriate to use in a computer program.

Laminar Flow

For single-phase flow, the Darcy friction factor for laminar flow is given by Cengel and Cimbala (2006) as:

$$f_{lam} = \frac{64}{Re_d}$$

Darcy to Fanning conversion is given by Cengel and Cimbala (2006) as

$$c_f = \frac{16}{Re} \quad \text{for } Re < 1181$$

The Nusselt number for laminar fully-developed flow is adapted from Cengel (2006:468) as

$$Nu = \frac{hd}{k}$$

$Nu = 4.36$ laminar flow with , constant heat flux (Cengel, 2006: 468)

Turbulence Flow

For the turbulence regime, the following options for friction factor were considered:

Blasius's equation (Cengel, 2006)

$$f_{turb} = 0.316 Re_d^{-0.25} \quad 4000 \leq Re_d \leq 10^5$$

Filonenko's (1948) approximation of the Colebrook equation for smooth walls (White, 2011:58):

$$f_{turb} = (1.82 \log(Re_d) - 1.64)^{-2} \quad 4000 \leq Re_d \leq 10^{12}$$

Dobson (2014) and White (2011:58) recommended the Reynolds number at the transition point from laminar to turbulence to be taken as 1 181.

Colebrook's equation was used on the assumption that polycarbonate material is smooth (Cengel, 2006:867) and the fact that this equation was used to plot the Moody chart.

The minor losses coefficient was obtained from White (2011:59) and is given as

$$\tau_m = \rho \frac{v^2}{2} \sum K$$

The Nusselt number for turbulent flow is adapted from Cengel (2006:474) as

$$Nu = \frac{\left(\frac{f}{8}\right)(Re - 1000)Pr}{1 + 12.7\left(\frac{f}{8}\right)^{0.5}\left(Pr^{2/3} - 1\right)} \quad \text{turbulent, Gnielinski(Cengel, 2006: 474)}$$

According to Cengel (2007:474), this equation is more accurate.

Two-phase flow

For the two-phase flow, the void fraction concept was adapted. The vapour quality is given by

$$x = \frac{\dot{m}_g}{\dot{m}_g + \dot{m}_l}$$

Assuming that the two-phase mixture is homogenous, i.e. the velocity of each phase is the same, the density of the flow is adapted from Nayak et al. (2006:653) and White (2011:59).

$$\rho = \alpha\rho_v + (1 - \alpha)\rho_l$$

where α is the void fraction and is given as

$$\alpha = \left(1 + \frac{(1 - x)\rho_v}{x\rho_l}\right)^{-1}$$

Substituting the void fraction back into the two-phase density equation results in

$$\rho = \left[\frac{x}{\rho_v} + \frac{1 - x}{\rho_l}\right]^{-1}$$

Other two-phase flow properties, such as dynamic viscosity, specific heat and thermal conductivity, were adapted from Dobson and Ruppertsberg (2008:3), and are given below as respectively:

$$\mu = \left[\frac{x}{\mu_v} + \frac{1 - x}{\mu_l}\right]^{-1}$$

$$c_p = xc_{p,v} + (1 - x)c_{p,l}$$

$$k = \alpha k_v + (1 - \alpha)k_l$$

The friction factor for two-phase flow was determined using the friction multiplier method and the Darcy to Fanning conversion $c_f = \frac{1}{4}f$.

$$f_{2\phi} = \phi_{lo}^2 f_{1\phi}$$

where White gives the friction multiplier as given by Whalley (1987:41, in White, 2011:59)

$$\phi_{lo}^2 = \frac{C_{fv0}\rho_l}{C_{f10}\rho_v}$$

This equation is claimed by White (2011:59) to be unrestricted in terms of applicability in the loop, where C_{fv0} and C_{f10} refer to coefficients of friction for vapour only and liquid only respectively.

The two-phase flow coefficient of friction was adapted from White (2011:60) for its simplicity and easy applicability in the program.

$$\frac{h}{h_{lo}} = (1-x)^{0.8} + \frac{3.8x^{0.76}(1-x)^{0.04}}{P_r^{0.38}}$$

where h_{lo} refers to liquid only heat transfer coefficient, x to the fluid quality and P_r to the reduced pressure, given by $P_r = p/p_{crit}$; p_{crit} is the critical pressure.

Environmental losses

The environmental losses were adapted from White (2011:61) and verified in Cengel (2007:511). The losses from White (2011:61) were chosen due to good experimental approximation of his computer code.

Natural convection on horizontal tubes ($Ra_D \leq 10^{12}$) (White, 2011:61):

$$Nu = \left(0.6 + \frac{0.387 Ra_D^{\frac{1}{6}}}{\left[1 + \left(\frac{0.559}{Pr} \right)^{\frac{9}{16}} \right]^{\frac{4}{9}}} \right)$$

Where $Ra_L = Gr_L Pr$ (Grashof times Prandtl numbers) and $Nu = \frac{hL}{k}$.

The diameters of all the tubes in the experimental set-up satisfied this relation $\geq \frac{35L}{Gr_L^{1/4}}$, according to Cengel (2007:511) and White (2011:61). If this is true, the following natural convection can be used for vertical tubes:

$$Nu = \left\{ 0.825 + \frac{0.387 Ra_L^{\frac{1}{6}}}{\left[1 + (0.492/Pr)^{9/16} \right]^{8/27}} \right\}^2$$

APPENDIX C: DERIVATION OF MOMENTUM EQUATION ASSUMING STEADY FLOW

The conservation of momentum equation was also solved by assuming that the flow rate of the fluid at a particular fixed point in the system does not change with time. This assumption states that the flow will be smooth from start-up to finish, which automatically eliminates all time-dependent terms in the general momentum equation (B.15), decreasing the degree of complexity in the calculation of the mass flow rates. The derivation of the steady mass flow rate equations is presented in this section. However, the derived equations were not used in the computer code to test the performance of the system assuming steady-state conditions apply.

Linear momentum equation

The general momentum equation is given by equation (B.15) as

$$\frac{L_i}{A_{x,i}} \frac{\Delta \dot{m}_n}{\Delta t} = -\Delta p_i - 2 \frac{L_i}{d_i} \frac{\dot{m}_n^2}{\rho_i A_{x,i}^2} (C_{f,i} + K_{m,i}) \pm \rho_i g L_i \sin(\theta_i) + \frac{\dot{m}_n^2}{A_{x,i}} \left(\frac{1}{\rho_{i-1} A_{x,i-1}} - \frac{1}{\rho_i A_{x,i}} \right) \quad (C.1)$$

For steady flow $\frac{L_i}{A_{x,i}} \frac{\Delta \dot{m}_n}{\Delta t} = 0$ and

equation (C.1) becomes

$$0 = -\Delta p_i - 2 \frac{L_i}{d_i} \frac{\dot{m}_n^2}{\rho_i A_{x,i}^2} (C_{f,i} + K_{m,i}) \pm \rho_i g L_i \sin(\theta_i) + \frac{\dot{m}_n^2}{A_{x,i}} \left(\frac{1}{\rho_{i-1} A_{x,i-1}} - \frac{1}{\rho_i A_{x,i}} \right) \quad (C.2)$$

Integrating equation (C.2) into each branch yields

$$0 = - \int_b^k \Delta p_i - 2 \int_b^k \frac{L_i}{d_i} \frac{\dot{m}_n^2}{\rho_i A_{x,i}^2} (C_{f,i} + K_{m,i}) \pm \int_b^k \rho_i g L_i \sin(\theta_i) + \int_b^k \frac{\dot{m}_n^2}{A_{x,i}} \left(\frac{1}{\rho_{i-1} A_{x,i-1}} - \frac{1}{\rho_i A_{x,i}} \right) \quad (C.3)$$

The integration manifested itself as a summation due to the control volumes being finite and not infinitesimally small, resulting in equation (C.4) for each branch, where n and i denote the branch number and number of control volumes in each branch respectively. The letters b and k signify the beginning (bottom) and end (top) control volume numbers of each branch.

$$0 = - \sum_{i=b}^k \Delta p_i - 2 \sum_{i=b}^k \frac{L_i}{d_i} \frac{\dot{m}_n^2}{\rho_i A_{x,i}^2} (C_{f,i} + K_{m,i}) \pm g \sum_{i=b}^k \rho_i L_i \sin(\theta_i) + \sum_{i=b}^k \frac{\dot{m}_n^2}{A_{x,i}} \left(\frac{1}{\rho_{i-1} A_{x,i-1}} - \frac{1}{\rho_i A_{x,i}} \right) \quad (C.4)$$

Solving for the mass flow rate in equation (C.4) gives

$$\dot{m}_n^2 = \frac{\sum_{i=b}^k (p_{in} - p_{out})_i \pm g \sum_{i=b}^k \rho_i L_i \sin(\theta_i)}{2 \sum_{i=b}^k \frac{L_i}{d_i} \frac{(C_{f,i} + K_{m,i})}{\rho_i A_{x,i}^2} - \sum_{i=b}^k \frac{1}{A_{x,i}} \left(\frac{1}{\rho_{i-1} A_{x,i-1}} - \frac{1}{\rho_i A_{x,i}} \right)} \quad (\text{C.5})$$

but $C_f = 0.078 Re^{-0.25}$, where $Re = \frac{\rho v d}{\mu}$ and $v = \frac{\dot{m}_n}{\rho A_x}$

therefore $C_f = 0.078 \left(\frac{\rho \dot{m}_n d}{\mu \rho A_x} \right)^{-0.25} = 0.078 (\dot{m}_n d / \mu A_x)^{-0.25}$

Substituting into equation (C.5) results in

$$\dot{m}_n^2 = \frac{\sum_{i=b}^k (p_{in} - p_{out})_i \pm g \sum_{i=b}^k \rho_i L_i \sin(\theta_i)}{2 \sum_{i=b}^k \frac{L_i}{d_i} \frac{\left(\left(0.078 (\dot{m}_n d_i / \mu_i A_{x,i})^{-0.25} \right) + K_{m,i} \right)}{\rho_i A_{x,i}^2} - \sum_{i=b}^k \frac{1}{A_{x,i}} \left(\frac{1}{\rho_{i-1} A_{x,i-1}} - \frac{1}{\rho_i A_{x,i}} \right)}$$

$$\dot{m}_n = \pm \sqrt{\frac{\sum_{i=b}^k (p_{in} - p_{out})_i \pm g \sum_{i=b}^k \rho_i L_i \sin(\theta_i)}{2 \sum_{i=b}^k \frac{L_i}{d_i} \frac{\left(\left(0.078 (\dot{m}_n d_i / \mu_i A_{x,i})^{-0.25} \right) + K_{m,i} \right)}{\rho_i A_{x,i}^2} - \sum_{i=b}^k \frac{1}{A_{x,i}} \left(\frac{1}{\rho_{i-1} A_{x,i-1}} - \frac{1}{\rho_i A_{x,i}} \right)}} \quad (\text{C.6})$$

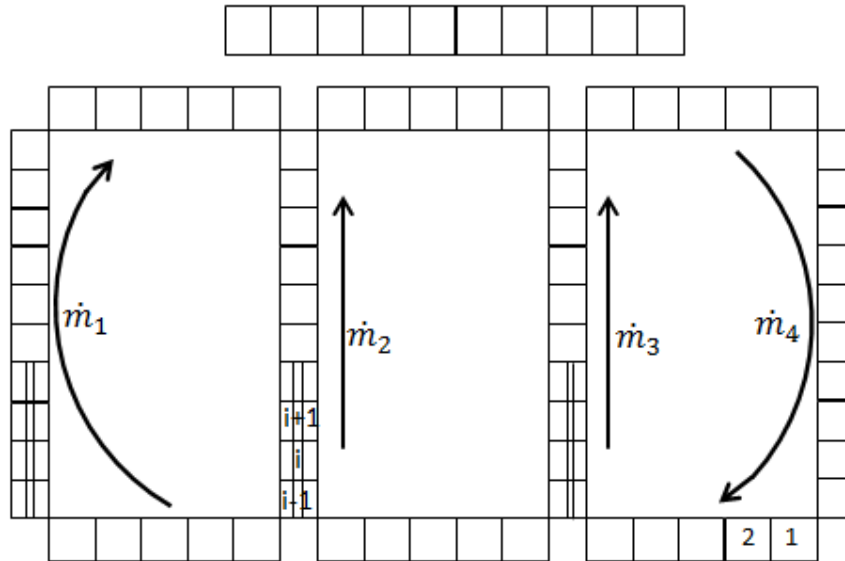


Figure C.1: Discretised experimental model (Figure B.3 repeated)

Applying equation (C.6) to each every branch in Figure C.1 results in the following equations:

$$\dot{m}_1 = \pm \sqrt{\frac{\sum_{i=b}^k (p_{in} - p_{out})_i \pm g \sum_{i=b}^k \rho_i L_i \sin(\theta_i)}{2 \sum_{i=b}^k \frac{L_i}{d_i} \left(\frac{(0.078(\dot{m}_1 d_i / \mu_i A_{x,i})^{-0.25}) + K_{m,i}}{\rho_i A_{x,i}^2} \right) - \sum_{i=b}^k \frac{1}{A_{x,i}} \left(\frac{1}{\rho_{i-1} A_{x,i-1}} - \frac{1}{\rho_i A_{x,i}} \right)}} \quad (C.7)$$

$$\dot{m}_2 = \pm \sqrt{\frac{\sum_{i=b}^k (p_{in} - p_{out})_i \pm g \sum_{i=b}^k \rho_i L_i \sin(\theta_i)}{2 \sum_{i=b}^k \frac{L_i}{d_i} \left(\frac{(0.078(\dot{m}_2 d_i / \mu_i A_{x,i})^{-0.25}) + K_{m,i}}{\rho_i A_{x,i}^2} \right) - \sum_{i=b}^k \frac{1}{A_{x,i}} \left(\frac{1}{\rho_{i-1} A_{x,i-1}} - \frac{1}{\rho_i A_{x,i}} \right)}} \quad (C.8)$$

$$\dot{m}_3 = \pm \sqrt{\frac{\sum_{i=b}^k (p_{in} - p_{out})_i \pm g \sum_{i=b}^k \rho_i L_i \sin(\theta_i)}{2 \sum_{i=b}^k \frac{L_i}{d_i} \left(\frac{(0.078(\dot{m}_3 d_i / \mu_i A_{x,i})^{-0.25}) + K_{m,i}}{\rho_i A_{x,i}^2} \right) - \sum_{i=b}^k \frac{1}{A_{x,i}} \left(\frac{1}{\rho_{i-1} A_{x,i-1}} - \frac{1}{\rho_i A_{x,i}} \right)}} \quad (C.9)$$

$$\dot{m}_4 = \pm \sqrt{\frac{\sum_{i=b}^k (p_{in} - p_{out})_i \pm g \sum_{i=b}^k \rho_i L_i \sin(\theta_i)}{2 \sum_{i=b}^k \frac{L_i}{d_i} \left(\frac{(0.078(\dot{m}_4 d_i / \mu_i A_{x,i})^{-0.25}) + K_{m,i}}{\rho_i A_{x,i}^2} \right) - \sum_{i=b}^k \frac{1}{A_{x,i}} \left(\frac{1}{\rho_{i-1} A_{x,i-1}} - \frac{1}{\rho_i A_{x,i}} \right)}} \quad (C.10)$$

$$\dot{m}_4 = \dot{m}_1 + \dot{m}_2 + \dot{m}_3 \quad (C.11)$$

Substituting equation (C.11) into equation (C.10) gives

$$\dot{m}_4 = \pm \sqrt{\frac{\sum_{i=b}^k (p_{in} - p_{out})_i \pm g \sum_{i=b}^k \rho_i L_i \sin(\theta_i)}{2 \sum_{i=b}^k \frac{L_i}{d_i} \left(\frac{(0.078((\dot{m}_1 + \dot{m}_2 + \dot{m}_3) d_i / \mu_i A_{x,i})^{-0.25}) + K_{m,i}}{\rho_i A_{x,i}^2} \right) - \sum_{i=b}^k \frac{1}{A_{x,i}} \left(\frac{1}{\rho_{i-1} A_{x,i-1}} - \frac{1}{\rho_i A_{x,i}} \right)}} \quad (C.12)$$

APPENDIX D: PHOTOGRAPHS OF EXPERIMENTAL SETUP

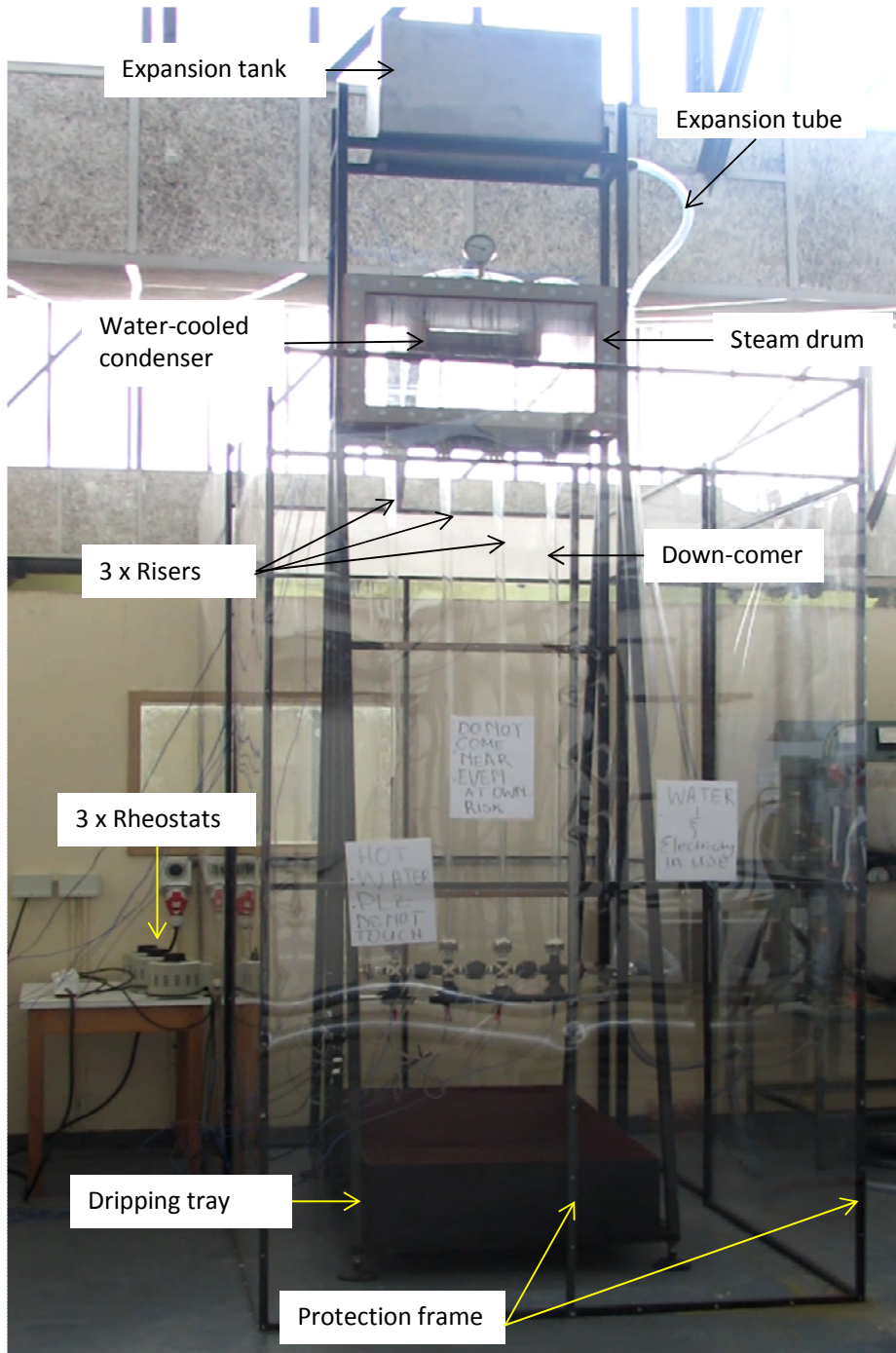


Figure D.1: Photograph of experimental facility

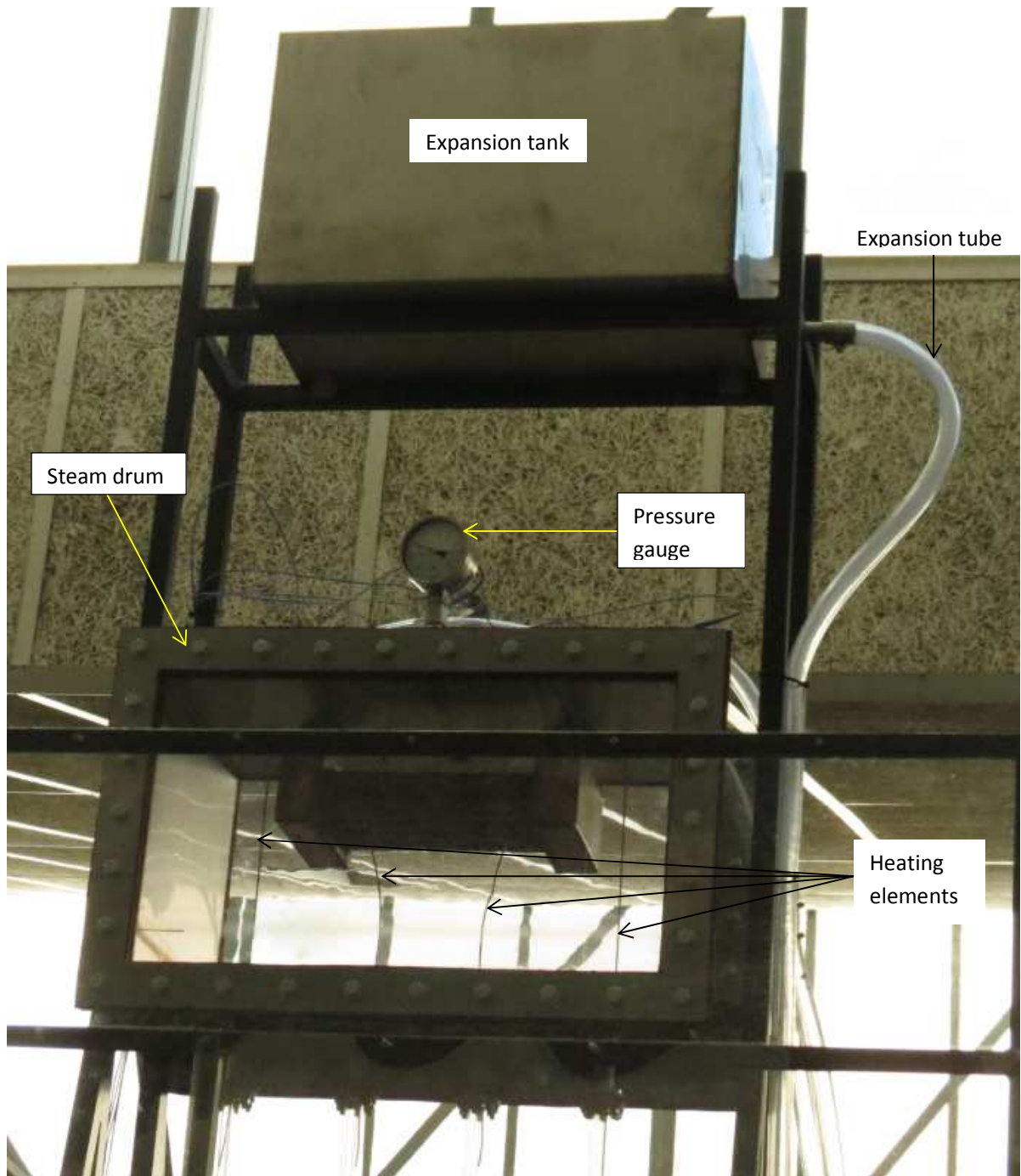


Figure D.2: Heating elements and pressure gauge mounted on the steam drum

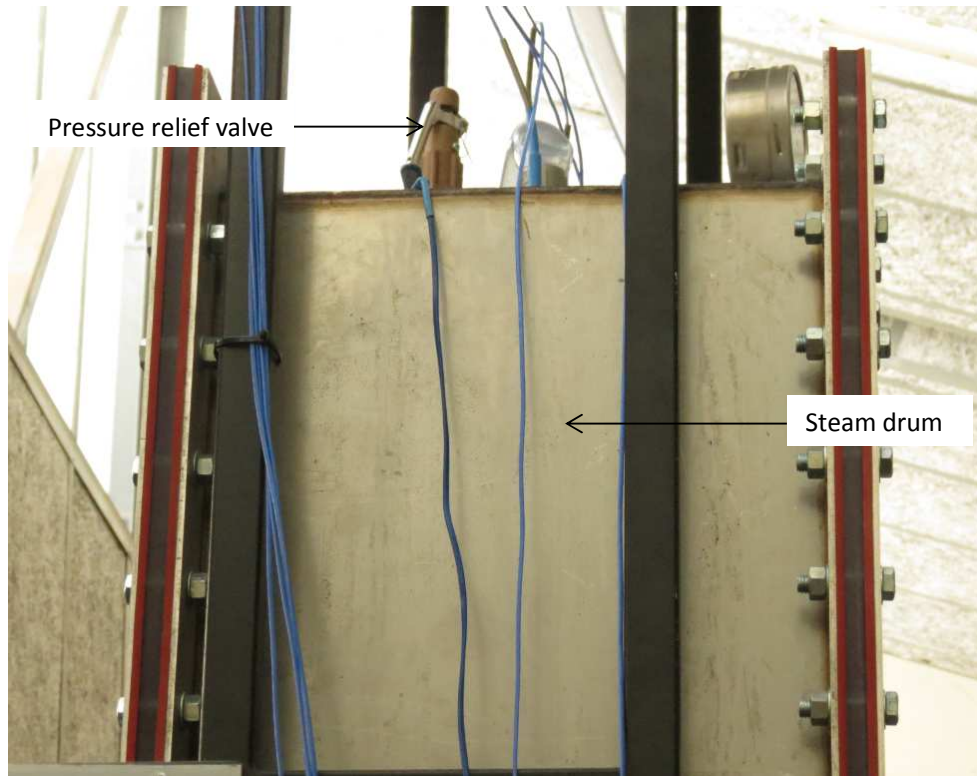


Figure D.3: Pressure relief valve mounted on the steam drum

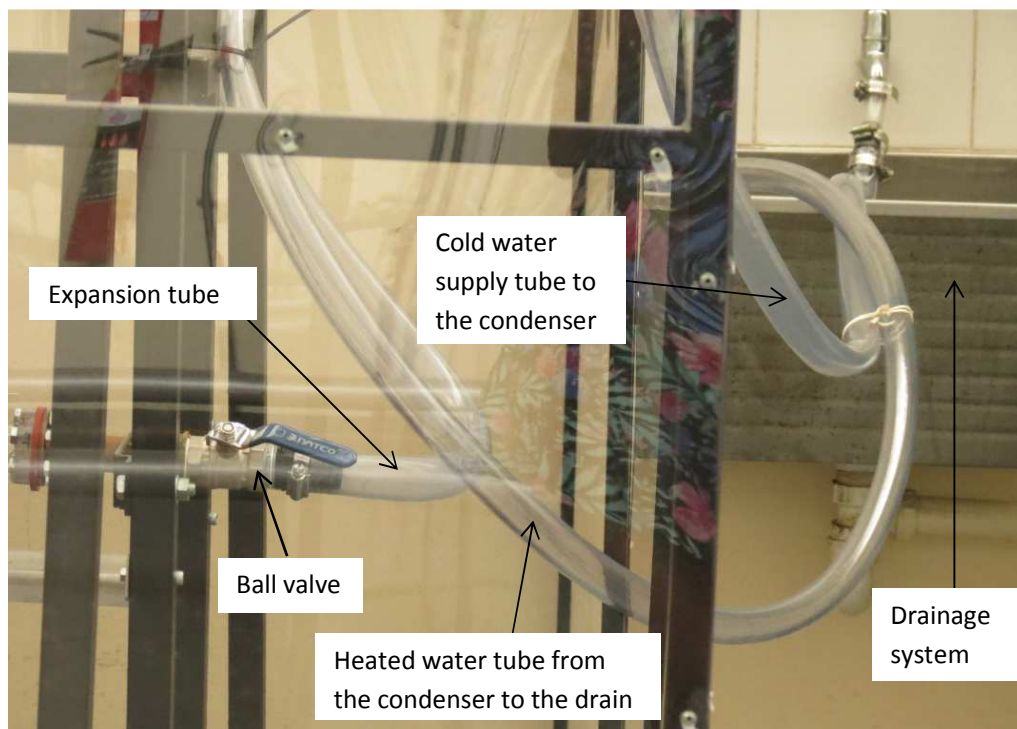


Figure D.4: Valve connecting the expansion tank to the system and drainage system

APPENDIX E: SAMPLE RESULT OUTPUTS OF THE DEVELOPED PROGRAM

Time (s)	W1	W2	W3	WS	Tr1t	Tr1b	Tr2t	Tr2b	Tr3t	Tr3b	Tct	Tcb	Tcwb	Tcwt	Q1	Q2	Q3	Qs
0.50	-0.0001	0	0	0	20.2	20.4	21	21.6	21	21.6	21	21	20	20	-0.1211	0.0496	0.0496	-0.0219
1.00	-0.0001	0.0001	0.0001	0	20.2	21	21	22.2	21	22.2	21	21	20	20	-0.2288	0.118	0.118	0.0072
1.50	-0.0002	0.0001	0.0001	0	20.2	21.6	21	22.7	21	22.7	21	21	20	20	-0.3148	0.2021	0.2019	0.0893
2.00	-0.0002	0.0002	0.0002	0.0001	20.2	22.2	21	23.3	21	23.3	21	21	20	20	-0.3825	0.3023	0.3018	0.2216
2.50	-0.0002	0.0002	0.0002	0.0002	20.2	22.8	21	23.9	21	23.9	21	21	20	20	-0.4335	0.4184	0.4172	0.4021
3.00	-0.0002	0.0003	0.0003	0.0003	20.2	23.3	21	24.4	21	24.5	21	21	20	20	-0.4689	0.5497	0.5474	0.6283
3.50	-0.0002	0.0003	0.0003	0.0004	20.2	23.9	21	25	21	25	21	21	20	20	-0.4893	0.6955	0.6913	0.8975
4.00	-0.0002	0.0004	0.0004	0.0006	20.2	24.5	21	25.6	21	25.6	21	21	20	20	-0.4954	0.8546	0.8473	1.2065
4.50	-0.0002	0.0005	0.0005	0.0008	20.2	25.1	21	26.1	21	26.2	21	21	20	20	-0.4879	1.0257	1.0136	1.5514
5.00	-0.0002	0.0006	0.0006	0.001	20.2	25.7	21	26.7	21	26.7	21	21	20	20	-0.4674	1.2073	1.1881	1.928
5.50	-0.0002	0.0007	0.0007	0.0012	20.2	26.2	21	27.2	21	27.3	21	21	20	20	-0.435	1.3977	1.3686	2.3313
6.00	-0.0002	0.0008	0.0008	0.0014	20.2	26.8	21	27.8	21	27.8	21	21	20	20	-0.3915	1.5954	1.5527	2.7565
6.50	-0.0002	0.0009	0.0009	0.0016	20.2	27.4	21	28.3	21	28.3	21	21	20	20	-0.3381	1.7986	1.7379	3.1984
7.00	-0.0001	0.001	0.001	0.0018	20.2	28	21	28.9	21	28.8	21	21	20	20	-0.2756	2.0057	1.9217	3.6519
7.50	-0.0001	0.0011	0.0011	0.0021	20.2	28.5	21	29.5	21	29.3	21	21	20	20	-0.2052	2.2153	2.102	4.1122
8.00	-0.0001	0.0012	0.0011	0.0023	20.2	29.1	21	30	21	29.7	21	21	20	20	-0.1278	2.4261	2.2766	4.5749
8.50	0	0.0013	0.0012	0.0025	20.2	29.7	21	30.6	21	30.1	21	21	20	20	-0.0443	2.6369	2.4435	5.0362
9.00	0	0.0014	0.0013	0.0027	20.2	30.3	21	31.2	21	30.5	21	21	20	20	0.0447	2.847	2.6012	5.4929
9.50	0.0001	0.0015	0.0014	0.003	20.2	30.8	21	31.7	21	30.9	21	21	20	20	0.1382	3.0557	2.7485	5.9424
10.00	0.0001	0.0016	0.0014	0.0032	20.2	31.4	21	32.3	21	31.2	21	21	20	20	0.2352	3.2626	2.8845	6.3823
10.50	0.0002	0.0017	0.0015	0.0034	20.2	32	21	32.9	21	31.5	21	21	20	20	0.3345	3.4676	3.009	6.8111
11.00	0.0002	0.0018	0.0016	0.0036	20.2	32.5	21	33.4	21	31.8	21	21	20	20	0.4355	3.6707	3.1216	7.2279
.
.
.

APPENDIX F: RESULTS FROM SIMILAR WORK DONE BY OTHER RESEACHERS

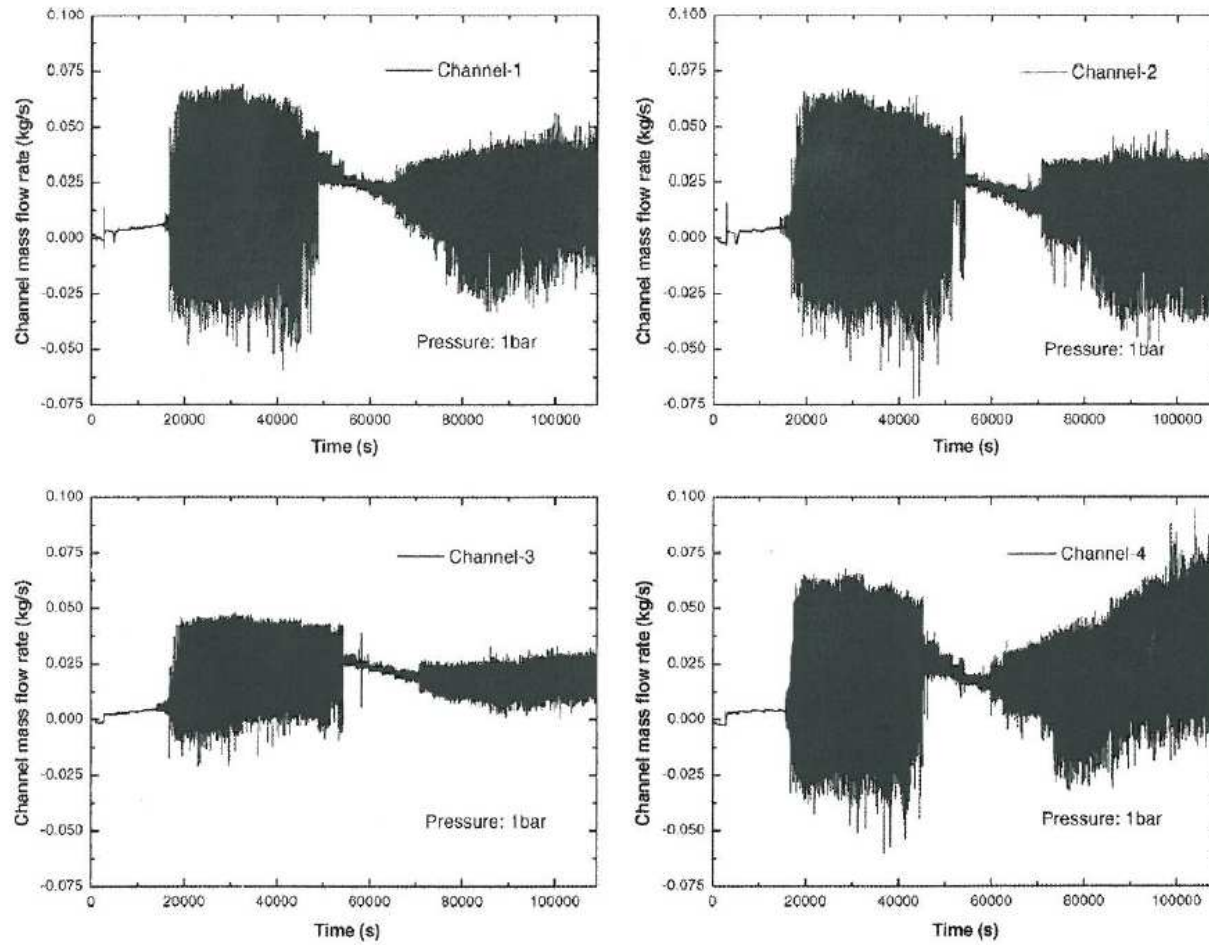


Figure F.1: Individual channel behaviour for experiment at 1 bar pressure (Jain et al., 2010:784)

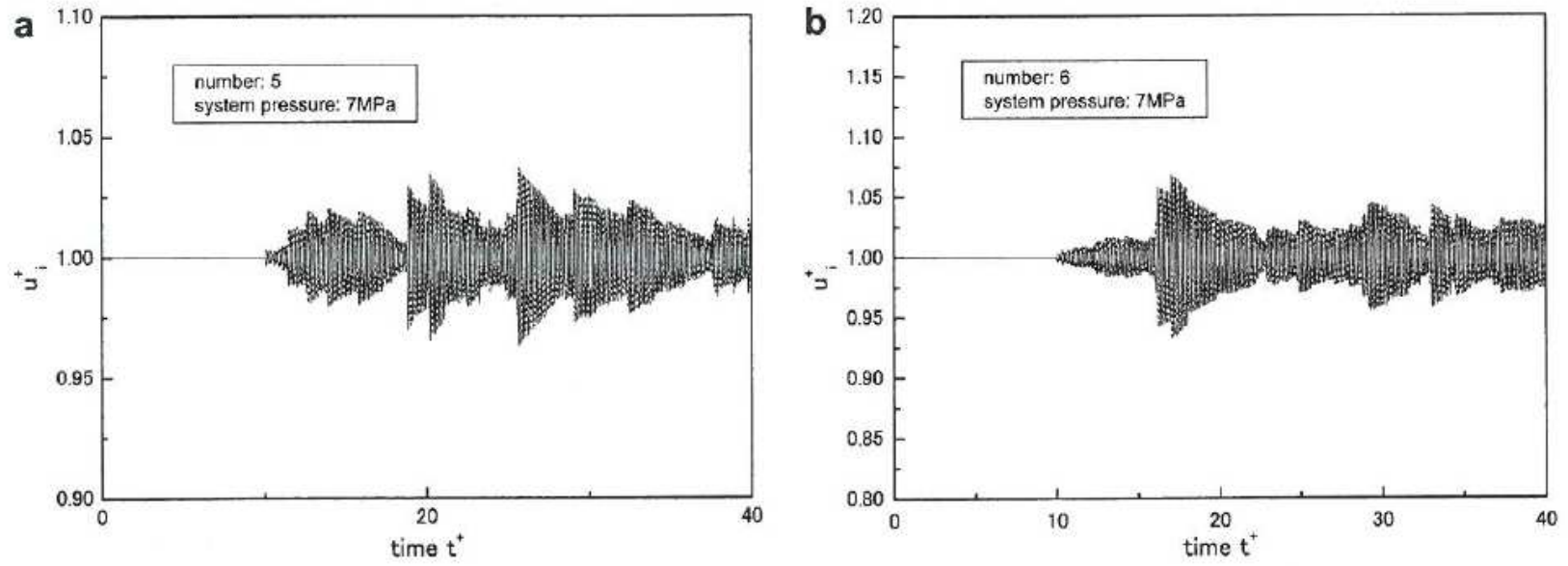


Figure F.2: Inlet velocity oscillation curves (Yun et al., 2008:673)